UNIVERSITY OF TROMSØ UIT

FACULTY OF SCIENCE AND TECHNOLOGY
DEPARTMENT OF PHYSICS AND TECHNOLOGY

Coastal wind from SAR and NWP model for offshore wind power production

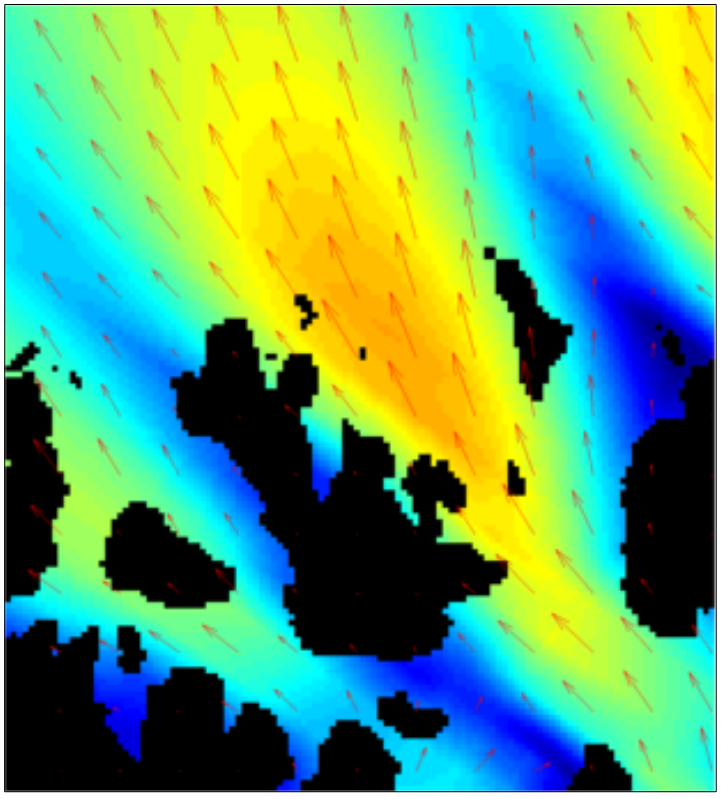

Malin Abrahamsen

EOM-3901 Master's Thesis in
Energy, Climate and Environment

July 2013

The Cloud

I am the daughter of Earth and Water,
And the nursling of the Sky;
I pass through the pores of the ocean and shores;
I change, but I cannot die.
For after the rain when with never a stain
The pavilion of Heaven is bare,
And the winds and sunbeams with their convex gleams
Build up the blue dome of air,
I silently laugh at my own cenotaph,
And out of the caverns of rain,
Like a child from the womb, like a ghost from the tomb,
I arise and unbuild it again.

Percy Bysshe Shelley (1792 - 1822)

Acknowledgement

This study was made possible thanks to the generous contribution of several people and groups. A large thank you to NORUT for making the satellite ASAR images available to me, and to MET for letting me use their weather model data and providing a great deal of assistance in figuring it out. A special thank you to Eirik Samuelsen and Bård Fjukstad at MET for patiently answering all my many, many questions. I am also very grateful to Troms Kraft for letting me use the wind observations from Fakken.

Behind every panicking master student stand the patient supervisors. Thank you to Harald Johnsen for your highly infectious fascination with wind streaks and all things SAR, and for guiding me safely through new territory. Thank you to Yngve Birkelund for your optimism, enthusiasm and for constantly telling me not to worry. I'm afraid that last part was beyond me.

Though a master's degree is not the elusive thing it used to be, this is the culmination of a very long journey for me, and I am incredibly grateful that I got to make it. Thank you to my beloved Sindre for always believing in me, for putting up with me, for letting me vent and letting me ramble and always, always being there for me. To my parents: I love you and I promise to call more often.

Abstract

With rising energy demands as well as technological advances, offshore wind power production is becoming an attractive option. However, it is necessary to estimate the wind climate at potential sites in order to achieve optimal siting, and numerical weather prediction models as well as satellite SAR can been used in a first evaluation for this purpose. Complicated wind climates in coastal regions can make this challenging. This study looks at how ASAR and model wind maps compare in terms of estimating coastal wind climates, and whether they can identify local features important to wind farm siting.

ASAR images covering Vannøya in northern Norway have been acquired for a period of just over a year. They have been converted to wind speed maps using the CMOD-IFR2 algorithm, with model wind directions as input, and averaged to 450 m resolution. UM.4km wind model data from MET, covering the same area and time period, have been interpolated to match the resolution of the ASAR wind maps. In-situ observations from the on-shore Fakken wind farm have been made available by Troms Kraft, and have been compared with model predictions for the same location. To get a better idea of how the model and ASAR wind estimates fare in a coastal region, both descriptive statistics and an in-depth analysis of individual ASAR scenes have been made.

The model and ASAR wind maps were found to have a root mean square deviation of ~ 3.33 m/s and a correlation coefficient of 0.54. The RMSD is higher than that found in similar studies, and possible reasons include the data filtering process, the area's proximity to land and the model's relatively low resolution. The root mean square error of the wind model compared to in-situ observations for Fakken were ~ 4.22 m/s, and there was a large difference in variance indicating the the model could not capture the full variation in the wind climate. The in-depth analysis of individual scenes revealed several instances of wind features such as atmospheric gravity waves and wind shadowing which were present in the ASAR wind maps but absent or poorly defined in the model wind maps. Identifying the extent and location of features connected to turbulence or wind shadows can be essential to siting, and it was possible to identify several locations where special care should be taken in estimating the wind climate.

Contents

Chapter 1

Introduction

1.1 The need for wind estimation

The first offshore wind farm was established in 1991, off the coast of Denmark. In 2010 it had a total capacity of 4.05 MW. Since then, more offshore wind farms have been built, and by 2011 the total installed capacity in the EU area was 2 994 MW (The European Wind Energy Association, 2011).

Offshore wind power has several advantages over land-based wind farms, such as generally higher wind speeds and more stable wind conditions and large availability of area for siting (Manwell et al., 2010). A study from European Environment Agency (2009) attempted to establish the potential for wind power in Europe, and estimated the energy potential from offshore wind power in the EEA countries to be 30 000 TWh in 2030 with the current technology. This only includes coastal regions with a depth of up to 25 metres, as technological restraints at present for the most part limits the building to these areas. A study by the Norwegian Water Resources and Energy Directorate (NVE) in 2008 estimated that in Norwegian coastal areas up to 50 m depth, the potential wind power was as much as 55 300 MW . However, as the coast of Norway is generally quite deep, the area available for such siting is very close to land. (Hofstad and Tallhaug, 2008)

	Onshore investment cost (%)	Offshore investment cost (%)
Turbine	74–82	30–50
Foundation	1–6	15–25
Installation	1–9	0–30
Grid connection	2–9	15–30
Total turnkey investment costs	800–1 100 EUR/kW	1 200–2 000 EUR/kW

Table 1.1: Cost estimate for some aspects of onshore and offshore wind farms (European Environment Agency, 2009)

Clearly one of the disadvantages to offshore wind power is increased investment cost, as illustrated in table 1.1. Placement in deep water increases installation cost, makes higher demands on the structure due to the environmental conditions and potentially increased load, and makes maintenance more difficult due

to location and weather conditions. However, offshore wind parks have advantages when it comes to siting which can allow it to benefit from generally higher wind speeds than onshore. This advantage is useless if there is no knowledge of the wind conditions at a potential site. Onshore wind parks benefit from a (mostly) well-developed network of wind measurement stations which allow for a thorough evaluation of the optimal siting of a new wind park, but this is not necessarily the case for offshore. Wind ocean climates can vary considerably on a regional as well as local scale, and so a thorough investigation of the wind conditions is necessary.

Sempreviva et al. (2008) divides the resource assessment phase of wind farm projects into two stages; regional assessment and site-specific assessment. For the first stage, the use of meteorological models for simulation of wind conditions coupled with in-situ measurements from buoys and meteorological masts has been the prevailing method. However, meteorological masts and buoys can only provide spatially very limited data, and are also expensive (Hasager et al., 2007). It's hardly feasible to deploy ocean buoys or masts in every potential wind power site. An alternative method of estimating the wind conditions is by use of satellite Synthetic Aperture Radar (SAR). Ocean surface winds have been mapped in this manner since as early as 1978, when the SeaSat satellite launched with an L-band SAR. Regular and reliable data has been available since 1991 with the ERS-1 satellite. Continuous data, taken from an increasing number of satellites, has existed since then (Nielsen et al., 2004). Wind estimates from SAR provide information about a much larger geographical area than in-situ measurements can, and can be a cheaper option to installing masts or deploying buoys. However, the method has its own challenges, such as temporal resolution and accuracy. Therefore, it's interesting to have a closer look at the prevailing differences in estimating the local wind climate with model estimates versus SAR wind estimates.

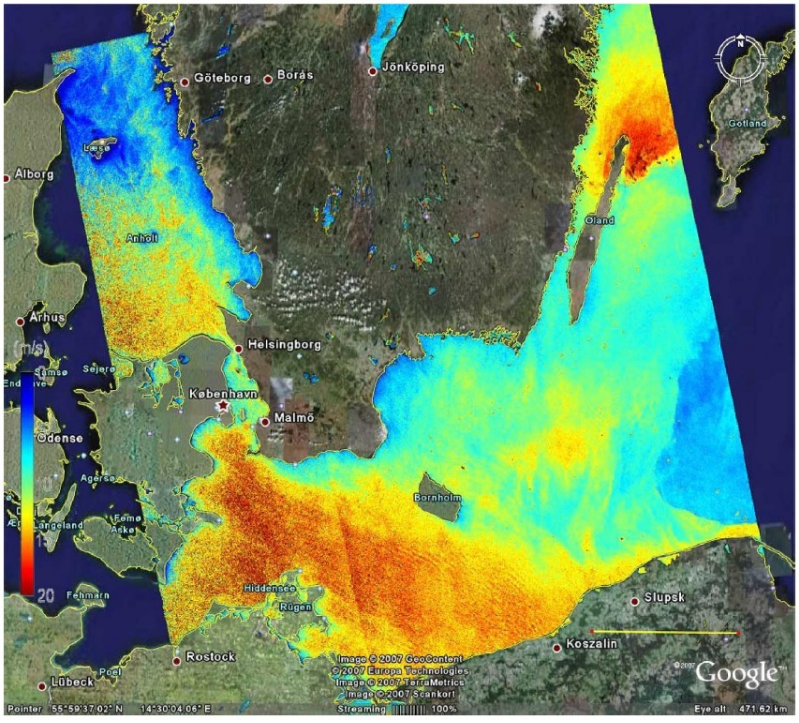

Figure 1.1: Wind map over the Baltic Sea from the Envisat ASAR. (Hasager et al., 2008)

1.2 Former research

An overview of the research which has led from the first wind measurements from the SeaSat in 1978, to an active use of SAR for wind farm siting in 2013, would be extensive and worthy of it's own book. Much has happened; from technical advances, with the development of new sensors, to steady improvement of the CMOD algorithms needed to "translate" radar backscatter to wind speeds, and increasing accuracy in deriving wind direction directly from the SAR image features. Many research areas come together to further the accuracy and applicability of offshore wind estimation with SAR, and they cannot all be detailed here. In the following section, a presentation of some of the main research projects into the use of SAR for wind estimation the past 10 years will be presented; many of them primarily with wind production in mind.

One of the first large studies into the use of SAR images for wind prediction was the US StormWatch project at the John Hopkins University of Alaska. The Radarsat ScanSAR images were acquired between November 1997 and through March 1998, and had a swath width of 440 km. The images covered a part of the US and Canadian east coast and a complete set of images covering the area was acquired every 24 days. The geophysical model used to aquire the wind speed estimates from the normalized radar cross section was the CMOD4, modified for HH-polarization. (Pichel and Clemente-Colón, 2000) Beal (2000) found that the SAR wind estimate in areas where they had in-situ measurements corresponded well both with the in-situ data and the model winds from the U.S. Navy Fleet Numerical Meteorology and Oceanography Center. In addition, spatial details in the wind fields could be seen in the SAR images which were not available in the model at the same resolution, and this could be coupled more easily to the on-shore terrain features which might influence the wind. Beal (2000) concluded that more research would be needed into the interactions between the variables in SAR imagery, such as radar frequency and polarization, boundary-layer stability, water surface tension, etc.. Also, uncertainties in the local wind direction used for the CMOD4 algorithm was identified as a potentially large source of error.

In 1999 - 2000 the Alaska SAR demonstration was conducted, also by the John Hopkins University of Alaska. The aim of the study was to look at the possibility of real-time wind estimation using SAR images. The project had access to roughly 12 wide-swath SAR images monthly, and coupled this with model wind directions from the US Navy's Naval Operational Global Atmospheric Prediction System (NOGAPS). The project managed to produce wind speed estimates in 5-6 hours of acquiring the SAR images, but as little as 2 hours was the desired result. One of the challenges described is the desire for near real-time wind direction input to the CMOD4-algorithm used to extract wind speeds. This was usually not available within a few hours of the SAR images, and so model wind direction predictions generated 12 hours previously were used.(Monaldo, 2000; Monaldo et al., 2001)

The SAR images used in the Alaska SAR demonstration as well as those from the StormWatch project have been analysed by Monaldo et al. (2001), who compared both to model data and in-situ wind measurements from ocean buoys. The SAR image pixels were averaged from 100 m to 600 m wind cells, and the NOGAPS model wind direction was linearly interpolated to match this. The resulting wind speed map was then averaged to a 50 km x 50 km grid to be more easily comparable to model winds. It was found that the wind speeds from SAR were increasingly underestimated compared to model estimates for incidence angles under 25°, and these images were excluded. The study looked at the effect of using different values for the α variable in the CMOD4 algorithm, and found the difference between SAR and model winds to be lowest for $\alpha = 0.6$. The mean standard deviation between SAR estimates and buoy measurements were found to be 1.06 m/s, with a bias of 0.85 m/s. Monaldo et al. (2001) also identified two of the main potential error sources as erroneous wind directional input to the algorithm, as well as a need for further development of the CMOD4 geophysical model itself. The mean difference between measured wind direction and modelled wind direction was 3°, with a standard deviation as large as 44°, which can lead to a large error in the

estimated SAR wind speed.

Another attempt to develop a tool for quicker and easier generation of offshore wind estimates was the Wind Atlas Analysis and Application Program (WaSP). WaSP was developed by the Department of wind energy at the Technical University of Denmark. It is used for estimation of wind climates and siting of wind turbines, amongst other things. WaSP combines model wind data with in-situ measurements, information about terrain, surface roughness and different obstacles to calculate the wind climate at a site. This can be used to produce a wind atlas of nearby sites or areas with largely similar wind climates. (Frank et al., 2001)

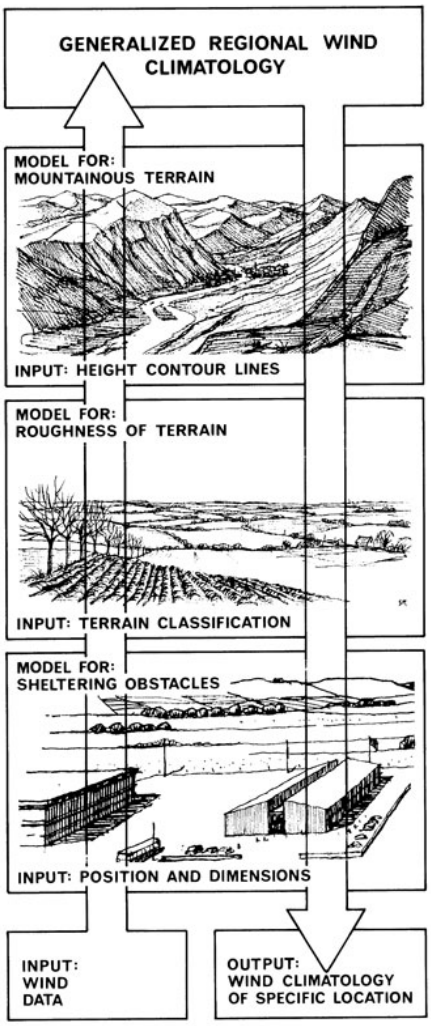

Figure 1.2: Illustration of the WaSP methodology. (Frank et al., 2001)

One of the largest studies done on offshore wind estimation from satellite is the SAT-WIND project by the Danish Risø National Laboratory at the Technical University of Denmark. The project ran from January

2004 until October 2006, and looked at various methods of estimating offshore wind through active and passive satellite-based remote sensing, including SAR. They developed the Satellite - Wind Atlas Analysis and Application Program (S-WASP), which calculates wind resource statistics from SAR wind estimates. The tool is limited to wind speeds between 2 and 24 m/s, as this is the range for which SAR can reliably be used to estimate wind speeds. (Hasager et al., 2007; Barthelmie and Pryor, 2003; Nielsen et al., 2004)

The Wind Energy Mapping using Synthetic Aperture Radar-project (WEMSAR) in the early 2000s attempted to develop a tool which could be used for optimal offshore wind park siting by combining the available data in an efficient way. The project combined the S-WaSP-program with input from the regional scale Karlsruhe Atmospheric Mesoscale (KAMM) model, with wind estimates from ERS 1 and 2 as well as RADARSAT. The SAR images used were taken over several different locations in Europe, namely the west-coast of Norway, Horns Rev outside Denmark as well as Sardinia in Italy, with a total of 72 scenes. The WEMSAR tool retrieves wind direction from the SAR image spectra or in-situ measurements and compute wind speeds using the CMOD-4 or CMOD-IFR2 algorithms (Furevik et al., 2003). Another program called the Risor WEMSAR Tool was developed at Risør to calculate further wind climate statistics, such as fitting of the Weibull distribution. (Hasager et al., 2005)

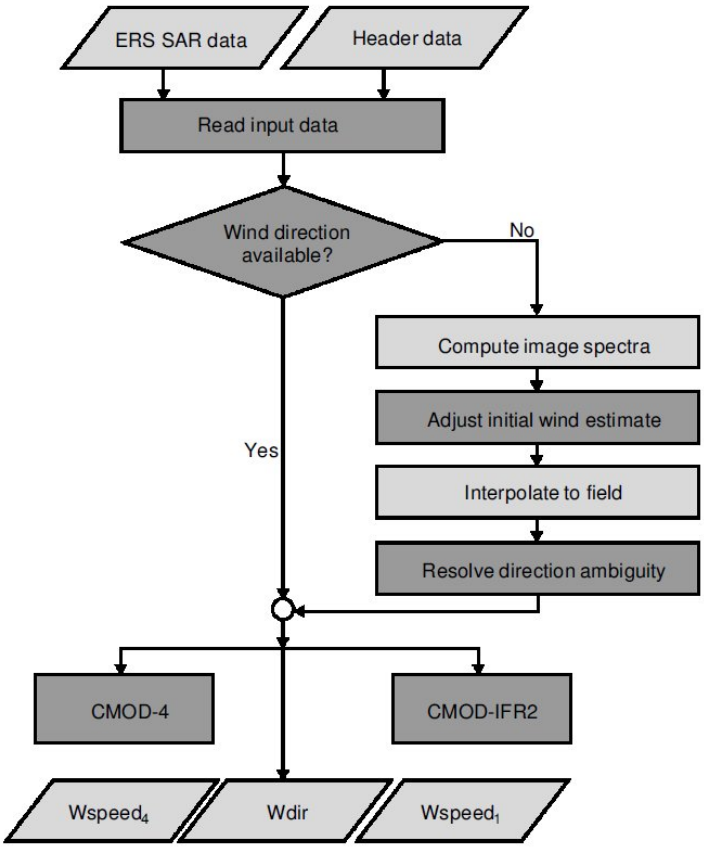

Figure 1.3: Illustration of the workflow of the WEMSAR tool. (Furevik et al., 2003)

In Canada, Beaucage et al. (2007) used the MC2 mesoscale model with a resolution of 4 km, which was run self-nested to get a grid-point spacing of 1 km. This was compared to SAR wind speeds with a final wind cell size of 400 m. Since the SAR data was truncated to between 2m/s - 25 m/s, model data points with winds outside this range was also removed. Wind directions for the SAR wind estimates were acquired both from the model and the QuickSCAT scatterometer, and the two methods didn't give significantly different results, with a rms error of 2.07 m/s and a bias of -0.13 m/s for wind speeds, and rms error of 16.3° and a bias of -5.7 ° for wind direction. They considered both model and asar wind estimates to be reliable after comparing with in-situ measurements. They point out that individual SAR wind estimates are somewhat more inhomogeneous than the model winds, and that topographical and sea surface characteristics might be the reason for this.

A study by Espedal et al. (2001) examined typical spatial wind variations in a coastal area outside Bergen, Norway using five SAR images chosen based on a representative wind direction for the area. The purpose of the study was to identify dominant wind features as an aid in wind farm siting. They point out that the CMOD-IFR2 model was developed for stable atmospheric conditions, and as such might be inaccurate for different conditions. The study used wind directional input from the SAR images, acquired using fast fourier transform, with supplements from nearby onshore in-situ measurements where necessary. They found that though areas further from the coast usually have higher wind speeds than coastal areas, this is not the case for wind directions parallel to the coast. Furthermore, better wind conditions were found near the mouth of a fjord. In general, it is concluded that a detailed analysis of SAR images gives a good basis for selecting areas which should be investigated further.

Attempts to use ASAR wind estimates specifically for wind farm siting have already been made. (Schneiderhan et al., 2005) describe the use of ERS-2 satellite SAR images to evaluate the Horns Rev wind farm off the coast of Denmark and try to compare the spatial variability of the wind climate with another wind farm, Butendiek, also in the North Sea. Their study showed that the assumptions about the wind climate at Butendiek were erroneous and that the wind potential was higher than earlier expected.

1.3 The aim and purpose of the study

The aim of this study is to compare ASAR wind estimates with model wind estimates for a coastal area in northern Norway. There are no offshore in-situ measurements available for this area, and so it is not possible to estimate the accuracy of either method. But as both methods are relevant tools for a first-estimate of wind conditions at a potential site, a central topic will be to compare how the wind estimates vary spatially in complicated coastal terrain. With the purpose of offshore wind production in mind, particular attention will be given to advantages and shortcomings of these methods in relation to each other, and difficulties presented to each by the geography of the area. This will be done both through statistical analysis to examine temporal features relevant to a coastal area, such as seasonal or diurnal basis, and a qualitative examination of selected ASAR scenes to investigate the effect of wind climate and spatial features on the estimates.

1.4 Organization of the study

This study is organized into seven chapters. Chapter two will describe the theoretical basis of the study, with background information about wind theory and wind power production, SAR theory and remote sensing and measurement of offshore wind and numerical weather prediction. Chapter three contains a description of the location, time frame and data used, as well as pre-processing and methods used for analysis. Chapter four

contains a detailed presentation of all the results, with a discussion of these results presented in chapter five. The final conclusion and suggestions for further study can be found in chapter six.

Chapter 2

Theoretical background

2.1 Wind theory

2.1.1 Power of the wind

Manwell et al. (2010) describes the available power in the wind through a section such as a rotor disk with area A as

$$\frac{dm}{dt} = \rho A v \tag{2.1}$$

where ρ is the density of the air and U is the air velocity. The kinetic energy per unit time, P, then becomes

$$P = \frac{1}{2}\rho A U^3 \tag{2.2}$$

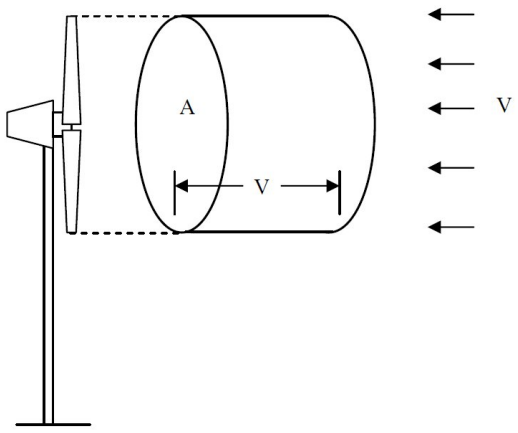

Figure 2.1: Airflow with wind velocity V through a disk with area A.(Mathew, 2006)

The wind power density, or the wind power per unit area, is defined as

$$\frac{P}{A} = \frac{1}{2}\rho U^3 \tag{2.3}$$

As shown above, the power in the wind is not only dependent on the velocity of the wind, but also on the density of it. This varies by both temperature and pressure, which again varies with height. Manwell et al. (2010) gives an expression for the density of the air:

$$\rho = \frac{p}{RT} = 3.4837\frac{p}{T} \tag{2.4}$$

where T is the temperature in Kelvin and p is the pressure in kPa. In practice, the temperature changes of a location have a larger impact on the density than pressure changes.

Wind distribution

The wind speed probability density function describes the probability that the wind speed has a particular value. It is possible to use a Rayleigh distribution to represent wind speed, and it is the easiest option since the only variable is the mean wind speed. However a better and more accurate option is the Weibull distribution, which is dependent on a shape factor k and a scale factor A. Different sources has been used in the following section which employ different names for these variables, but these will be used consistently here. As illustrated in figure fig. 2.2, for k = 1, we get an exponential distribution, for k = 2 we get a Rayleigh distribution and for k = 3.6, it approaches a Gaussian distribution. (Pavia and O'Brien, 1986)

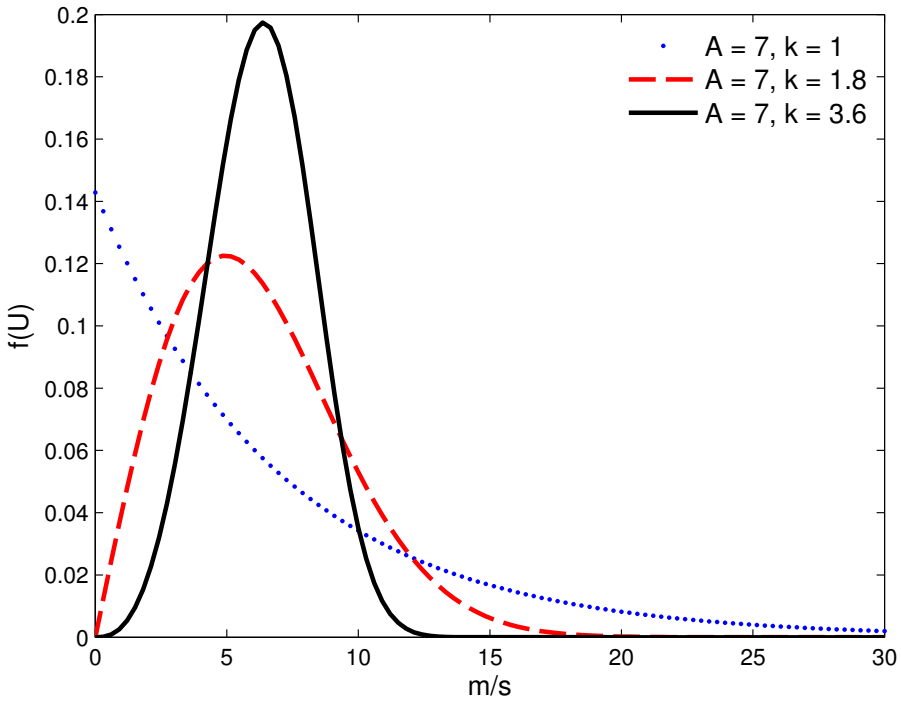

Figure 2.2: Weibull density function for different values of k.

Pryor et al. (2004) describe the following attributes of the Weibull distribution:

Probability density function

$$p(U) \equiv \left(\frac{k}{A}\right)\left(\frac{U}{A}\right)^{k-1} e^{-\left(\frac{U}{A}\right)^k} \tag{2.5}$$

for U $\geq$ 0, A $>$ 0 and k $>$ 0.
The moments as given by Pavia and O'Brien (1986) are:

Non-central moments

$$m_m = \int_0^\infty p(U)U^n dU = A^n \Gamma\left(1+\frac{n}{k}\right), \tag{2.6}$$

where Γ is the gamma function, and the lower order moments can be given as

Mean

$$\overline{U} = A\Gamma\left(1+\frac{1}{k}\right) \tag{2.7}$$

Variance

$$\sigma^2 = A^2\left(\Gamma\left(1+\frac{2}{k}\right) - \Gamma^2\left(1+\frac{1}{k}\right)\right). \tag{2.8}$$

Pryor et al. (2004) looked at different methods for deriving these parameters, such as moment fitting methods, maximum likelihood estimation, least squares fit and more. Both the moments II and maximum-likelihood methods were found to give good fits, but higher wind speeds gave more precise estimates than lower ones. The approximations based on the second order moments are for the shape parameter k

$$\frac{\Gamma\left(1+\frac{3}{k}\right)}{\Gamma^3\left(1+\frac{1}{k}\right)} = \frac{\overline{U^3}}{\overline{U}^3} \tag{2.9}$$

and the scale parameter A is

$$A = \frac{\overline{U}}{\Gamma\left(1+\frac{1}{k}\right)} \tag{2.10}$$

Cohen (1965) derives the maximum likelihood estimator, starting with the likelihood function (original notation uses k = γ, $A = \theta$ and U = x)

$$L(U_1,...,U_i;k,A) = \prod\left(\frac{k}{A}\right)U_i^{k-1}e^{-\frac{U_i^k}{A}} \tag{2.11}$$

From this we can find the estimating equations

$$\frac{\partial \ln L}{\partial k} = \frac{n}{k} + \sum_i^n \ln U_i - \frac{1}{A}\sum_i^n U_i^k \ln U_i = 0 \tag{2.12}$$

$$\frac{\partial \ln L}{\partial A} = -\frac{n}{A} + \frac{1}{A^2}\sum_i^n U_i^k \tag{2.13}$$

which can be used to eliminate A and give the maximum-likelihood approximations to k and A, respectively:

$$\left[\frac{\sum_1^n U_i^k \ln U_i}{\sum_1^n \ln U_i} - \frac{1}{k}\right] = \frac{1}{n}\sum_1^n \ln U_i \tag{2.14}$$

$$A = \sum_i^n \frac{U_i^k}{n} \tag{2.15}$$

These are given on a slightly different form by (Pryor et al., 2004):

$$\frac{n}{k} + \sum_{i=1}^n \ln U_i - \frac{n\sum_{i=1}^n U_i^k \ln U_i}{\sum_{i=1}^n U_i^k} = 0 \tag{2.16}$$

$$A = \sqrt[k]{\frac{1}{n}\sum_{i=1}^n U_i^k} = 0 \tag{2.17}$$

Given the Weibull distribution we can calculate the available wind power density

$$E = \frac{1}{2}\rho A^3 \Gamma\left(1 + \frac{1}{k}\right), \tag{2.18}$$

where ρ is the air density and Γ is the gamma function (Barthelmie and Pryor, 2003).

2.1.2 Wind in coastal areas

As mentioned earlier, offshore wind parks are for the moment dependant on being placed reasonably close to the coast, in depths up to 25 metres, due to both technological and financial restrictions. This means that although offshore wind parks generally benefit from higher winds than onshore, the wind climate is often more complicated.

Atmospheric stability and variation with height

Wind shear or wind gradient can be described as the difference in mean wind speed over a certain distance, and the mean wind speed tends to increase with height. In the planetary boundary this is to a large extent due to surface friction. This is relevant to wind resource assessment because the mean wind speed might need to be corrected in relation to altitude when using measurements taken from different elevations. Manwell et al. (2010) describes two different mathematical models which are used to model the vertical profile of wind speeds. The logarithmic wind profile is given by

$$U(z) = \frac{U^*}{k} ln\left(\frac{z}{z_0}\right), \tag{2.19}$$

where $U^* = \sqrt{\frac{\tau_0}{\rho}}$ is the friction velocity, k is the von Karman's constant and z_0 is the surface roughness length. For calm seas, z_0 has a value of 0.20 mm, and for a blown sea 0.50 mm.

The power law profile in its basic form is

$$\frac{U(z)}{U(z_r)} = \left(\frac{z}{z_r}\right)^\alpha \tag{2.20}$$

where $U(z)$ is the wind speed at height z, $U(z_r)$ is the reference wind speed at height z_r and α is the power law exponent. α is highly variable, and may be chosen empirically to fit the wind data.

The wind gradient is also dependant on atmospheric stability, which again is dependant on height over the ocean and decreases with increasing heights. Barthelmie et al. (2009) gives a modified expression for the power law wind profile which takes atmospheric stability into account:

$$U_z = \frac{U^*}{k}\left[ln\frac{z}{z_0} - \Psi_m\left(\frac{z}{L}\right)\right] \tag{2.21}$$

where Ψ_m is a stability term dependant on the height z and the Monin-Obukhov length L. A large L indicates neutral conditions and a lower contribution to the wind gradient.

Changes to heat flux has a greater effect on the atmospheric stability offshore than mechanically generated turbulence due to the low surface roughness, and this in turn has a greater effect on the low-level wind speeds (up to 8 m/s). Figure 2.3 shows the frequency of wind speeds compared to atmospheric stability for the Vindeby wind farm in Denmark.

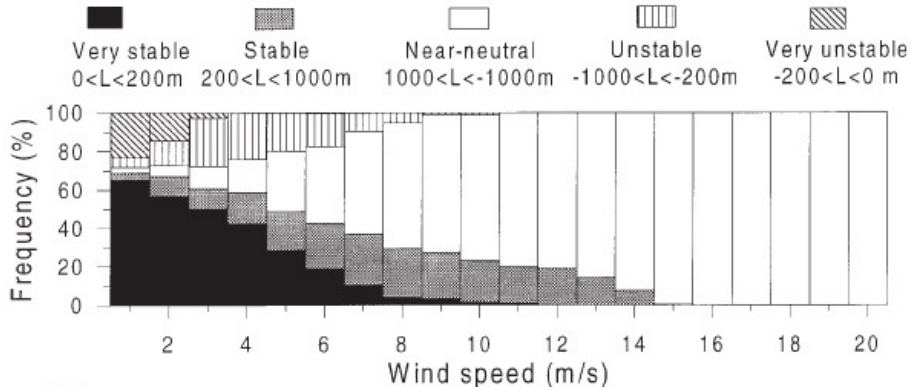

Figure 2.3: Wind speed and atmospheric stability for the Vindeby wind farm (Barthelmie et al., 2009).

On land, diurnal cycles affect the wind to a much larger extent than offshore, where the sea surface temperatures are far more stable than the air temperatures. However, in coastal areas it is sometimes possible to find a weaker diurnal cycle that is either shifted or inverse to the one found on land - i.e. with highest wind speeds found around midnight. (Barthelmie et al., 1996) The wind gradient and its effect on atmospheric instability is much greater offshore than on land, and is a large factor in wind forecasting. A lag in changes to ocean temperatures compared to air temperatures means that seasonal changes in atmospheric stability are slightly different offshore than onshore. Stable conditions are in northern Europe common in the spring, while autumn and winter are characterized by unstable atmospheric conditions. (Barthelmie et al., 2009)

Observing the wind by the waves

The mass of an ocean wave will move in a circular motion with little net forward movement. For deep ocean waves, where the depth of the water is much larger than the wave's wavelength, the expression for the wave velocity is

$$v = \sqrt{g}\left(\frac{\lambda}{2\pi}\right)^{\frac{1}{2}} \tag{2.22}$$

where g is gravity, λ the wavelength and d the depth of the water. When the wavelength is larger than the depth, this expression becomes

$$v = \sqrt{g}d^{\frac{1}{2}}. \tag{2.23}$$

(da Rosa, 2005)

Figure 2.4 shows the wave height as a function of the fetch (how far the wind has blown over the given stretch of water) and duration of the wind. Wind speed and fetch are essential to wave height.

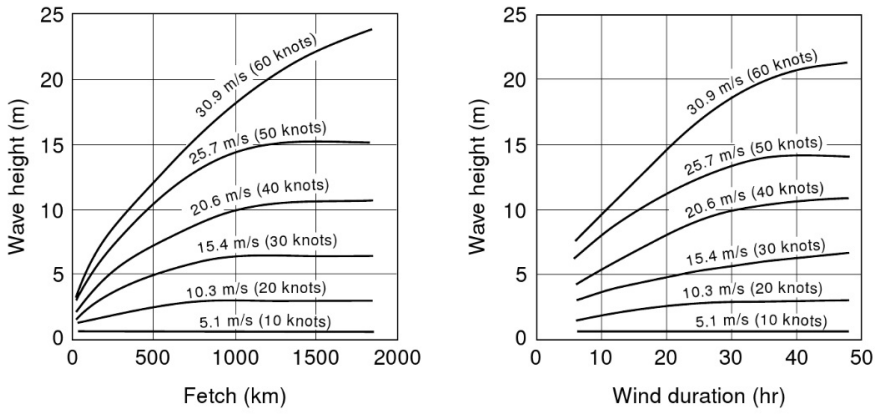

Figure 2.4: Wave height (da Rosa, 2005)

The wave types that result from the wind over the ocean are called capillary waves (wavelengths shorter than 1.79 cm) and gravity waves (wavelengths over few cm). Capillary and short gravity waves are the waves that are observed with satellite remote sensing, and are coupled to Bragg scattering (Richards, 2009). This process is essential to wind observation and estimation with satellite SAR, and will be described in more detail in section 2.2.3.

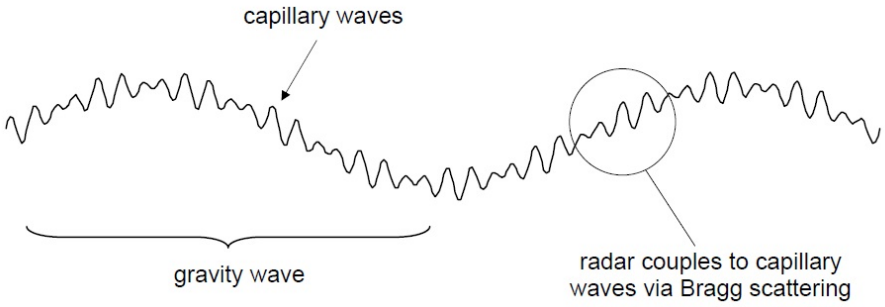

Figure 2.5: Illustration of capillary and gravity waves (Richards, 2009)

Topographical and atmospheric features in SAR

Atmospheric gravity waves can be caused by the air moving over objects, such as mountains and islands, or by wind shear and the intersection of hot and cold air. They appear as streaks of alternating wind speeds nearly perpendicular to the wind direction in SAR images (usually rotated around 18° clockwise to the wind direction), and have a wavelength on the order of a few kilometres. They are connected to potentially strong turbulence and rotors, and have been know to pose a hazard to air crafts. These conditions can subsist for up to 18 hours and extend as far as 50 km offshore. (Worthington, 2001, 2002; Hertenstein and Kuettner, 2005).

The effect of atmospheric turbulence on wind power production has not been extensively studied, but recent studies indicate that turbulence can have as strong an impact on production and fatigue as wake effects, and can cause fatigue loading which can severely impact the lifespan of a turbine (Churchfield et al., 2012; Brand et al., 2011). However, turbulence is also a key to reducing wake effects, and so it's important that the nature and frequency of the turbulence at a site is understood.

Internal ocean waves with large wavelengths (up to 20 km) will also appear with a similar pattern, as the circular motion of the wave dampens the capillary waves. (Tonboe, 2001; Christiansen, 2006)

2.1.3 Mechanics of a wind turbine

Wind resources offshore are generally greater than on-shore, and this provides an opportunity for greater wind power production. All wind turbines experience large loads on the turbine rotors, but offshore turbines are generally exposed to a more demanding climate. For wind turbines mounted on floating structures, there is an additional load from wave-induced motion and gravity due to changing directions.

The blade of a wind turbine is an aerofoil and functions much as an aeroplane wing. The air moving faster over the curved top of the blade than under it, creates a lift force which has a component in the rotor plane. This causes the rotor to turn and generate power.

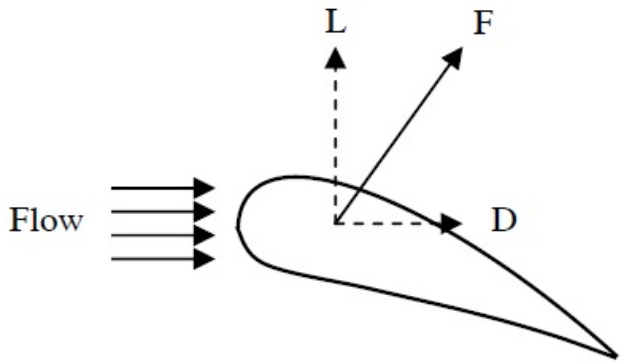

Figure 2.6: Lift and drag force on a turbine blade (Mathew, 2006)

This lift force is given by Mathew (2006) as

$$L = C_L \frac{1}{2} \rho_a A V^2, \tag{2.24}$$

where ρ_a is the density of the air, V is the speed of the air, A is the area of the aerofoil and C_L is the lift coefficient. The lift coefficient is dependent on the angle of attack, and the optimal angle will vary depending on the aerofoil. An indication of the amount of energy that can be extracted from the air by the wind turbine is the axial induction factor, a, which is a measure of how much the rotor slows the speed of the wind as it passes by it. This can be used to express the ratio of power the wind turbine extracts in relation to the theoretical power in the wind as

$$C_p = 4a(1-a)^2. \tag{2.25}$$

Solving the differential equation

$$\frac{dC_p}{da} = 0 \tag{2.26}$$

gives us the maximum theoretical power coefficient, $16/27 \approx 0.59$, which is also known as the Betz limit (Mathew, 2006). If we combine this with the expression for the kinetic energy of the wind in eq. (2.2), we get the actual energy available to the turbine, which is

$$P = \frac{16}{27}\frac{1}{2}\rho U^3. \tag{2.27}$$

Another factor that influences the efficiency of a wind turbine is the *tip-speed-ratio*

$$\frac{R\Omega}{u}, \tag{2.28}$$

where R is the blade length, Ω the the angular speed of rotation and u is the wind speed (Twidell, 2009). The speed of the rotation is very important, as too low a speed will result in the wind passing between the blades without affecting them, and too high a speed will result in the wind being forced around the outside of the blade radius. The tip-speed-ratio affects the power coefficient and torque coefficient of a wind turbine, and ideally the tip-speed-ratio should remain constant at the optimal rate regardless of wind speed. With traditional generators, *fixed speed* operation has been necessary to produce constant frequency power despite a 20 % production loss; however, with newer generators, such as are generally applied in offshore wind farms, *variable speed* operation is possible, where the rotation speed varies with the wind speed.

An estimate of wind speed distribution and mean wind speed for the site of the wind farm is used to estimate optimal blade tip speed, and to select the appropriate mechanical and electric components for the wind turbines. Since the power in the wind increases with the cube of the wind speed, a good estimate of the wind speed for a site is crucial for the wind turbines to function at their best and to avoid employing wrongly dimensioned turbines (Twidell, 2009).

The power curve of a wind turbine shows the expected power output depending on wind speed, and fig. 2.7 shows an example power curve based on data on the Vestas V112-3.3 MW IEC 1B turbine from Vestas (2013). Based on the usual distribution of wind speeds, the optimal wind speed in terms of power production is 12 m/s. An example of this can be seen in fig. 2.8, where the Weibull probability density function has been fitted to 5 years of wind measurements from Torsvåg Fyr, situated on the north-eastern part of Vannøya. This has then been used to calculate the theoretical power available in the wind, which is plotted as a percentage of maximum theoretical power available, with the peak at 12 m/s as 100 %. We see that most of the energy can be found in the range between 8 m/s and 20 m/s, with very little under 4 m/s and over 24 m/s (Lynn, 2012). Shown in fig. 2.7 are the cut-in and cut-out wind speeds for the Vestas turbine, which are the wind speeds at which the turbine will start and stop. The cut-out speed is to protect the turbine from the extreme loads at high wind speeds, but as fig. 2.8 illustrates, this will not lead to significant losses in production.

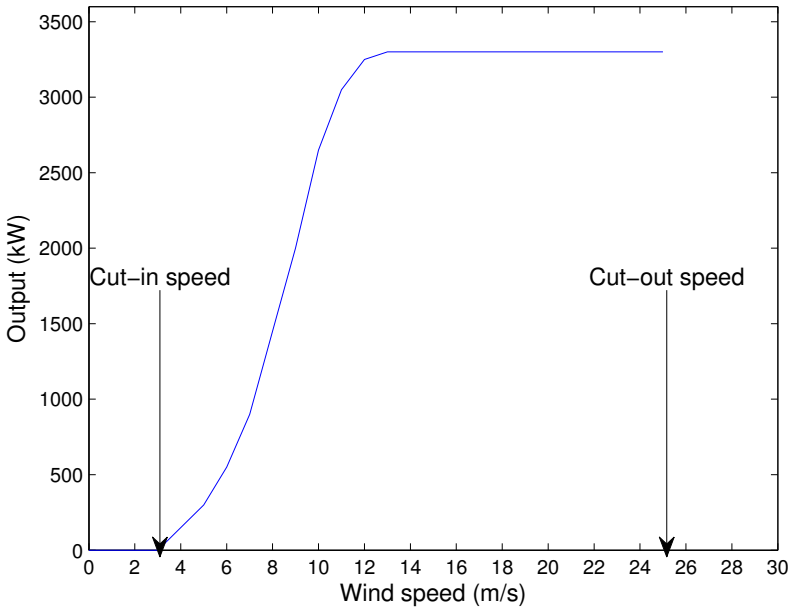

Figure 2.7: Example power output curve from a Vestas V112-3.3 MW IEC 1B turbine.

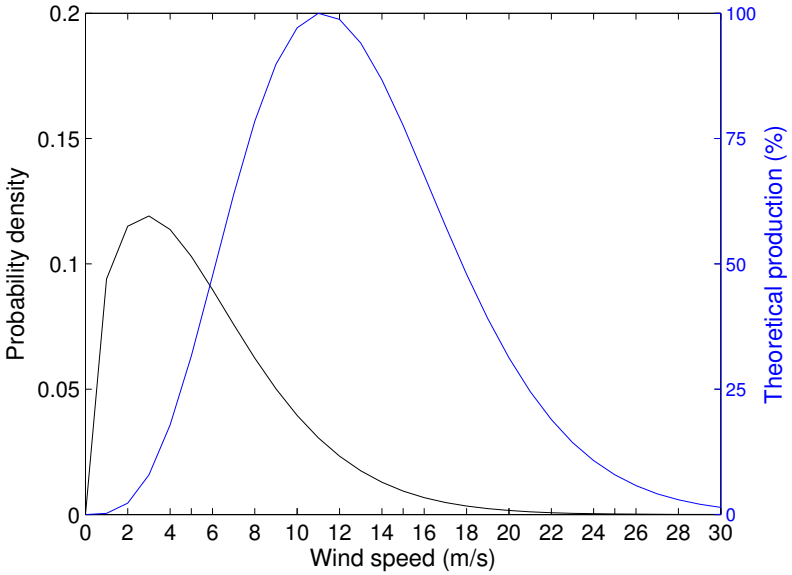

Figure 2.8: Probability density function and theoretical power for Torsvåg Fyr.

Wake effects

As the wind passes through the rotor blades of a wind turbine and gives up some of its energy, this naturally means that there will be less energy available in the wind for the wind turbine further down the line to extract. Another wake effect is the turbulence created as the wind gains some rotation from its interaction with the wind turbine. This will reduce the power coefficient of the downwind turbine. Wake effects will to a some degree be stabilized as kinetic energy is restored from the surrounding wind, but this is dependant both on the distance the wind moves (which is dependant on the spacing of the wind turbines), as well as the atmospheric turbulence. (Barthelmie et al., 2009)

Figure 2.9: Wake effects at the Horns Rev offshore wind farm in Denmark. (Steiness, 2013)

2.2 Synthetic aperture radar theory

A radar system works by emitting microwave pulses which are backscattered from the ground and recorded by the radar. The radar system is best described by the radar equation,

$$P_r = \frac{P_t A_e^2 \sigma}{4\pi\lambda^2 R^4} \tag{2.29}$$

where P_r is the signal power received by the radar, P_t is the power transmitted by the radar, A_e is the effective area of the antenna, σ is the radar cross section of the target, λ is the transmitted wavelength and R is the range. This simplified version of the radar equation doesn't take into account important elements like probability of detection and parameter uncertainties, but it shows the element of interest with regards to wind detection: the radar cross section σ, which will be described in more detail later.

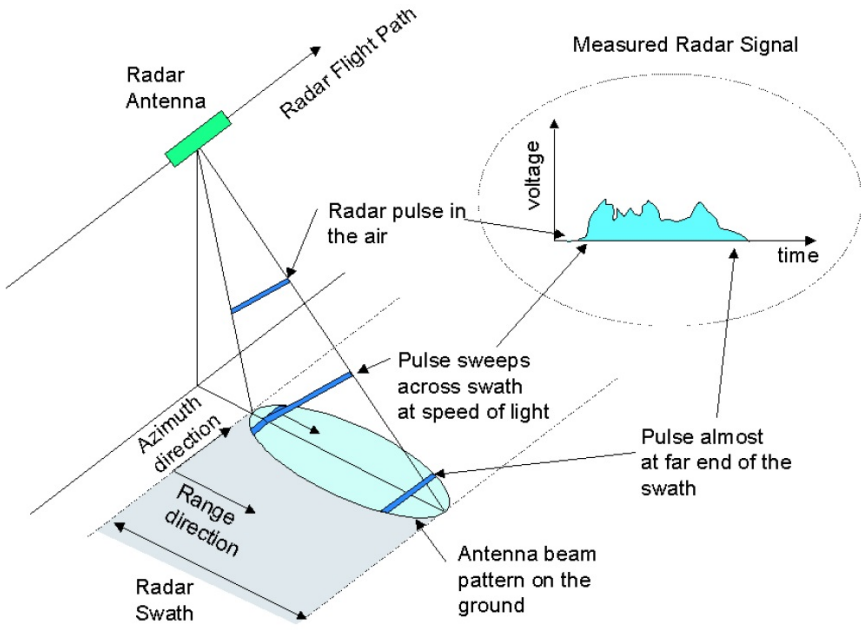

Figure 2.10: Illustration of Imaging SAR operation (Elachi and van Zyl, 2006)

The across-track area illuminated by the antenna beam is referred to as the swath, and the points in the beam that lie furthest away in relation to the radar nadir, will take longer to reach the radar sensor. This time delay can be used to divide the surface into range bins, which allows us to place the signal backscatter source in the range direction. Each range bin is equal in size to the antenna footprint in azimuth direction (Elachi and van Zyl, 2006).

2.2.1 Resolution

The range resolution is the shortest distance between two objects at which they can be identified as separate. If the signal reflected from one object should overlap with that reflected from another, they will not be separable. Therefore the range resolution is dependent on the pulse length, which itself is dependant on the frequency. An expression for the radar resolution is

$$r_{range} = \frac{c}{2Bsin\theta}, \tag{2.30}$$

where c is the speed of the electromagnetic energy, B is the spectral bandwidth and θ is the angle of incidence. To get the best possible resolution it is desirable with a long pulse as well as wide bandwidth, but as bandwidth is defined as

$$B = \frac{1}{\tau}, \tag{2.31}$$

this does not work out well. A solution is to modulate the signal ('chirp'), where the frequency f_0 of the signal is changed linearly to $f_0 + \delta f$ so that the bandwidth as given by Elachi and van Zyl (2006), now independent of τ, becomes

$$B = |(f_0 + \Delta f) - f_0| = |\Delta f|. \tag{2.32}$$

With this method the signal can be compressed so that the pulse has the same energy, but is much shorter.

For long distances such as is the case for space-born radars, the spatial resolution with a real aperture radar will become very low. This can be solved with the use of synthetic aperture radar. In a SAR, the coherently recorded signal is used to synthesize a virtual antenna, which allows for a much larger resolution. As the array footprint on the ground will be increased as the height increases, this will result in a longer synthetic array and a finer beam, thus offsetting the effect of the height on the resolution. The array footprint, or azimuth resolution, can be expressed as

$$X_a = \frac{L}{2}. \tag{2.33}$$

2.2.2 Polarization

The polarization of an electromagnetic wave can be described as the vector component of the amplitude of the electric field as described by the equation given by (Elachi and van Zyl, 2006):

$$\mathbf{E} = \mathbf{A}e^{i(kr-\omega t+\phi)}, \tag{2.34}$$

where k is the wave vector in the propagation medium, ω is the angular frequency and ϕ is the phase. The amplitude A can be expressed as

$$\mathbf{A} = a_h e^{i\delta_h}\hat{\mathbf{h}} + a_v e^{i\delta_v}\hat{\mathbf{v}}, \tag{2.35}$$

where $\hat{\mathbf{h}}$ and $\hat{\mathbf{v}}$ are orthogonal basis vectors. The polarization of a wave transmitted by the radar antenna can be modified upon being scattered by a surface, and this modification can be described by a 2x2 scattering matrix [S]. The power received by the antenna can be expressed as the magnitude squared of the voltage, given by the scattering matrix and the normalized polarization vectors of the transmitting and receiving radar antennas, or

$$P = VV^* = |\mathbf{p}^{rec} \cdot [\mathbf{S}]\mathbf{p}^{\mathbf{rad}}|^2. \tag{2.36}$$

2.2.3 Scattering

The radar receives the energy that is scattered back from the object that we wish to observe. The backscatter is strongly dependant on the surface roughness, which can be characterized by the surface standard deviation relative to an average flat surface, as well as the surface deviation at a given point relative to that of other points in the surface. The model commonly used to describe backscattering in relation to wind measurements, is the small-perturbation model, also called the Bragg model, which regards the surface roughness as small perturbations on a flat surface (Elachi and van Zyl, 2006).

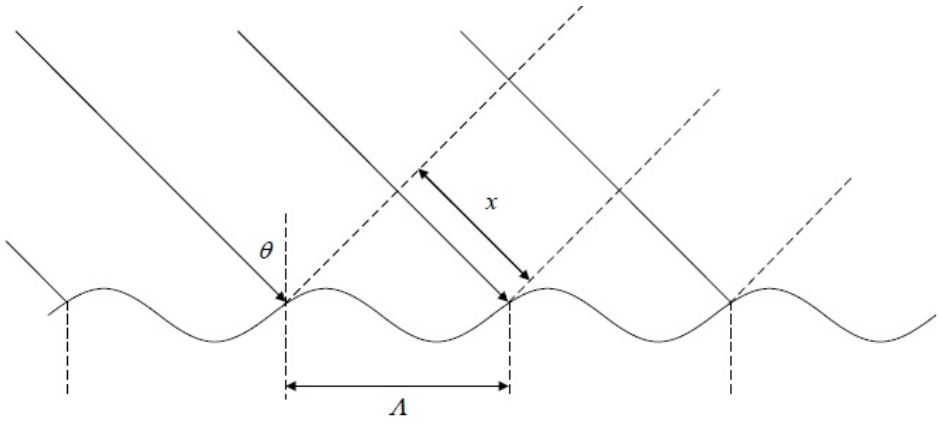

Figure 2.11: Illustration of Bragg Scattering (Richards, 2009)

The radar signal will be backscattered from the regularly spaced waves with a phase difference depending on the distance travelled to the surface, and when adding the returning signal within a pixel, this regularity will cause signals that have a phase difference that is a multiple of 2π to reinforce each other. The condition for Bragg scattering is given by Richards (2009) as

$$\Lambda = \frac{n\lambda}{2sin\theta}, \tag{2.37}$$

where Λ is the wavelength of the spatial surface, in our case the capillary waves, λ is the radar signal wavelength, and θ is the incidence angle.

Normalized Radar Cross Section

The returning signal to the sensor when it backscatters from an object is described by the Radar Cross Section (RCS), also called the backscattering cross section, which is defined as the ratio between the power reflected back to the radar per unit solid angle, to the incident power density, and in its simple form it can be written as

$$\sigma = 4\pi R^2 \frac{|E_r|^2}{|E_i|^2}, \tag{2.38}$$

where E_i is the power of the incident wave and E_r is the power of the scattered wave. It is usually given as

$$\sigma = 10log(\text{energy ratio}). \tag{2.39}$$

The radar cross section varies depending on the wavelength and polarization of the signal, the viewing angle, as well as characteristics of the object being viewed, and the different types of scattering the combination of these create (Skolnik, 2001). In wind detection application, the Normalized Radar Cross Section (NRCS),

$$\sigma_0 = \frac{\sigma}{\triangle A} \tag{2.40}$$

is used. $\triangle A$ is the area of the illuminated surface. The NRCS is proportional to the wave height spectral density of the capillary waves which result in Bragg scattering, which is the dominant type of scattering for

incidence angles of $20^\circ - 70^\circ$. However, other factors such as spatially varying current fields, modulation of the Bragg waves by longer waves, and the polarization of the radar signal also affect the NRCS. There is also an asymmetry to the NRCS for opposing look directions (i.e. upwind/downwind) for the same capillary waves. Improved models for the NCRS which take these factors into account has been presented by several sources (Romeiser and Alpers, 1997; Romeiser et al., 1997; Kudryavtsev et al., 2003, and more) and will not be described here.

Wind direction can also be connected to the NRCS, as the capillary waves tend to move with the wind. This means that when the wind direction is opposite to the radar look direction, the NRCS will be maximized, and it will be minimized for wind directions perpendicular to the look directions. For the case when the look direction and wind directions are the same, there is a small local maxima (Young et al., 2007).

2.2.4 Wind detection with SAR

The SAR most commonly used for wind detection use a C-band sensor, though L ($\sim$ 1.2 GHz) and X ($\sim$10 GHz) can be used, and can have resolutions as fine as 25 $\times$ 25 meters and a swath width of 100 km. This means that a SAR can give far more detailed wind maps than a scatterometer, and is more functional for use in coastal regions.

The satellite images used in this study come from the Envisat satellite. It operated between March 2002 until April 2012, when the European Space Agency (ESA) lost contact with it and declared the end of its mission. It had a sun-synchronous orbit at an altitude of 800 m, and the sensor used for wind detection was the C-band Advanced SAR (ASAR). The ASAR is an active phased array with incidence angles between 15° and 45°, and records in both high-resolution ($<$ 100 km swath with 30 m resolution) and wide-swath (405 km), as well as an alternating polarization mode (VV, HH,VV/HH, HV/HH, or VH/VV). The repetition time for high-resolution was $\sim$10 days, and $\sim$3 days for wide-swath and polarization mode.(Hasager et al., 2007; European Space Agency, 2012)

Lin et al. (2008) presents the process from SAR image to wind speed map quite succinctly in figure 2.12.

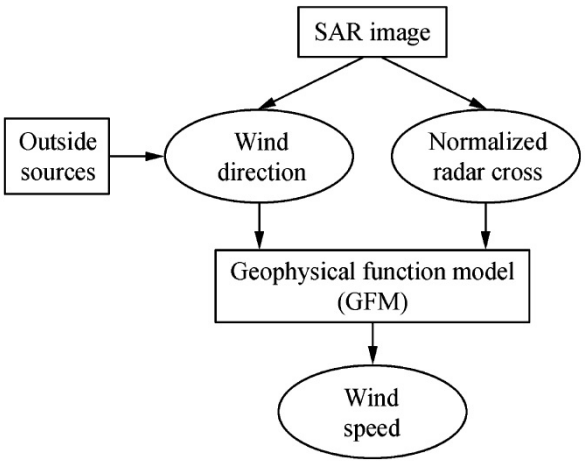

Figure 2.12: Outline of process from SAR image to wind speed map (Lin et al., 2008).

Before SAR images can be used for wind estimation, radiometric and geometric corrections and calibration must be performed. A compromise must be made between resolution and speckle reduction. All of this can be done with dedicated software, such as the BEST program supplied by ESA. The image can be converted into a wind speed map with the use of dedicated tools described in section 1.2, such as the WEMSARTool or S-WaSP. They all apply as their main tool a geophysical model function to translate the NRCS into wind speeds.

CMOD

To find a link between the wind speed and the backscatter coefficient σ_0, it is necessary to use a Geophysical Model Function (GMF) to find a modelled backscatter coefficient $\sigma_0^{(m)}$, which takes into consideration the signal's frequency, polarization and incidence angle. The C-band Model Functions (CMOD), CMOD4, CMOD5 and CMOD-IFR2 are such models. Though created for C-band scatterometers, modified versions exist both for advanced scatterometers and C-band SAR. The CMOD function solutions are not unique for each value of σ_0, but rather depends on the incidence angle and wind direction input as well, as illustrated in fig. 2.13.

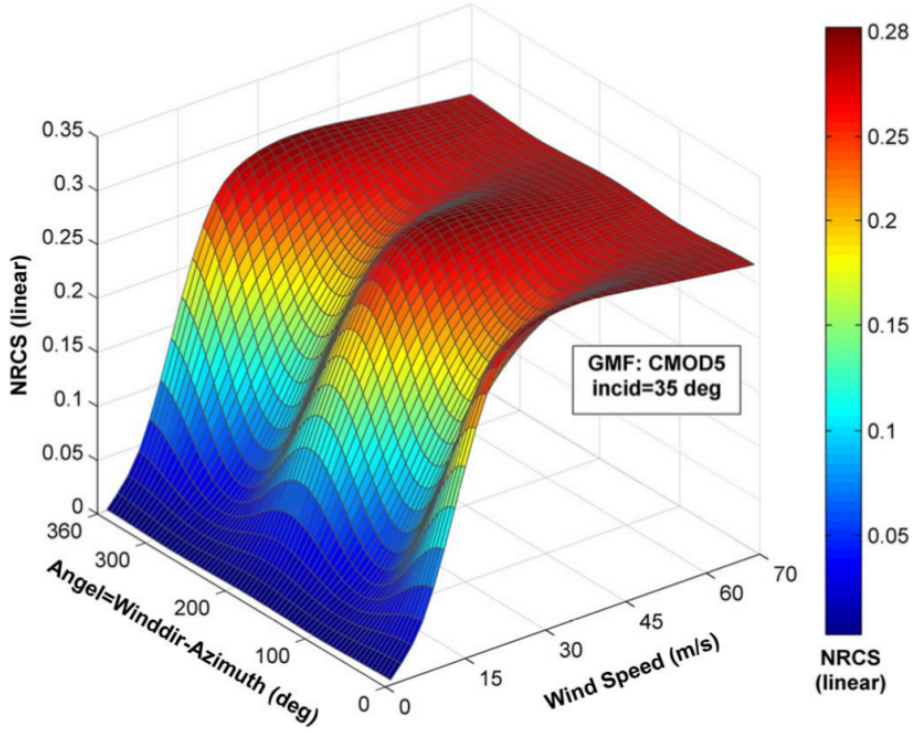

Figure 2.13: CMOD-5 function for an incidence angle of 35° (Yang et al., 2011).

The CMOD-IFR2 function is used in this study, and is given by Quilfen et al. (1998) as

$$\sigma_0 = 10^{\alpha+\beta\sqrt{V}} \times (1 + b_1 cos\Phi + \tanh b_2 \times \cos 2\Phi), \tag{2.41}$$

where σ_0 is the normalized radar cross section, V is the wind speed, ϕ is the wind direction and θ is the incidence angle of the radar. The b_1 and b_2 terms describe the upwind-downwind and upwind-crosswind amplitudes. The details of these variables are outlined in the appendix, in table A.1, with further details in Quilfen et al. (1998). This equation is solved for each point by maximum likelihood estimation, using the maximum likelihood estimator described by Quilfen and Bentamy (1994) as

$$MLE = \sum_{i=1}^{3} \frac{(\sigma_i - \sigma_{mi})^2}{(Kp \times \sigma_{mi})^2}, \tag{2.42}$$

where Kp is the radiometric resolution, σ_i is the NRCS for the beam (with the i indicating multiple beams in the case of scatterometers), and σ_{mi} is the model value for the beam. Since the CMOD functions were developed for VV-polarization, it's necessary to multiply the result from the function with a polarization ratio to get the correct result when using a HH polarized signal. Thompson et al. (1998) gives this polarization ratio as

$$PR(\theta) = \frac{\left(1 + \alpha \tan^2(\theta)\right)^2}{\left(1 + 2\tan^2(\theta)\right)^2}. \tag{2.43}$$

The α is a parameter chosen empirically, and set to 0.6 in this study, as suggested in Mouche et al. (2004).

Wind direction retrieval

As mentioned, the CMOD functions require wind directional input. In the case of scatterometers, the complete wind vectors can be calculated based on multiple observations from different angles provided by the use of multiple antenna beams. For SARs however, there is only one antenna, and the wind direction must be provided to the CMOD function from other sources. Several options exist, such as using wind directions from numerical weather prediction (NWP) models, sometimes in conjunction with in-situ data. The challenge with using NWP data is that there can be erroneous features in the prediction, such as weather fronts, which can easily be misplaced temporally or spatially. This is partially due to complications is modelling these features, and partially due to the resolution of most models, which may not be able to capture the features accurately in a resolution corresponding to the desired SAR image (Young et al., 2007). The use of low-resolution models often result in the application of one general wind direction for the entire SAR image, or interpolation of the modelled data. This leaves a potential for error both from lack of spatial and temporal correlation (Koch, 2004). The erroneous features in the model can be adjusted manually or semi-automatically with different available tools, to align more accurately with features seen in the SAR image, but many of the challenges connected to resolution and accuracy still remain.

Different methods exist to determine wind direction directly from the SAR image. Features in the image which can be used for this purpose include Langmuir cells, surfactant streaks, boundary layer rolls, and wind shadowing. For areas in the open ocean and larger areas, spectral methods can be applied. The gradient of an image with wind streaks can be used to determine the wind direction, as the gradient will point in the direction of greatest change. This direction will be roughly orthogonal to the wind direction. Gonzalez and Woods (2008) defines the gradient as the vector

$$\nabla f = \begin{bmatrix} \frac{\partial f}{\partial x} \\ \frac{\partial f}{\partial y} \end{bmatrix}. \tag{2.44}$$

The magnitude of the gradient is a measure of the rate of change of the gradient. Different discrete approximations can be applied as a filter mask, such as the Laplacian or Sobel operators. Koch (2004) suggests an

optimization of the Sobel,

$$D_x = \frac{1}{32}\begin{pmatrix} 3 & 0 & -3 \\ 10 & 0 & -10 \\ 3 & 0 & -3 \end{pmatrix}, \tag{2.45}$$

with D_y given by the transpose D_x^T. This operation is performed on the amplitude image, which will result in 180° ambiguities in the wind direction. Data points belonging to either land or non-wind features are discarded by the use of a coastline database and algorithms developed for removing such features. The method has an error of about 1°, but 180° ambiguities must be removed manually. (Koch, 2004)

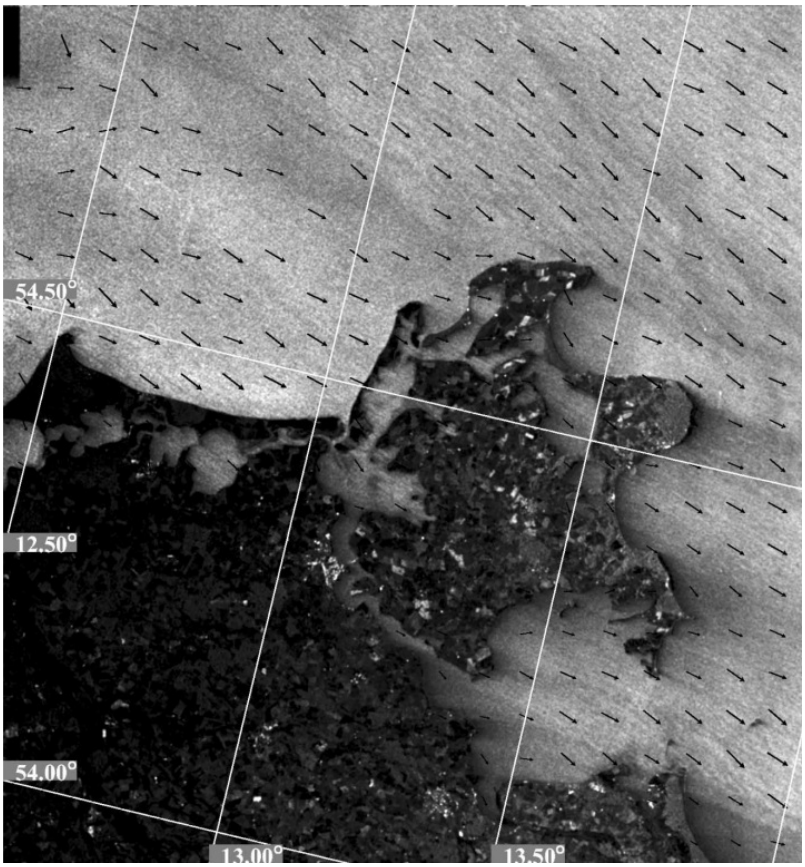

Figure 2.14: Wind streaks and matching wind gradients in a SAR image of Rügen taken on 12 August 1991 (Koch, 2004).

2.3 Numerical weather prediction

NWP systems aim to predict the future state of the atmosphere, and thus provide us with weather forecasts. However, the applications of a NWP-system extend to a number of areas which depend on knowledge of the atmosphere, such as air quality predictions and climate models.

NWP systems take their input from observations from around the world, in the form of atmospheric pressure, temperature, humidity, wind speeds and directions, etc.. These are taken from a number of sources, such as meteorological stations, buoys, ships, aircrafts and satellites. Observations are received and collected in databases, and this is coordinated by the World Meteorological Organisation (WMO). They are subjected to quality control which corrects for systematic biases, checks for consistency with nearby measurements and short-term forecasts, and removes data with serious errors caused by such things as faulty instruments. (Swinbank, 2010)

This data must be assimilated before it is input onto a NWP model. A common method used is based on Optimal Interpolation (OI) - the use of statistical interpolation techniques. Solving these equations is done with variational methods; a cost function J is constructed to find the optimal solution, where the difference between the model's state and the background (a-priori model) state as well as prior observations is minimized. Four-dimensional variational data assimilation (4D-Var) also accounts for the different acquisition time of the different data, and Swinbank (2010) gives the cost function as

$$J = \frac{1}{2}\left[\mathbf{x}_0 - \mathbf{x}_0\right]^T \mathbf{B}_0^{-1}\left[\mathbf{x}_0 - \mathbf{x}_0\right] + \frac{1}{2}\sum_{i=0}^{N}\left[\mathbf{y}_i - \mathcal{H}(\mathbf{x}_i)\right]^T \mathbf{R}^{-1}\left[\mathbf{y}_i - \mathcal{H}(\mathbf{x}_i)\right] \tag{2.46}$$

, where $\mathbf{x}$ is the vector that defines the model state, $\mathbf{x^b}$ is the background model estimate, $\mathbf{y}$ is the observations, $\mathbf{R}$ is the error covariance of the observations and $\mathbf{B}$ is the error covariance of the background estimate.

The core of a NWP system are the so called *primitive equations* - equations based on the equation laws of momentum, mass, energy and moisture, and which describe the basic processes in the atmosphere. These equations must be solved numerically, thus approximation errors in the model will exist. (COMET Program, 2013, "Impact of Model Structure and Dynamics")

The primitive equations are usually evaluated at regular points in a latitude-longitude grid. Models covering a larger area, with lower resolution, are generally more accurate than mesoscale, or high-resolution local-area models. They require more time and processing power, though, as it requires the primitive equations to be evaluated at more grid points and with more time-steps. (Swinbank, 2010)

A model is not able to resolve physical processes which occur on a smaller scale then the grid scale, and in fact can only resolve processes on a scale a few times larger than the grid resolution with any degree of accuracy. Such things as precipitation, small cumulus clouds, surface friction, aerosols and small-scale turbulence are processes on a smaller scale than the model can "see". Yet they can be essential for the atmospheric processes, particularly on a mesoscale level. NWP systems solve this by *parametrization*. These physical processes are included in the model as parametrized versions of themselves based on physical or statistical simplifications and assumptions. (COMET Program, 2013, Model fundamentals)

Mesoscale models can use locally available observations as initialization data, and provide a better short-term forecast. Alternatively one can run small-scale models nested inside larger-scale model and use the larger model as boundary conditions, alone or in combination with initialization data from measurements. (Swinbank, 2010)

2.3.1 The Unified Model

The Unified Model(UM) is developed by the United Kingdom national weather service, Met Office. It incorporates several different model components (such as ocean and atmosphere) with different configurations for the time and spatial scales. This improves efficiency and the level of complexity, and is thus termed a *seamless* model by the Met Office (Met Office, 2013). It is used all over the world, in different versions with grid sizes ranging from 60 km to only 1.4 km.

The primitive equations used by the UM for the wind motion is given by Davies et al. (2005) as

$$\frac{Du}{Dt} - f_r v + f_\phi w - \frac{uv\tan\phi}{r} + \frac{uw}{r} + \frac{c_p\theta_V}{r\cos\phi}\frac{\partial\Pi}{\partial\lambda} = P^u \tag{2.47}$$

$$\frac{Dv}{Dt} - f_r u + f_\lambda w - \frac{u^2\tan\phi}{r} + \frac{vw}{r} + \frac{c_p\theta_V}{r}\frac{\partial\Pi}{\partial\phi} = P^v, \tag{2.48}$$

$$\frac{Dw}{Dt} - f_\phi u + f_\lambda v - \frac{\left(u^2+v^2\right)}{r} + g + c_p\theta_V\frac{\partial\Pi}{\partial r} = P^w \tag{2.49}$$

where (u,v, w) are the wind components, (λ,ϕ,r) (longitude, latitude, radius) are the spherical polar coordinates with origin at the Earth's centre, and P are the tendencies from the physical parametrizations. Π is the Exner pressure defined as $\Pi = \left(\frac{\rho}{\rho_0}\right)^\kappa$, where ρ is the pressure, ρ_0 is a reference pressure and $\kappa \equiv \frac{R_{dry}}{c_p}$. R_{dry} is the dry air gas constant and c_p is the corresponding specific heat.

The method used for discretizing the equations is a semi-Lagrangian scheme. The equations are still evaluated in a regular grid, as it would for a Eulerian method. As opposed to for a fully Lagrangian method, where the movement of the air parcels would be traced along their entire trajectories, a semi-Lagrangian scheme only keeps track of the grid point the parcel arrived from at the present time step, and integrates the surrounding grid values. (Kalnay, 2003)

UM is a non-hydrostatic model, meaning that it solves the primitive equations for vertical movement as well as horizontal. Hydrostatic models, such as older NWP models, simplified the vertical movement in the atmosphere by assuming a balance between the pressure gradient and the atmosphere weight. Using a non-hydrostatic model improves the ability to resolve physical processes in high-resolution models. (COMET Program, 2013, Impact of Model Structure and Dynamics)

Chapter 3

Data and methods

This chapter will present the data used in this study as well as any pre-processing and filtering done to prepare it for analysis. An illustration of the work flow can be seen in fig. 3.1, and each step will be described in further detail under the corresponding sections.

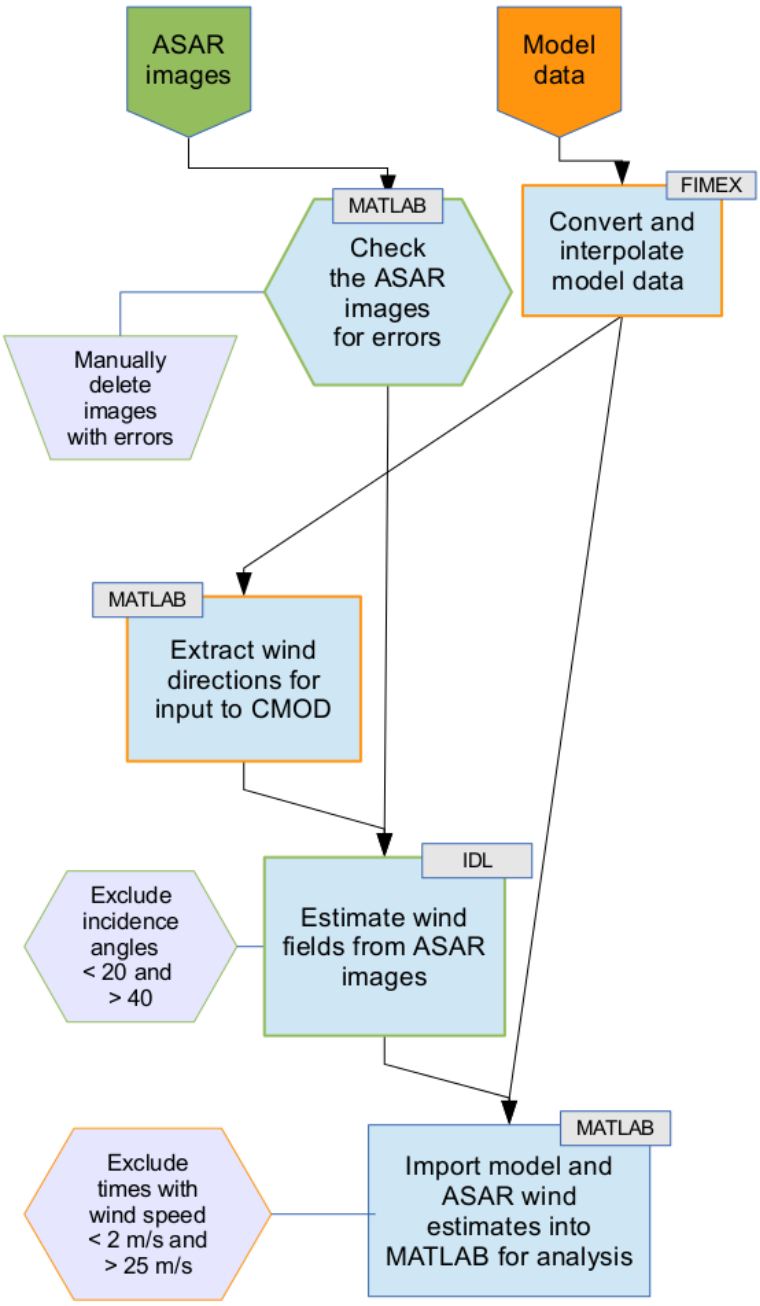

Figure 3.1: Flow chart showing the workflow in this study, from unprocessed ASAR/model data to analysis.

3.1 Area and time frame

The Vannøya area is a good illustration of many of the possibilities and challenges relevant to wind estimation with SAR for offshore wind power production. It has been identified by the NVE as an area which is potentially suited for offshore wind production (Norwegian Coastal Administration, 2013), and has since July 2nd 2012 been the site of an onshore wind park owned by Troms Kraft AS. The wind park consists of 18 turbines with an estimated 138 GWh production, and a second site (Fakken II) just to the north is under planning. In addition, an offshore wind farm just east of Fakken I is in the early stage of planning, and estimated size is around 250 turbines with around 2.5 TWh total production (Troms Kraft, 2013). Coastal areas in Norway are generally quite deep, and the current technological limitations related to site depth means that wind farms will often have to be placed closer to the coast than elsewhere.

Geographically, the area is a good example of typical Norwegian coastal geography, with a combination of mountainous terrain, islands and fjords. No part of the selection is very far from the coast, with the furthest offshore point being 23 km from the tip of Vannøya. In short, it makes for a complicated wind climate, and the corresponding challenges in wind estimation in conjunction with the area's high wind potential makes it an interesting subject for this study.

Figure 3.2: Map showing the location of the area.

UTM, zone 33W	65660E	710680E
	7828400N	7768400N
Latitude / longitude	70.5118, 19.2088	70.4277, 20.6545
	69.9752, 19.1004	69.9368, 20.5092

Table 3.1: Coordinates for the area

3.1.1 Time span of data

The selected time span is mainly based on the availability of ASAR scenes. A whole year is necessary to be be able to get some idea of seasonal variability, as well as a high enough number of scenes. As the Envisat mission officially ended on 9 May 2012, scenes have been chosen which cover 2011 (1 January 2011 - 31 December 2011) and 1 January 2012 - 31 April 2012. An overview of the distribution of data points by month and year can be seen in figure 3.3.

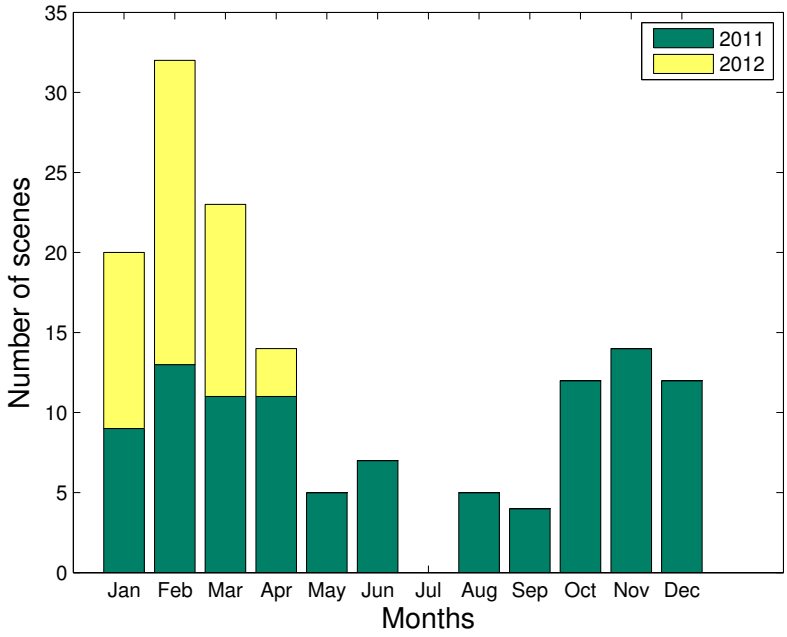

Figure 3.3: Illustration of the monthly distribution of data points.

3.2 Data

3.2.1 ASAR data

Initially, a total of 261 ASAR scenes taken by the Envisat satellite between 1 January 2011 - 31 April 2012 were acquired. These images were generously supplied by the Northern Research Institute (NORUT), and were already pre-processed in terms of standard geographical and radiometric corrections. Selections covering the area shown in figure 3.2 were made from the images. An example ASAR selection of the area can be seen in figure 3.4. The images have a spatial resolution of 75 m, which means that each image pixel covers 75 meters on the ground, and the total selections covers a 60 km $\times$ 54 km area.

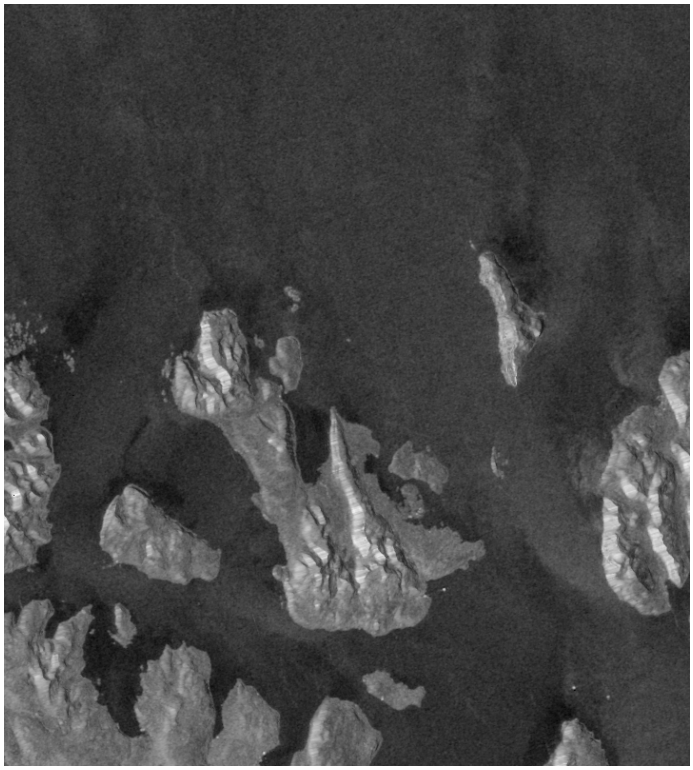

Figure 3.4: ASAR image of Vannøya, taken 15 January 2011.

Wind fields were estimated from the images with the use of an algorithm in IDL which employs the CMOD-IFR2 algorithm detailed in section 2.2.4. The IDL algorithm provided by NORUT averages the image pixels based on the desired wind cell resolution chosen by the user. The averaging is done to reduce statistical noise, and it's common to average the SAR image to 300 m - 600 m resolution (6 - 10 times original pixel size) (Monaldo et al., 2001; Barthelmie and Pryor, 2003). In this case, pixels were averaged to give wind fields with a 450 m resolution, with the aim of keeping as much detail as possible.

The algorithm creates a wind field image by passing information about polarization, ascending/descending pass, incidence angle and wind direction from the wind model data, to the CMOD-IFR2 algorithm, and applies a land mask.

Image coordinates

The geotiff image contains the geographical location of each image pixel given in Universal Transverse Mercator (UTM) coordinates. The UTM grid is divided into 60 zones of 6° longitude each. They are generally uniform, except in some few instances. On the UTM meridians separating the zones, the scale factor of the projection is exactly 1, while vertically dividing each zone is a central meridian with a scale factor of 0.9996 (Snyder, 1987). As the northing and easting coordinates of a grid is given in meters from the point of intersection between the equator and the zone's central meridian, it is perfectly possible to give a location in a different set of grid coordinates than the one it is located in. Because the larger part

of the original satellite images cover UTM zone 33W, the area selected was automatically geolocated in these coordinates, despite the selection being entirely in UTM zone 34W. Due to the change in scale factor described above, this leads to a slight error in the location of the image pixels. However, this error is only at the most 10% at the far boundary of zone 34W. For the area used, the error along the 70th parallel will be $0.045\% - 7.4\%$ (distortions increasing towards the east), i. e. between 0.45 - 74 m/km. Considering the resolution of 450 m, this is not a considerable amount. Another reason for keeping the original coordinates is that the selection in the 33W grid is regular, while the corresponding selection in the 34W grid is slightly rotated in relation to the grid lines. This would complicate the interpolation of the model data, which is described in section 3.2.2.

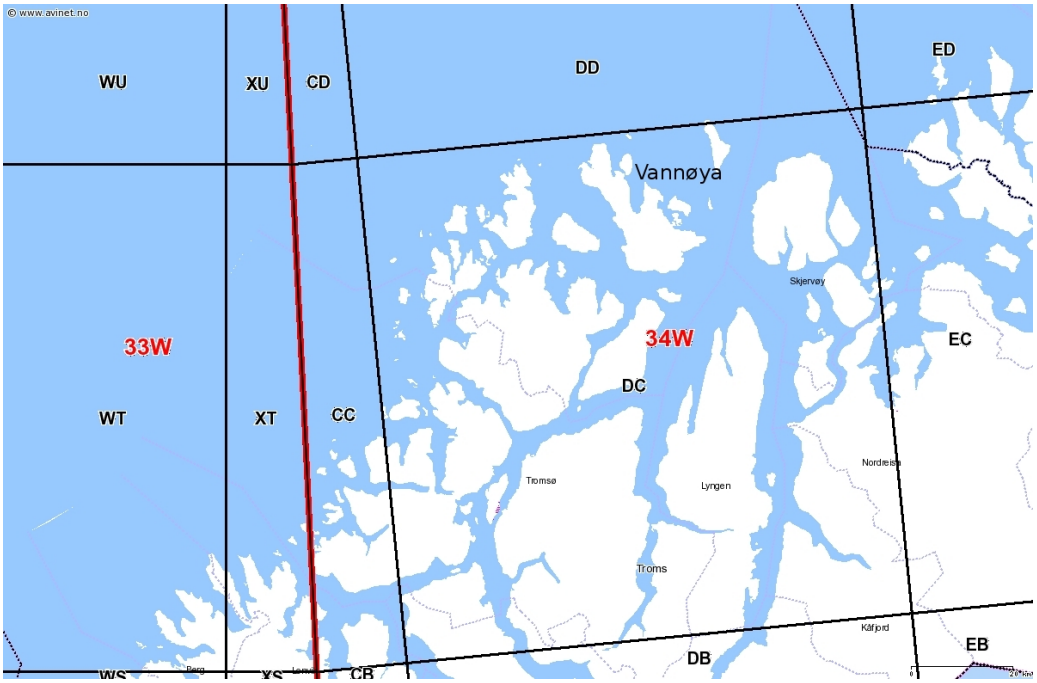

Figure 3.5: UTM and MGRS zones.

Filtering of data

ASAR scenes have been filtered based on a number of criteria. A first selection of ASAR scenes has been done by removing images which contained missing data. From the original 261 geotiff-files, 36 were removed, all of which were quite evenly distributed over the time period. ASAR scenes captured with an incidence angle $< 20^\circ$ and $> 40^\circ$ have been filtered. For incidence angles $< 20^\circ$, specular scattering dominates over Bragg scattering (Kudryavtsev et al., 2003; Romeiser and Alpers, 1997; Romeiser et al., 1997), and NRCS calibration errors have a larger impact (Yang et al., 2011). For incidence angles over 40°, a large part of the signal is scattered away from the sensor, making the noise/signal ratio higher.

Scenes have been limited to include only those those with a wind speed of ≥ 2 m/s and ≤ 25 m/s. This is done to avoid an artificial bias caused by the CMOD-IFR2 algorithms low validity for wind speeds outside this range (Beaucage et al., 2007). Due to the complicated coastal terrain, it is to be expected that some areas

will be in lee of the wind a lot of the time. It's not feasible to remove *all* scenes with wind speeds < 2 m/s, as this would include most of them. Therefore, only scenes where over 85% of the model and ASAR ocean wind cells have wind speed ≥ 2 m/s have been included. Only one scene had frequent wind speeds of over 25 m/s, however an additional 12 scenes had a small number of pixels with unusually large wind speed values, frequently over 40 m/s. These pixels were mainly located close to the coast, with some further offshore, and it's reasonable to assume that these are caused by man-made objects such as ships. These will scatter a very large portion of the signal back to the sensor, and thus have a much larger NRCS value than the surrounding ocean. Replacing the offending pixel with the image mean value will still provide an unnaturally high value, especially in images with otherwise low wind speeds. As a majority of the ocean image pixels are found in the relatively homogeneous northern part, this area (as will be shown in section 4.2) proved to have similar statistical properties as the overall area. It was therefore decided to use the mean of a 9x9 pixel selection centred around a point in the north-western area in place of the very high pixel values. Naturally this is not a perfect solution, as certain wind conditions would cause this area to have higher wind speeds than the replaced pixel would normally have, but considering the low number of offending pixels in each of these 12 images, it is not likely to have any noticeable influence on the statistics.

Some scenes are acquired within a very short time period of each other, of under 10 min. Considering there is generally a minimum time difference of 12 hours between the scenes, these have been considered duplicate data and one half removed. This leaves a total of 148 scenes for analysis, of which 103 are from 2011.

Heavy rain can affect the wind estimates due to scattering in the atmosphere, as well as by dampening the Bragg scattering on the ocean surface or otherwise modifying the capillary waves that indicate wind speed. (Hasager et al., 2011; Liu and Xie, 2006) Therefore, it's not unusual to filter out images which are affected by rain, to get a better estimate of the wind. However, the model data available only gives information on total accumulated precipitation amount since model initiation time, which is a minimum of 36 hours from the ASAR image was captured. Any attempt to get an idea of the precipitation at the time the image was captured would result in an estimate so uncertain as to render it useless for filtering. The scenes have therefore not been filtered for rain.

3.2.2 Model data

Wind model data has been acquired from the Meteorological Institute (MET). The model used is the 4 km Unified Model (abbreviated UM4) described in section 2.3.1.

Re-projection and extraction of data

The meteorological model data was provided in the felt-format developed by MET, and had to be converted to NetCDF before being imported to Matlab. Originally, the model data was also in a rotated latitude/longitude grid covering all of Norway. Using MET's open source File Interpolation, Manipulation and EXtraction (FIMEX) library, the data was re-projected to the same UTM map projection as the ASAR scenes. The desired section was extracted, and the data was interpolated using bilinear interpolation to get a grid size of 450 m, with data points geographically matching the ASAR wind estimates.

The model provides 10 m wind estimates on vector form, with the vectors aligned in relation to the model grid. As the model is re-projected to the appropriate UTM grid, the wind vectors are also rotated so as to be given in relation to true north. The potential mathematical error in this rotation was given by MET as 5°. From these wind vectors, the meteorological wind direction must be derived and be input to the CMOD-IFR2 algorithm to be used when estimating the ASAR wind fields. For this reason, a version of the

meteorological data is created which is interpolated to match the original ASAR resolution of 75 m$\times$75 m. This is only used as wind directional input to the CMOD algorithm.

Temporal interpolation

The UM4 model is run nested inside a 12 km High Resolution Local Area Model (HIRLAM). When the UM4 is run nested like this, it's not initialized with assimilated data, but rather the boundary conditions are taken from the HIRLAM model. Due to the difference in resolution between the two models, the dynamics of the HIRLAM model take some time to stabilize in the UM4 model. The time this takes is referred to as "spin-up time", and it is usually 6 - 12 hours (COMET Program, 2013, from "Effective use of high-resolution models"). To ensure that no errors are caused due to this spin-up time, the data is taken 24 - 48 hours from the model's initialization time. As the model data is given for each full hour from the initialization point, the data has also been time interpolated to exactly match the ASAR data. As the model data also includes estimates for land, the same land mask which was applied to the ASAR scenes, was also applied to the model data.

3.2.3 In situ measurements

The in-situ wind measurements are 10 meter wind observations from the Fakken wind farm, curtsey of the owners, Troms Kraft AS. Though wind data for a larger time span is available from Torsvåg Fyr on the northern part of Vannøya, these are not considered representative observations by MET, and have not been used. The measurements are averages of the last 10 minutes before the given observation time. As many data points as possible have been included for 2011, with automatic filtering done by met.no to exclude data of low quality. The remaining data consists of wind speeds and corresponding wind directions for 8273 times, with between 629 and 713 data points for each month through the year. The location of Fakken is illustrated in fig. 3.6.

3.3 Case study of data set

3.3.1 Individual locations

Certain locations in the area have been chosen for a more detailed investigation as they may give further insight into the wind climate. The locations are illustrated in fig. 3.6, with coordinates listed in table 3.2. Since we expect this coastal region to have a complex wind climate, locations have been chosen which might shed some light on the different wind conditions for different wind direction and speeds. These include locations further from the coast, such as 1 and 4, and locations near the fjord mouths, such as 5 and 6. This will let us see in more detail how the ASAR and model estimates differ in various situations.

	1	2	3	4	5	6	Fakken
UTM, (33W)	665600E 7828400N	674600E 7819400N	683600E 7810400N	692600E 7801400N	701600E 7792400N	710600E 7783400N	693686E 7785613
LATITUDE,	70.50610	70.41957	70.33277	70.24570	70.15836	70.20374	70.1042
LONGITUDE	19.44985	19.67215	19.89258	20.11114	20.32787	20.57858	20.1048

Table 3.2: Coordinates for the locations in figure 3.6.

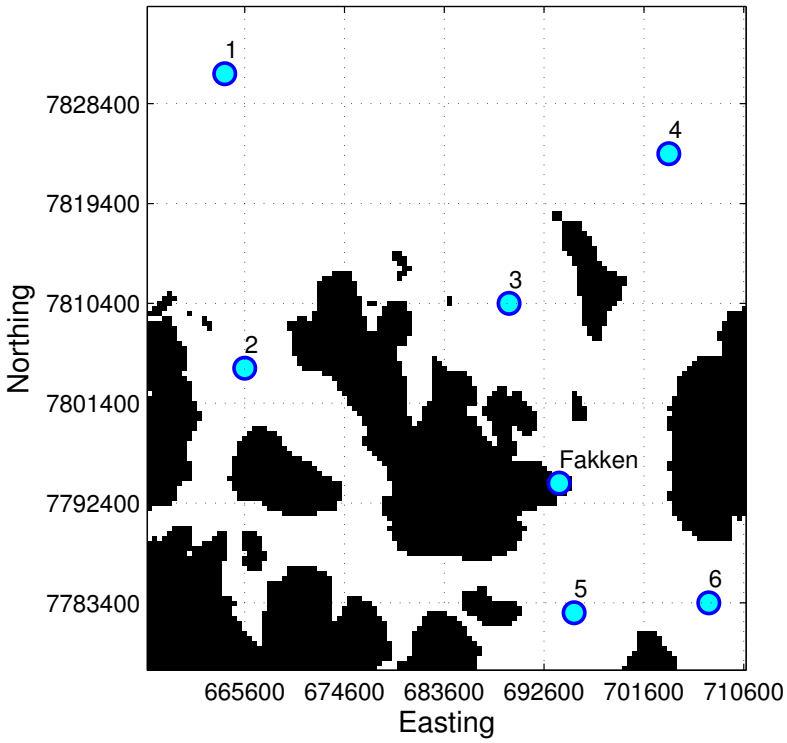

Figure 3.6: Selected locations.

3.3.2 Selected scenes

As mentioned earlier, one of the reasons why wind estimation with ASAR is an attractive option, is because the resolution potentially enables us to identify details in the wind climate in the scene which might not be apparent from model wind estimates. Therefore, it is natural to also do a qualitative analysis of the ASAR and model data. Weather fronts and other details might be shifted spatially or temporally between the model and ASAR data, and this will not be apparent from a purely numerical analysis. Therefore, a combination of qualitative and quantitative analysis can be of great benefit (Dagestad et al., 2006).

A selection of ASAR scenes has been made for this purpose. The scenes have been chosen based on a combination of high and low wind speeds and different wind directions, as well as a purely subjective evaluation of what might be interesting features in the ASAR images. Some scenes have also been chosen because the wind speed discrepancy in one of the locations described in section 3.3.1 is particularly large for this date, and it's interesting to investigate the cause of this. This is described in more detail in section 4.2.

3.4 Methodology

The following section will present the statistical methods used when investigating the data that has been presented. The aim of the study can be summarized, very simplified, as a comparison of wind model estimates and ASAR estimates. But as an essential part of the underlying problem is the general lack of ground truth for situations like these, it stands to reason that a large factor in this comparison must be the qualitative evaluation of the estimates. With this in mind, the main focus will be on descriptive statistics, as they will complement the qualitative analysis best.

3.4.1 Estimators

The following is a brief presentation of the estimators used in the study. As they are fairly standard statistical estimators, they will not be expound on in any detail.

Mean

The sample mean, or arithmetic mean, is given by Walpole et al. (2007) as

$$\bar{x} = \frac{1}{n}\sum_{i=1}^{n} x_i, \tag{3.1}$$

where n is the number of elements in the sample. We will assume that the sample mean is a good estimator of the population mean, so that $E(\bar{x}) = \mu$.

Standard deviation and variance

The sample variance, σ^2, is an measure of the variability of a sample, and is given by (Walpole et al., 2007) as

$$s^2 = \frac{1}{n-1}\sum_{i=1}^{n} (x_i - \bar{x})^2 . \tag{3.2}$$

The standard deviation, σ, is merely the square root of the variance, and gives the variation or deviation in relation to the mean.

3.4.2 Bias

The bias is used to describe how the wind speed estimates are underestimated or overestimated in relation to each other. The bias of an estimator is defined as

$$Bias\left(\hat{\theta}\right) = E\left[\hat{\theta}\right] - \theta. \tag{3.3}$$

As used in this study, the bias only describes the relationship between the estimates themselves, and not the true wind speed. If we assume as mentioned earlier that each sample mean is a good estimator of the true mean, we can get an expression of the bias between the samples as

$$Bias = \frac{1}{n}\sum_{i=1}^{n}(x_{i,ASAR} - x_{i,MODEL}). \tag{3.4}$$

3.4.3 Correlation coefficient

The covariance of two random variables X and Y describes the nature of a variables dependance on the other, and how a change in one will affect the other. An example is when an increase in one variable results in an increase in the other. The covariance is defined by Walpole et al. (2007) as

$$\sigma_{XY} = E(XY) - \mu_X\mu_Y. \tag{3.5}$$

However, the magnitude of the covariance is not a measure of *how much* a change in one variable affect another. Therefore we will use the correlation coefficient, which is normalized to [-1,1], and will also tell us something about the strength of the relationship between the variables. The correlation coefficient is given as

$$\rho_{XY} = \frac{\sigma_{XY}}{\sigma_X\sigma_Y}. \tag{3.6}$$

3.4.4 Root mean square difference

The mean square error (MSE) is simply put an estimate of the difference between two samples, where the squared error is averaged over the sample. Devore and Berk (2007) defines the MSE as

$$MSE = E[(\hat{\theta} - \theta)^2] \tag{3.7}$$

Taking the root of the MSE gives us a measure of the error between the estimates on the same scale as the data, which makes it more intuitive and easily comparable. However, it can be sensitive to outliers, which is something to be aware of (Hyndman and Koehler, 2006). As we will not generally be comparing the estimates with the true wind, an equivalent of the rms error will be used to express the root mean square difference (RMSD) instead.

$$RMSD = \sqrt{\frac{1}{n}\sum_{i=1}^{n}(x_{i,ASAR} - x_{i,MODEL})^2} \tag{3.8}$$

3.4.5 Probability density function

The Weibull probability distribution which is used to describe the wind speed distribution was described in detail in section 2.1.1, and it will not be repeated here. The Weibull pdf will be estimated in this study for model and ASAR wind estimates, as well as using the in-situ observations. The maximum likelihood method was used to estimate the parameters of the distribution for the 103 scenes of 2011, as well as for the individual locations outlined in section 3.3.1.

The estimated probability density function will also be used to estimate the available power density of the wind, which is defined in eq. (2.18). We assume the density of the air is $\rho = 1.225$.

Dataset density

A method of estimating the Weibull distribution as been presented, but as the number of available SAR-scenes for any given site will probably be limited, it's interesting to establish how large a data set is necessary to be able to accurately estimate the distribution parameters. Barthelmie and Pryor (2003) looked at in-situ measurements for the Vindeby offshore wind farm and re-sampled them to emulate a reasonable SAR dataset density. They concluded that over 60 randomly selected images were needed to estimate the Weibull scale parameter, over 150 for the variance and over 2000 to estimate the energy density. This should give an uncertainty of $\pm 10\%$ and a 90% confidence level. These figures were analytically verified to a large degree in (Pryor et al., 2004).

Regardless of the method used for measuring and predicting the wind climate, some degree of error is unavoidable simply due to the changeable nature of the local wind and the scale of the variability. Barthelmie et al. (2009) estimates these uncertainties to $\pm 5\%$ for estimates based on 30 years of data, and $\pm 15\%$ for one year of data.

3.4.6 Circular statistics

When comparing wind directions, we encounter the problem that wind direction is not a linear variable but an angular one, and the discontinuity at 360° makes calculating certain statistics less straight forward than we're used to. As an illustration, we have that a difference between two angles of 300° will in reality be smaller than one of 180°. Also, when averaging wind directions, it's intuitively obvious to us that the average of the wind directions 355° and 5° is not in reality 180°, but 0°.We therefore can't assume that the statistical definitions we're accustomed to when dealing with linear data will hold hold in the case of circular and angular data. As the in-situ wind direction observations are given in degrees and not as wind vectors, it's necessary to use circular statistics.

Rose diagrams

Rose diagrams, or wind roses as they are referred to in this context, are merely circular representations of a histogram of the wind directions. The wind rose bins are 30°, and the radial axis indicate the frequency of a given bin. The wind roses in this report are not normalized, i.e. the total area of the bars do not equal one, bit rather their length indicates the frequency. The color segmentation of the bars show the relative frequency of different wind speeds for each wind direction bin.

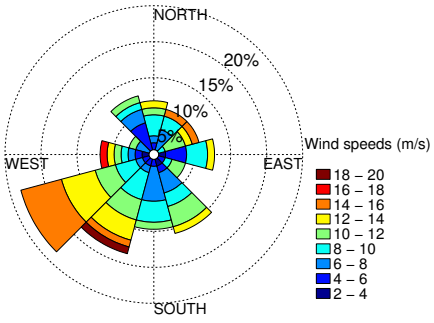

Figure 3.7: Example wind rose

Mean

Berens (2009) The mean wind direction can be calculated by converting the angle to its vector components and summing them, as described in Jammalamadaka and Sengupta (2001).

$$\mathbf{R} = \left(\sum_{i=1}^{n} \cos\alpha_i, \sum_{i=1}^{n} \sin\alpha_i \right) = (C, S) \tag{3.9}$$

The direction of the resultant vector is the mean direction we are looking for, which can be recovered with the tangent function like so to get the quadrant specific angle:

$$\overline{\alpha}_0 = \arctan\left(\frac{S}{C}\right) = \begin{cases} \arctan\left(\frac{S}{C}\right), & \text{for} \quad C > 0, \quad S \geq 0 \\ \frac{\pi}{2}, & \text{for} \quad C = 0, \quad S > 0 \\ \arctan\left(\frac{S}{C}\right) + \pi, & \text{for} \quad C < 0 \\ \arctan\left(\frac{S}{C}\right) + 2\pi, & \text{for} \quad C \geq 0, \quad S < 0 \\ \text{undefined}, & \text{for} \quad C = 0, \quad S = 0 \end{cases} \tag{3.10}$$

Angular deviation

The length of the resultant vector derived in section 3.4.6 is given as $R = ||\mathbf{R}||$. This is a measure of the concentration of the data, i.e. a large R indicates that the data is closely centred around the mean, while R = 0 means that the data is too widely dispersed for a mean to be calculated. It can indicate a uniform distribution, but this isn't always the case, and can't be assumed. $1 - R$ then becomes a measure of the dispersion of the data, and Zar et al. (1999) gives a definition of the angular variance as

$$s^2 = 2(1 - R). \tag{3.11}$$

From this we find that the angular deviation, the equivalent of the linear standard deviation, is

$$s = \sqrt{2(1 - R)}. \tag{3.12}$$

3.4.7 In-situ and model comparison

Naturally, in-situ wind speeds acquired from the onshore Fakken wind farm cannot be used to directly validate the offshore ASAR wind estimates. However, by comparing them to the model wind speed and direction, its possible to get a sense of the errors in the model estimates - particularly in regards to the wind direction, which directly affects the ASAR wind estimates.

3.4.8 Topographical and ocean effects

Several topographical features are likely to affect the wind in the region. As this is not a study in meteorology, the aim will not be to identify all of them, but merely to describe the effects where they might be apparent on the ASAR wind image and how it relates to the model estimates. Section 2.1.2 describes some of the effects which are likely to appear in an ASAR image depending on wind conditions.

The identification of the locations and scenes described in section 3.3 is important to this process as it allows for a more thorough visual and statistical comparison of the effects different wind conditions have on the ASAR and model wind estimates.

Chapter 4

Results

This chapter will present and describe the results based on the methods and data outlined in the past two chapters. Results related to an analysis of all 11999 ocean data points for all 103 scenes in 2011 will be presented in section 4.1. Results related so the selected locations, including Fakken, as outlined in section 3.3.1, are described in section 4.2. Potentially important factors such as seasonal and diurnal variations and wind speed dependencies, are described in section 4.3. The chosen ASAR scenes are described in section 4.4. Statistics for all the results examined in this chapter can be found in the appendix in table A.2, and will be summarized as relevant in the following sections, while statistics from the Fakken in-situ and model data can be found in table A.3.

Figure 4.1 shows the land mask used by the UM.4 model for this area. As we can see, the resolution is quite low, with the model merely indicating Vannøya and leaving out several of the other small islands in the area. This is not completely unexpected, considering the original resolution of the model is 4 km. The model height of Vannøya is show in the illustration for easier comparison.

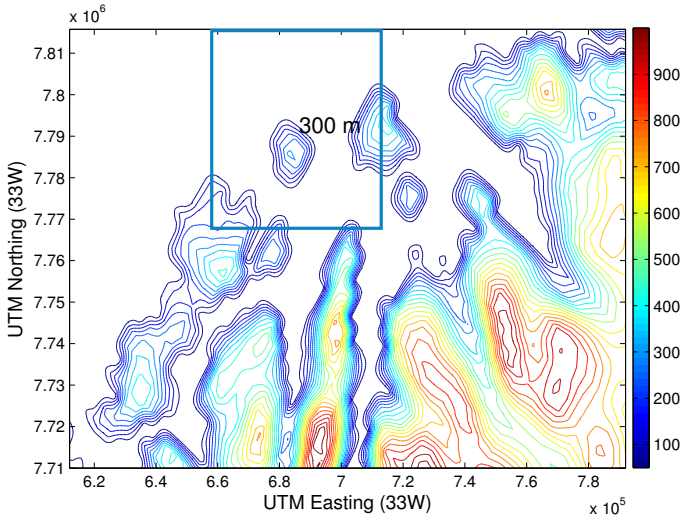

Figure 4.1: Model land mask

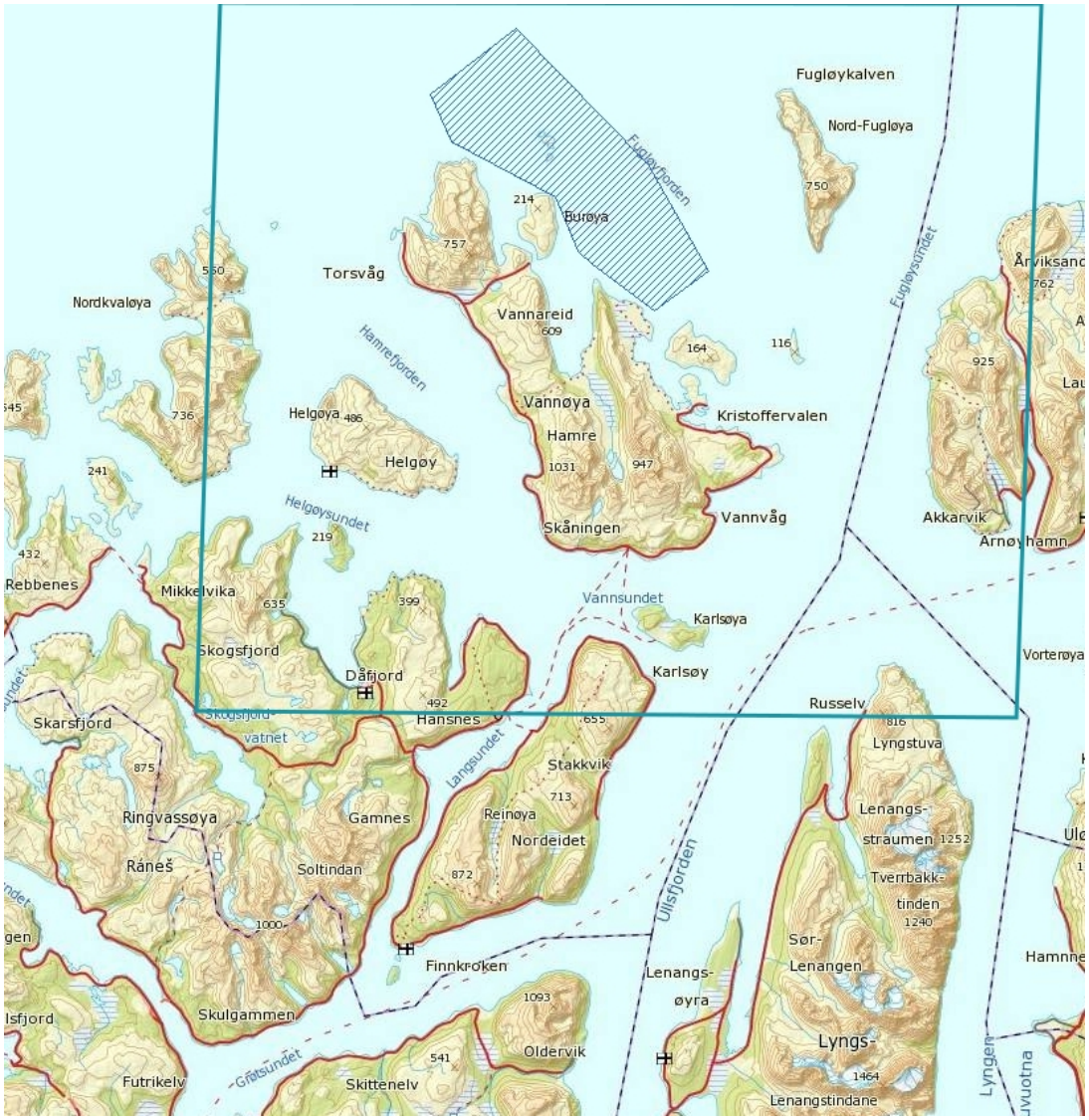

Figure 4.2: Map of Vannøya and surrounding area. Map from Norwegian Coastal Administration (2013).

Figure 4.2 shows a map of the region, with the turquoise selection illustrating the part of the area covered by the ASAR images. This map better shows the actual topography of the region, and is necessary to get a better idea of the terrain which affects the winds we see in the wind maps. Place names will be used for easier reference to geographical features. The shaded area on the north coast of Vannøya is the area designated by NVE as potentially suitable for an offshore wind farm, as mentioned in section 3.1.

4.1 Wind climate statistics

Figure 4.3a shows a wind rose illustrating the distribution of offshore wind directions for the entire area for all of 2011. The wind is grouped into 30° bins, and indicates the winds originating direction and frequency, as described in section 3.4.6. The normalized histogram in fig. 4.3b similarly illustrates the 2011 wind of the area organized into 30° bins. It's clear that south-west is the dominant wind direction. The directional mean of the wind is $\mu_{DIR} = 267.9°$, with standard deviation $\sigma = 78.6°$.

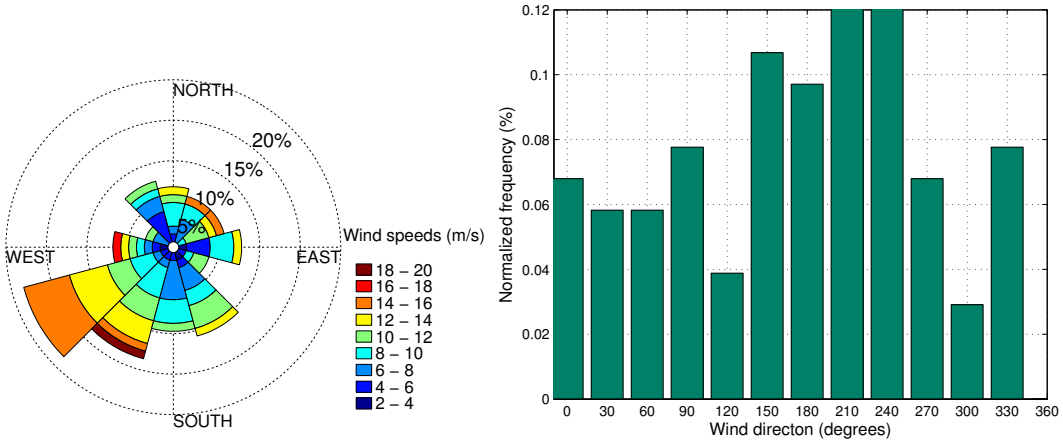

(a) Wind rose

(b) Entire area

Figure 4.3: Wind directions

The Weibull probability density functions in fig. 4.4 are estimated as described in section 2.1.1, and are both calculated based on 11999 offshore data points in 103 scenes. We can see the difference in mean wind speeds, 8.28 m/s for model wind estimates and 7.64 m/s for ASAR wind estimates. The slight positive skewness of the distributions are probably to some degree linked to the filtering away of most wind speeds under 2 m/s. The power plots in fig. 4.4c are histogram plots illustrating the theoretical power production based on model and ASAR wind estimates. They are both normalized in relation to the model power plot, to illustrate the discrepancy in power output depending on the two different wind distributions. They are based on the model and ASAR wind speed histograms, and not the probability density functions, which is why they are not as smooth. The small peak in power for the ASAR plot around 20 m/s is related to the small peak we can see in fig. 4.4a for the same wind speed. This is also apparent in the small cluster in the scatter plot in fig. 4.4d. The line going through the scatter plot is a least-squares fit of a regression line.

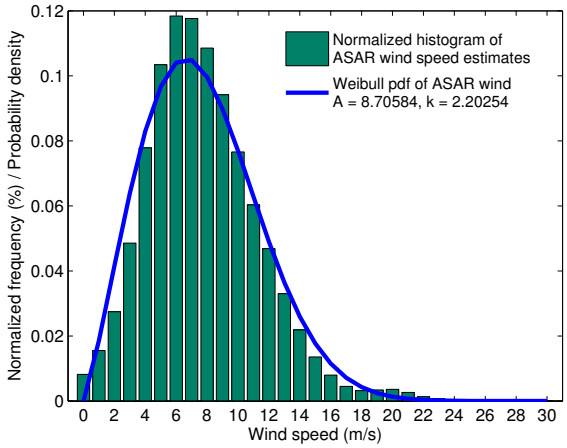

(a) Weibull pdf and histogram of ASAR wind speeds

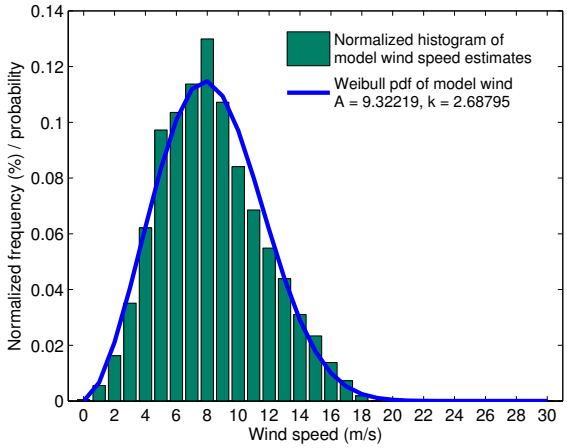

(b) Weibull pdf and histogram of model wind speeds

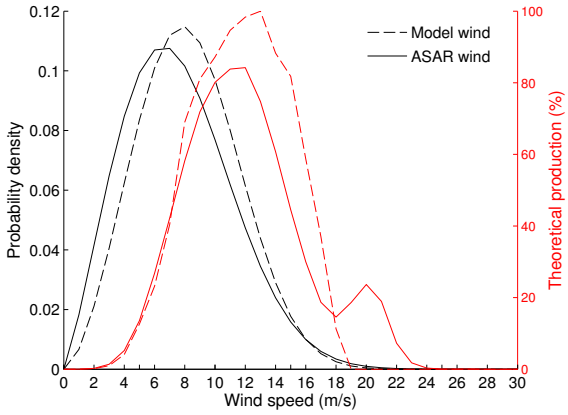

(c) Weibull probability density function of ASAR and model wind speeds.

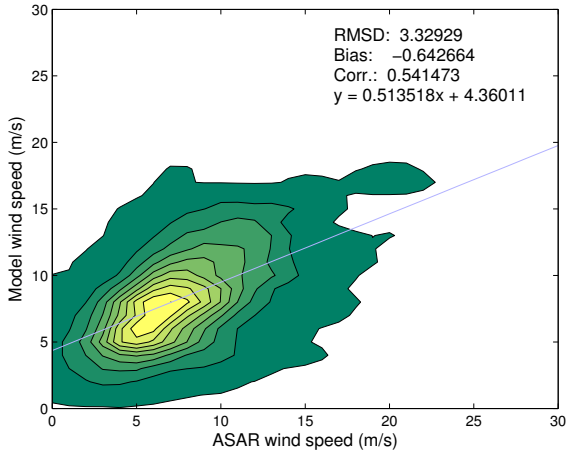

(d) Contour of scatter plot for all datapoints

Figure 4.4: Model and ASAR wind comparison plots

4.1.1 Polarization

To examine any possible error contribution from the different polarizations of the ASAR scenes, the data for 2011 was separated into groups of VV and HH polarization, and the scatter plots and wind statistics in fig. 4.5 was made. The RMSD and correlation coefficients are quite similar, although it must be noted that the data basis is much higher for HH-polarization. As we can see from fig. 4.5c, nearly all of the VV-polarized scenes were captured during June 2011.

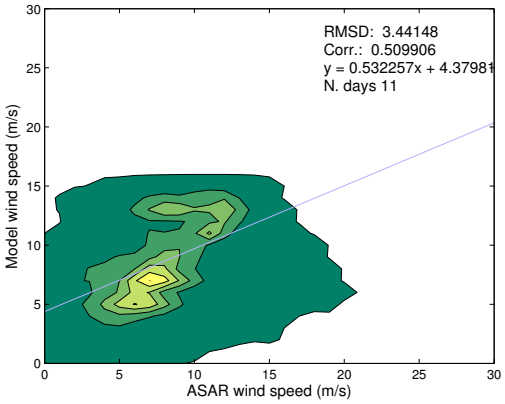

(a) Scatter plot for 'VV' polarizaton

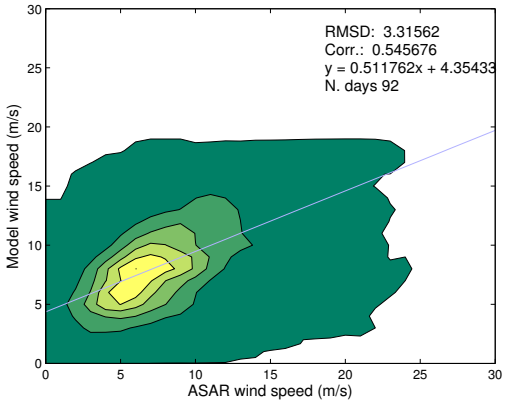

(b) Scatter plot for 'HH' polarizaton

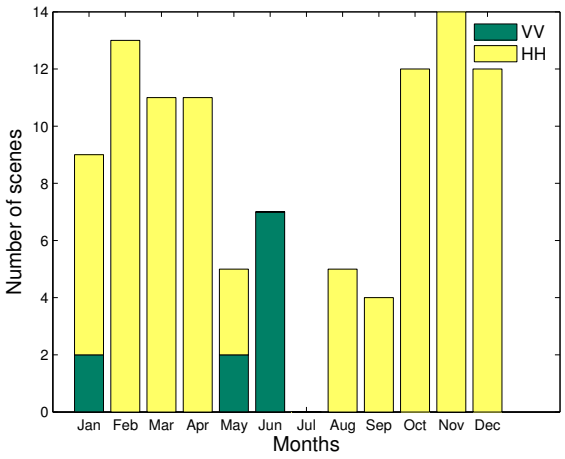

(c) Frequency of polarizations

Figure 4.5: Scatter plot and monthly distribution of polarizations

4.1.2 Errors in wind direction

Johannessen et al. (2003) concludes that for the CMOD4 algorithm, the largest error in wind speed is for wind direction with 45° error, while deviations in input wind directions as low as ±20° can cause errors

in wind estimates as high as 2 m/s. To get an idea of the variability in the ASAR wind estimates due to the inherent variability of the model wind directions, a simple test has been performed. The ASAR wind speed has been estimated for a fixed incidence angle of 30° and wind direction of 45°, for a common NRCS value in the data (0.1117). The wind speed is then estimated again, but with the standard deviation of the difference between the model wind and the in-situ measurements, 33.2°, added to the wind direction. The result for different polarizations are presented in table 4.1. Note that due to the non-linear relationship between incidence angle, NRCS, wind direction and wind speed, it can't be assumed that larger errors in wind direction will automatically cause similarly larger errors in wind speed.

Polarization	45°	78.2°	Difference
VV	10.07 m/s	14.21 m/s	4.14 m/s
HH	11.52 m/s	15.5 m/s	3.98 m/s

Table 4.1: Errors from model wind direction

4.2 Selected locations

The wind roses in figure 4.6 show the frequency of wind directions for each of the selected locations outlined in fig. 3.6. locations 1 and 4 are furthest offshore, and as illustrated by figs. 4.6a and 4.6d, they are the most exposed to wind from all directions. Location 1 is by far the most similar to the overall wind in the area, shown in fig. 4.3a, which is natural as a relatively large part of the section consists of similar offshore conditions not hemmed in by island or fjord. They both also display the highest mean wind speeds for ASAR wind estimates, as well as model estimates for location 1, with mean wind speeds of $\mu_{1,ASAR} = 9.1$ m/s ,$\mu_{4,ASAR} = 8.62$ m/s and $\mu_{1,MODEL} = 9.4$ m/s, $\mu_{4,MODEL} = 8.8$ m/s. Location one has the highest correlation coefficient between ASAR and model wind estimates of all the points, $\rho = 0.54$, while both locations 1 and 4 have the lowest RMSDs, with 3.2 m/s and 3.1 m/s respectively. All in all, the overall impression is that the model and ASAR wind estimates correspond best for these two locations. It is reinforced by the Weibull pdf estimate in figs. 4.7a and 4.7d, which shows nearly identical pdfs for location 4 and very similar ones for location 1. The standard deviation and the scatter plots in figs. 4.8a and 4.8d are more ambiguous, and show that while RMSD and bias might be among the lowest, and correlation relatively high for this data, there is still quite a spread in the data. Model standard deviation is as high as 3.5 m/s for location 1 and 3.1 m/s for location 4, while for the ASAR estimates it's 3.1 m/s and 2.9 m/s.

Wind roses for locations 2 and 3 (figs. 4.6b and 4.6c) also display wind from most directions. For location 2 particularly, we can reasonably assume the southerly wind would be directed around the small island to the south. Location 2 has the highest bias, with -2,3 m/s, which means that model wind estimates are generally higher than ASAR wind estimates. We can also see this in the mean wind speeds of the location, with $\mu_{ASAR} = 6.1$ m/s and $\mu_{MODEL} = 8.4$ m/s. Location 2 also has the highest RMSD, of 3.9 m/s.

Locations 5 and 6 (figs. 4.6e and 4.6f) both lie at the mouth of fjords, which we can see from figs. 4.6e and 4.6f very strongly affects the wind direction, which seems to generally be funnelled up the fjords. If we look at fig. 4.6f, there is hardly any wind from the north-east to south-east, where the islands of Kågen and Arnøya lie as barriers. These locations both have the lowest bias, but also the lowest correlation of them all; only 0.35 and 0.44 respectively, despite the fact that the mean winds for model and ASAR winds are quite close ($\mu_{5,ASAR} = 6.3$ m/s,$\mu_{5,MODEL} = 6.4$ m/s and $\mu_{6,ASAR} = 7.8$ m/s, $\mu_{6,MODEL} = 7.8$ m/s). For location 6,

there is a large difference in the model and ASAR Weibull pdf estimate shown in fig. 4.7f, with the ASAR wind estimate showing a much larger spread in wind speeds. This is also clearly illustrated in the scatter plot in fig. 4.8f.

If we calculate the wind power density as described in section 3.4.5, we get the results in table 4.2, with the difference calculated as $P_{DIFF} = P_{ASAR} - P_{MODEL}$. As these estimates are based on only 103 data points for each location, they can not be considered accurate estimates, but serve as a guide for comparison.

Location	1	2	3	4	5	6
Model	717.9 W/m^2	530.6W/m^2	664.7W/m^2	586.9W/m^2	254.1W/m^2	401.0W/m^2
ASAR	634.9W/m^2	233.3W/m^2	415.2W/m^2	539.4W/m^2	299.6W/m^2	533.7W/m^2
Difference	-83.0W/m^2	-297.3W/m^2	-249.4W/m^2	-47.4W/m^2	45.5W/m^2	132.7W/m^2

Table 4.2: Power density for selected locations

In the scatter plots in figs. 4.8a to 4.8f, certain data points are highlighted. These represent three dates when the difference between the model wind estimate and the ASAR wind estimate was larger than 10 m/s for either one of the locations in the selection. We can see that for all of the dates, the discrepancy between ASAR and model wind estimates is not consistent across the scene. While the estimates for 13 January 2011, highlighted in red, are divergent with as much as 13.6 m/s in location 5, the discrepancy is nowhere near as large for the other 6 locations in the scene. The same is true for 25 February 2011 (highlighted in blue) which has its strong divergence in location 1, and 16 April 2011 (highlighted in magenta) which diverges in location 2.

This small test by no means capture all the locations that diverge strongly, nor does it imply that any diverging locations not highlighted are considered close estimates. 10 m/s is a limit chosen to find some of the locations which diverge most strongly.

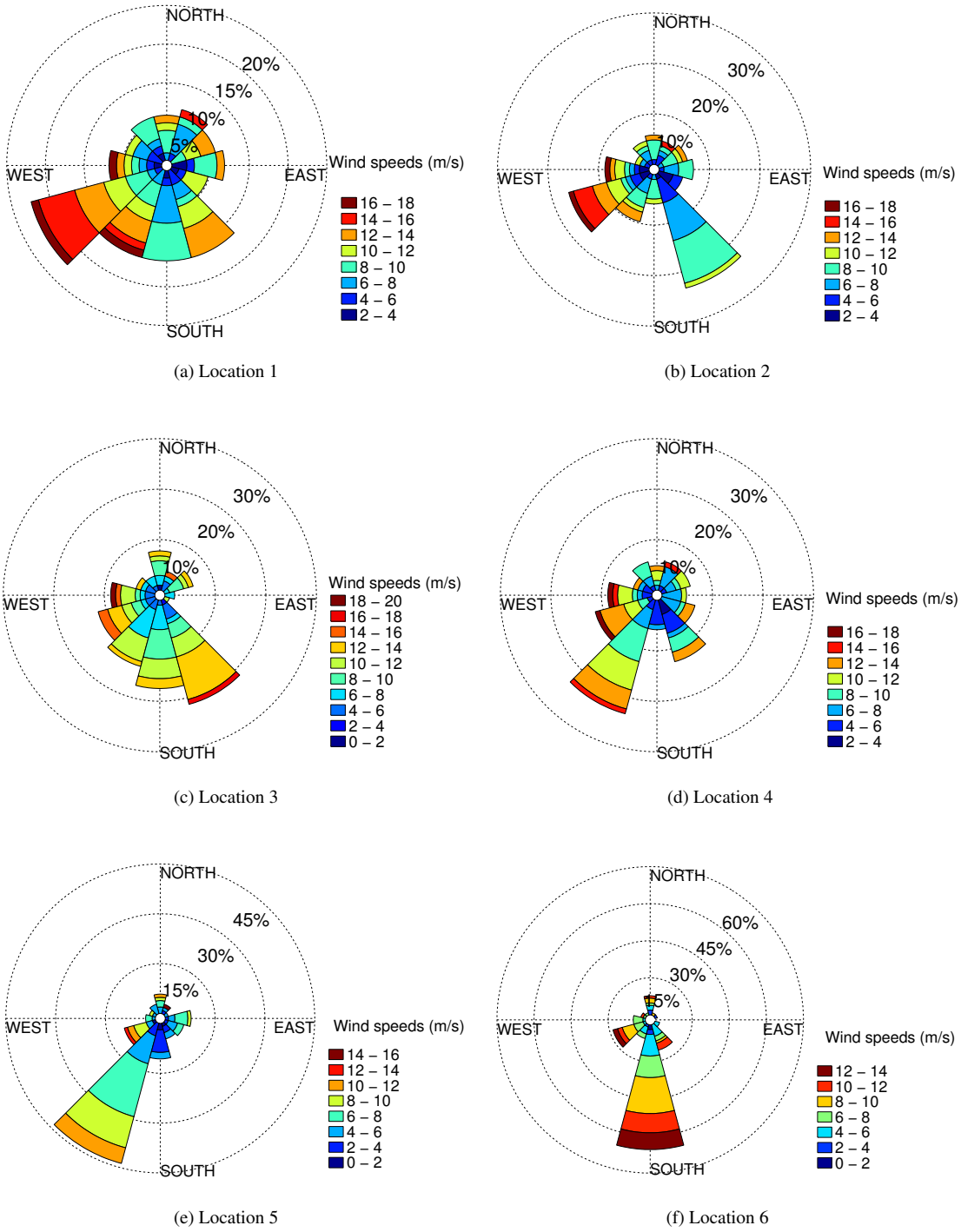

(a) Location 1

(b) Location 2

(c) Location 3

(d) Location 4

(e) Location 5

(f) Location 6

Figure 4.6: Wind roses of model wind directions for the selected locations.

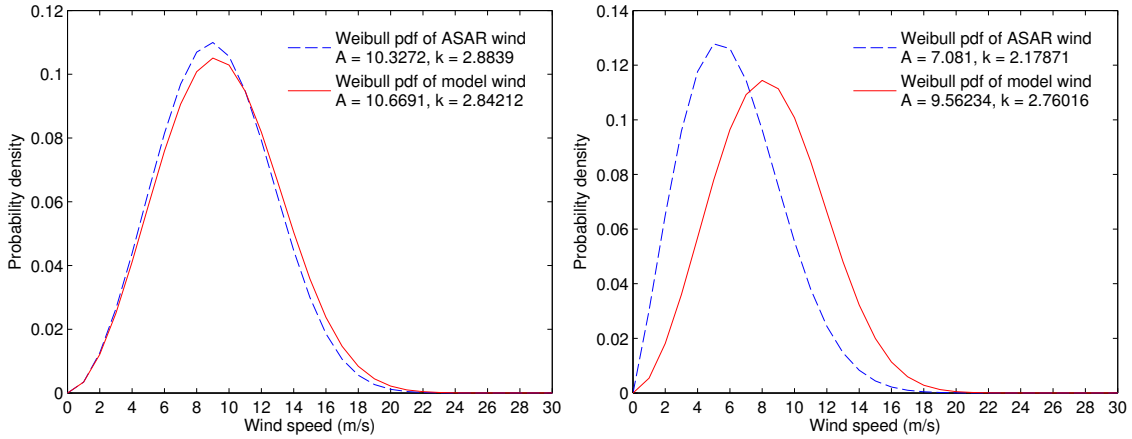

(a) Location 1

(b) Location 2

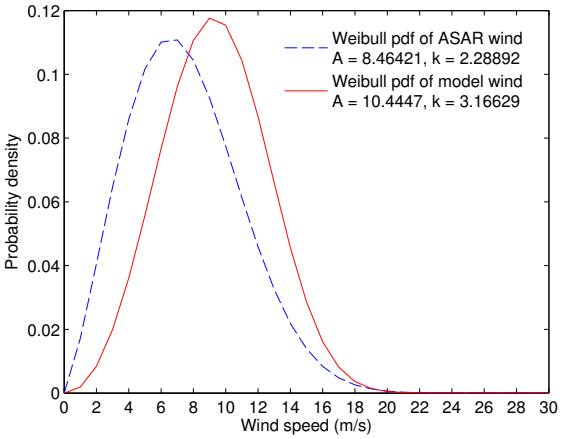

(c) Location 3

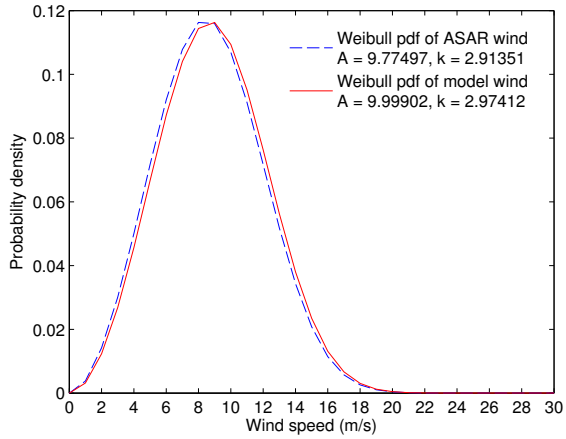

(d) Location 4

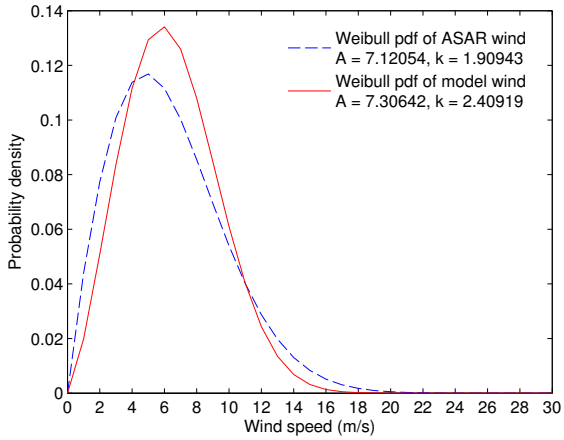

(e) Location 5

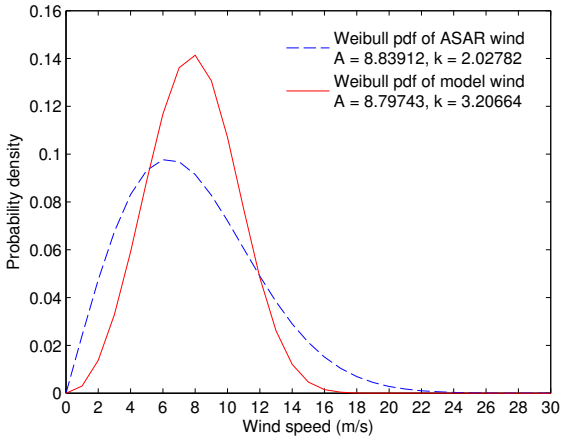

(f) Location 6

Figure 4.7: Estimated Weibull PDFs for the selected locations.

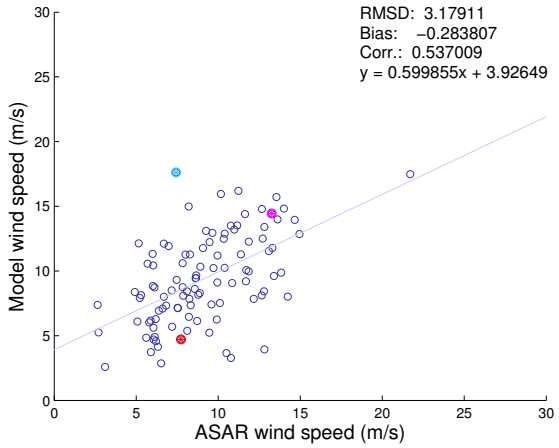

(a) Location 1

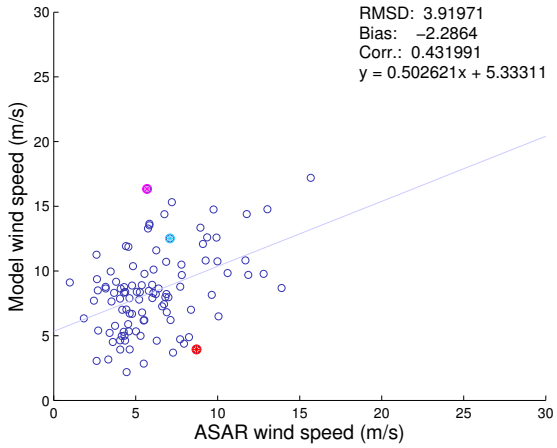

(b) Location 2

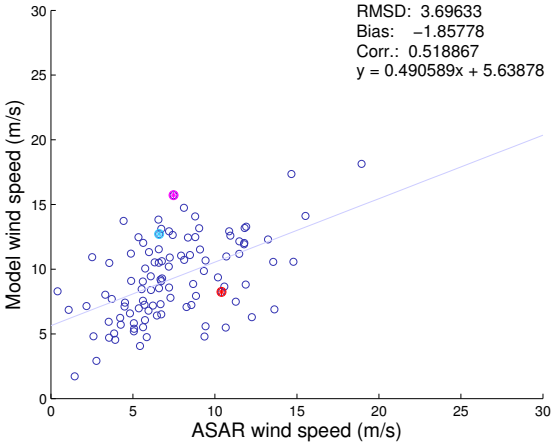

(c) Location 3

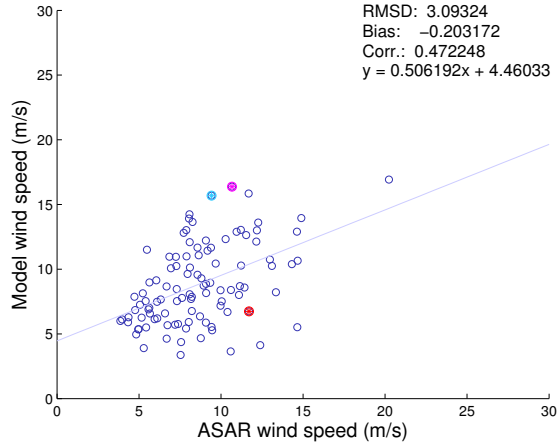

(d) Location 4

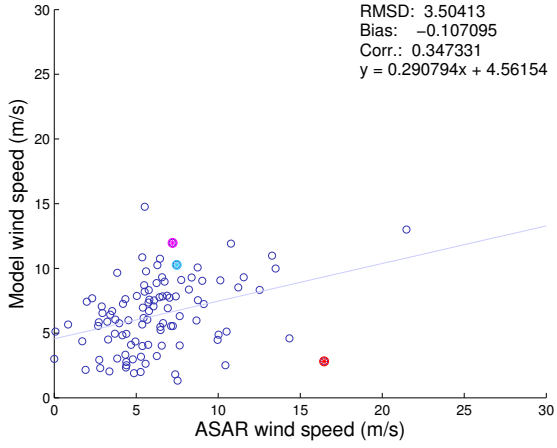

(e) Location 5

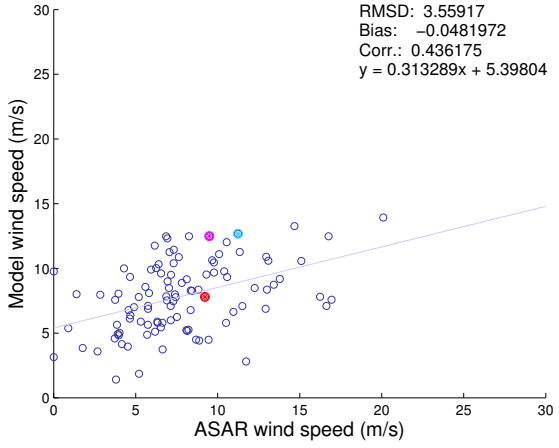

(f) Location 6

Figure 4.8: Scatter plots for the selected locations.

4.2.1 Fakken

The results for the Fakken in-situ measurements and model wind estimates are presented in table A.3. Figures 4.9a and 4.9b show wind roses based on the measurements from the Fakken 10m meteorological mast and the model wind estimates, respectively. As we can see, the wind directions for the model wind estimates are far more limited to south-easterly and south-westerly, than the in-situ measurements. The RMSE is quite large, with 4.22. Both the in-situ wind speeds and wind directions show a higher standard deviation than the model ones, with $\sigma_{DIR} = 71.2^\circ$ and $\sigma_{SPEED} = 5$ m/s for in-situ and $\sigma_{DIR} = 66.7^\circ$ and $\sigma_{SPEED} = 3$ m/s for model winds. It follows that the difference in variance will also be very large, and we have that $\sigma^2_{MODEL} = 8.8$ and $\sigma^2_{IN-SITU} = 15.5$.

Figures 4.9c and 4.9d show the Weibull pdf estimates along with theoretical maximum power in the wind based on the wind speed histograms for model and in-situ winds. The power plots have both been normalized in relation to the peak power of the in-situ plot, to make the comparison easier. In the pdf estimate for the in-situ wind measurements, we can clearly see the impact the higher frequency of higher wind speeds has on the theoretical power production, when compared to the model plots. If we calculate the theoretical wind power density, we find that with the model prediction of the wind, $P = 309.5W/m^2$, and with in-situ observations $P = 809.8W/m^2$.

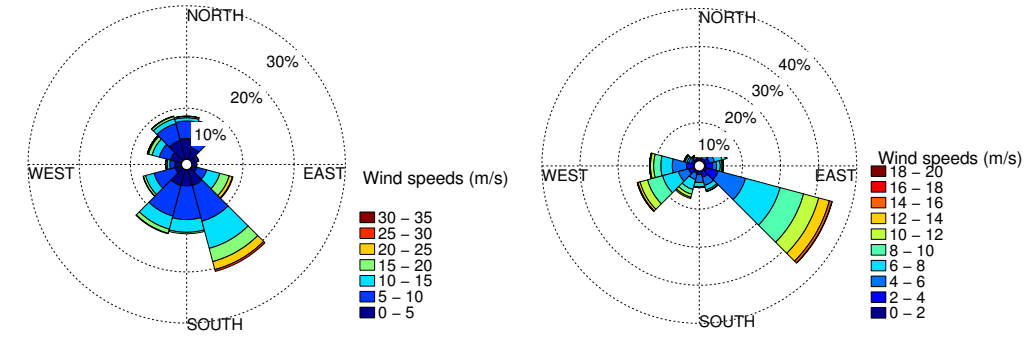

(a) Windrose of in-situ wind for Fakken

(b) Windrose for model wind for Fakken

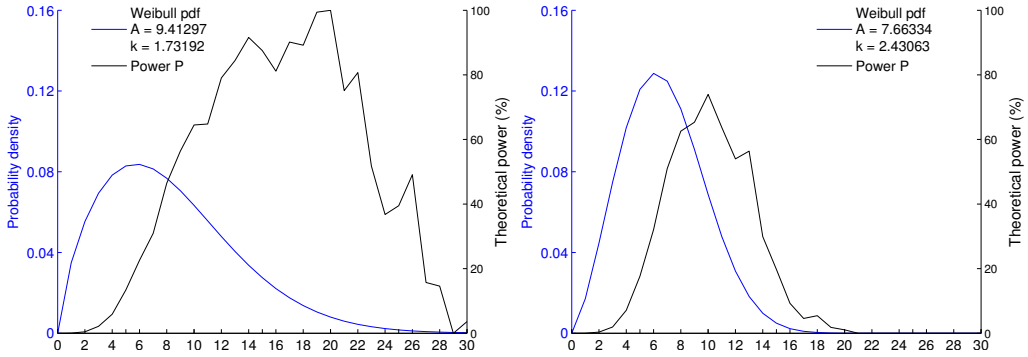

(c) Weibull pdf and theoretical power for in-situ observations

(d) Weibull pdf and theoretical power for model prediction

Figure 4.9: Wind roses and distributions for the Fakken wind farm.

4.3 Seasonal and diurnal variations

4.3.1 Seasonal variations

Scatter plots for different months have not been made, as the number of available days varies quite a bit between the months. However, the data has been organized by season, which are plotted as scatter plots in fig. 4.11 and wind roses in fig. 4.10. The most notable thing about the seasonal variability is the large discrepancy between the model mean wind speeds and ASAR means. Model mean wind speeds varies through the seasons with between 8 m/s and 8.5 m/s, with the largest difference between winter and summer. The ASAR mean wind estimates, however, are as low as 6.8 m/s for autumn and up to 8.5 m/s in the spring. The correlation coefficient varies from 0.52 for winter months, to 0.56 for autumn and spring. The only notable difference in terms of wind direction is that spring has the only occurrence of predominantly easterly wind, with a mean wind direction of 92.6°.

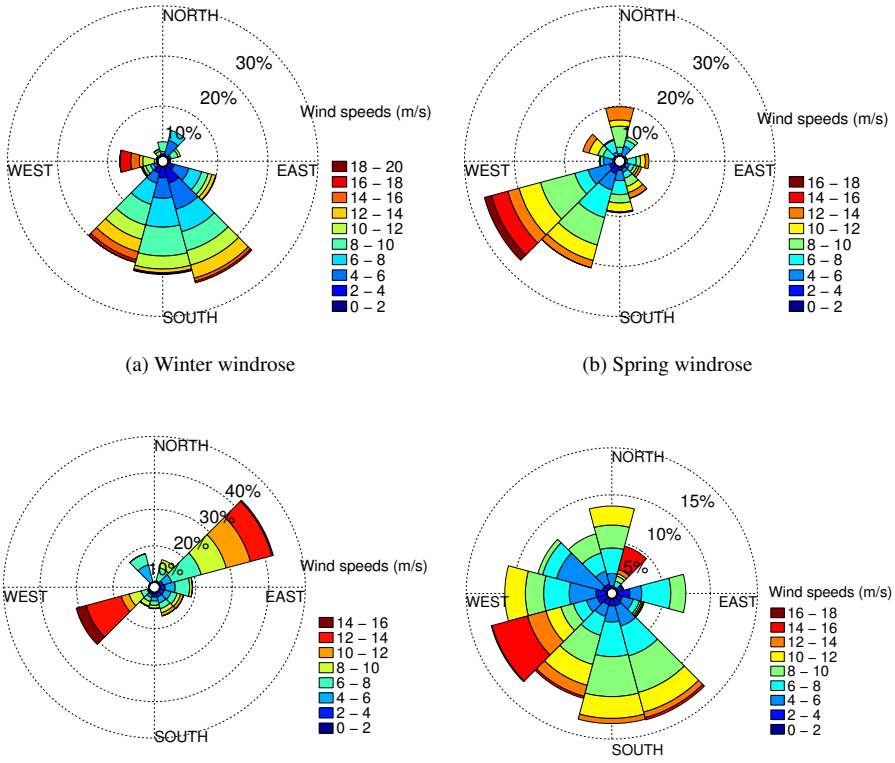

(a) Winter windrose

(b) Spring windrose

(c) Summer windrose

(d) Autumn windrose

Figure 4.10: Model wind wind roses for the 2011 seasons

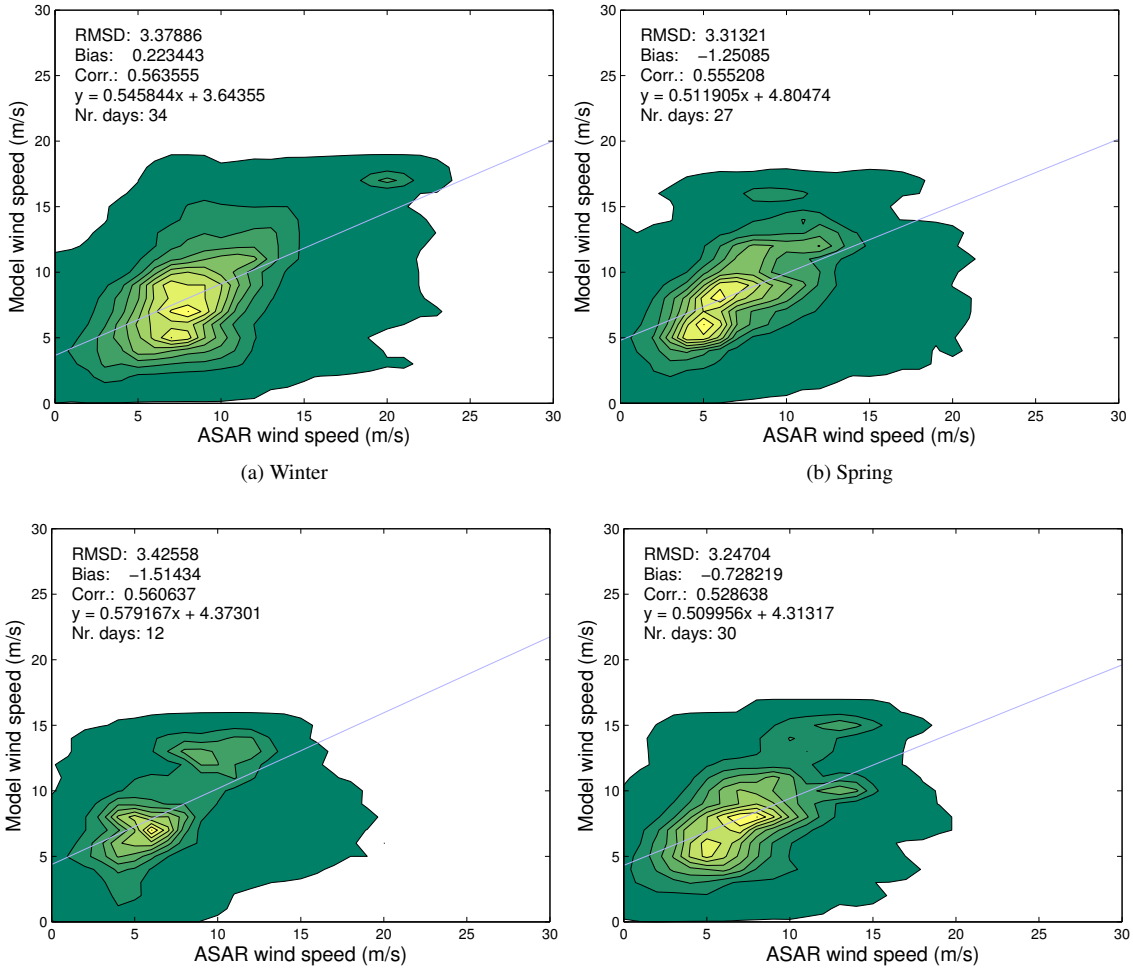

(a) Winter

(b) Spring

(c) Summer

(d) Autumn

Figure 4.11: Scatter plots for the 2011 seasons

4.3.2 Diurnal variations

There is often a diurnal pattern to wind speeds, with onshore winds having higher speeds during the day and lower during the night. Offshore and coastal areas have been shown to sometimes display an inverted diurnal wind pattern, with the highest wind speeds occurring during the night (Sempreviva et al., 2008). This is difficult to examine with ASAR data, as the satellite passes generally occur at fixed times. For this area the overpass times are around 09:00 and 19:00, at hours when the diurnal pattern would not be at it's strongest. Figures 4.12a to 4.12d show scatter plots and statistics for morning and evening passes. There is a slightly higher variance for model morning wind over evening ($\sigma^2_{9,MODEL} = 11.58$ over $\sigma^2_{19,MODEL} = 10.36$), and this difference is even larger for ASAR winds ($\sigma^2_{9,ASAR} = 14.95$ over $\sigma^2_{19,ASAR} = 10.99$). Aside from this, there are no remarkable differences.

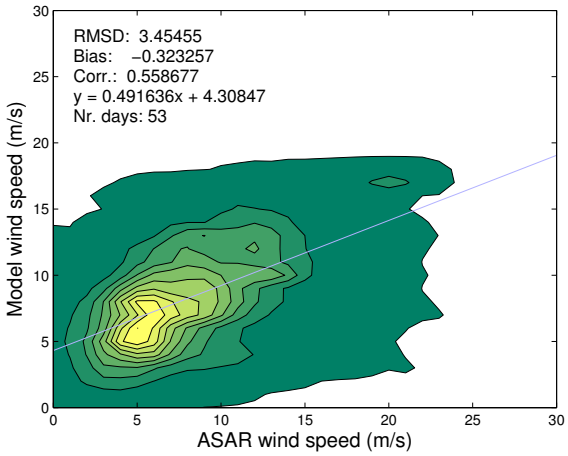

(a) Morning

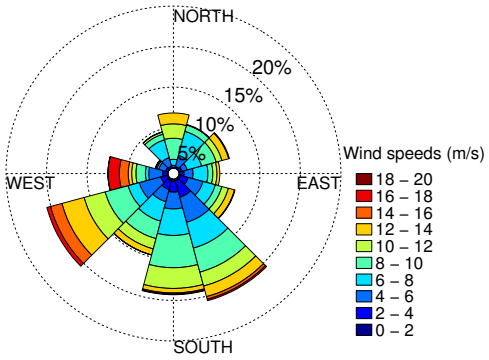

(b) Morning wind rose

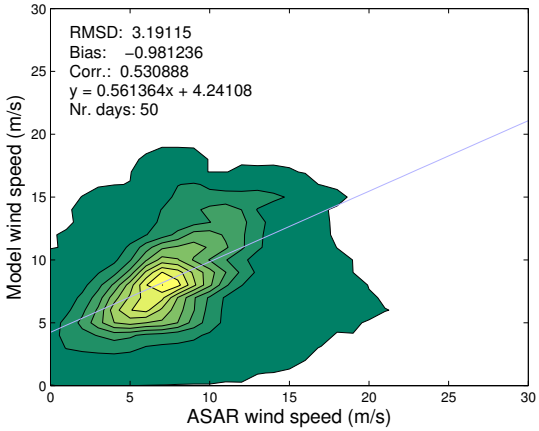

(c) Evening

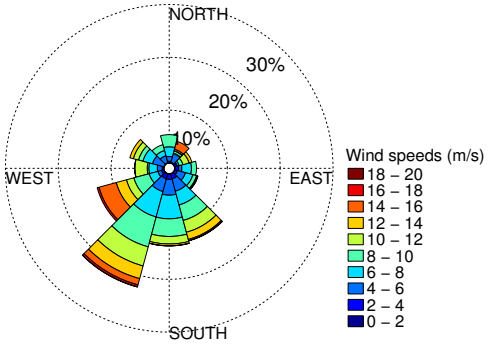

(d) Evening wind rose

Figure 4.12: Scatter plots for diurnal variations

4.3.3 Wind speed variations

To examine how the ASAR and model wind estimates compare for different wind speeds, scatter plots of the estimates have been made for low (under 5 m/s), medium (from 5 m/s to 8 m/s), and high (over 8 m/s) wind speeds. The selection has been made based on mean ASAR wind speeds for each scene. (Note in table A.2 that the selection was done based on the mean of each individual scene, but the mean of all the scenes for each separate time group is slightly higher.) There is a a slight increase in the correlation coefficient from low wind speeds (0.38) to high (0.52), but as seen in figs. 4.13e to 4.13a, the RMSD increases as well as well as the standard deviation.

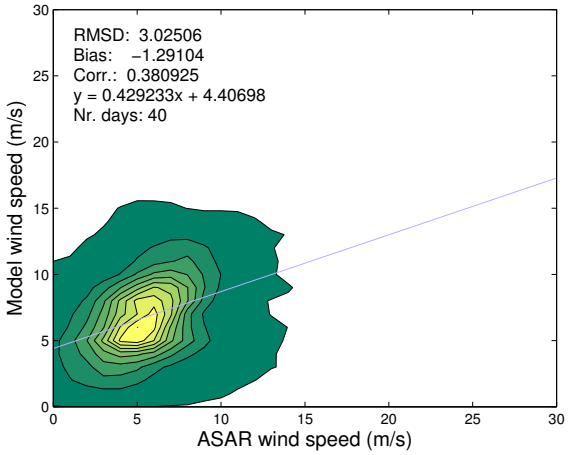

(a) Mean ASAR wind speed under 5 m/s

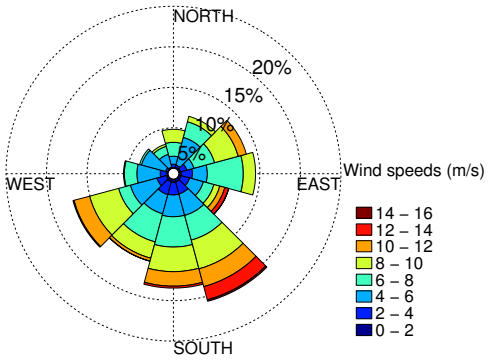

(b) Low wind speed windrose

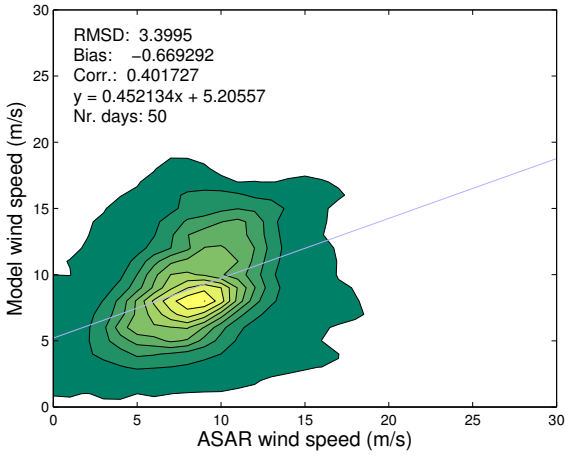

(c) Mean ASAR wind speed between 5 and 8 m/s

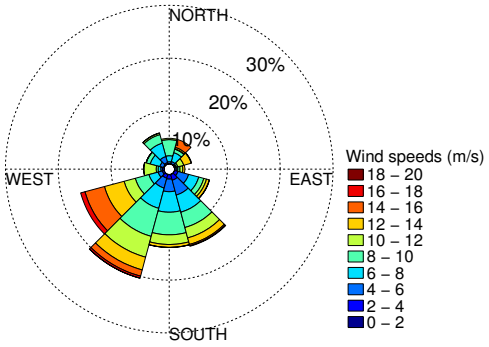

(d) Medium wind speeds windrose

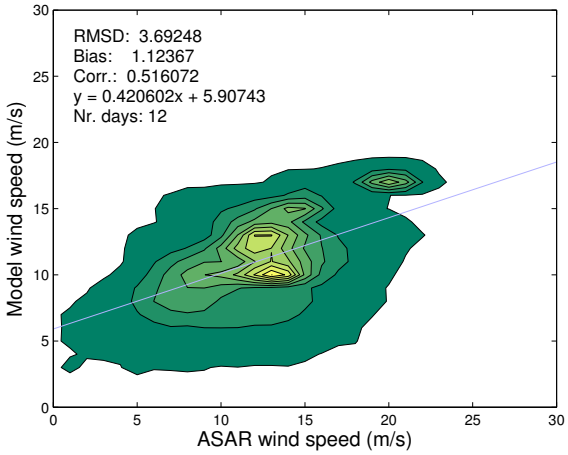

(e) Mean ASAR wind speed over 8 m/s

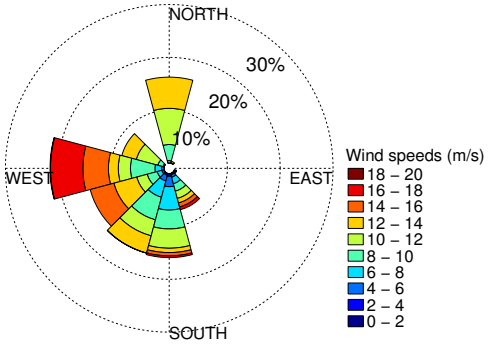

(f) High wind speeds windrose

Figure 4.13: Scatter plots for speed variations

4.4 Detailed analysis of scenes

Data for all the selected dates are presented and described below. This is organized by date, as a thematic organization of the scenes would be rather more disorganized. The description of the scenes will come first, with the corresponding data from these selections presented in figs. 4.14 to 4.20. Additional statistics can be found in appendix A. Figure 4.21 shows an illustration of the RMSD for each pixel using all 103 scenes.

4.4.1 13 January 2011

The scene for 13 January 2011 is one of the scenes which are highlighted in the scatter plots in fig. 4.8, this one in red, due to a large discrepancy between ASAR and model wind estimate. In this case we can see quite easily that the offending location is number 5, in which the ASAR wind estimate shows far higher wind speeds than the model estimate. This becomes all the more apparent as the estimates for rest of the scene generally correspond quite well. If we look at the difference image in fig. 4.14d, we see that the green shade indicating low difference is very present, aside from in a few areas. The ASAR estimates a somewhat lower wind speed in the bays south of Vannøya, and it extends further out than the wind shadows predicted by the model. The ASAR also estimates a somewhat higher wind speed than the model east of Fugløya, where the model seems to predict some slowing down of the wind around and over Arnøya. The RMSD is rather large, with 4.48, and so is the difference in variance between the ASAR and model estimates, with merely 2.9 for the model winds and 7.9 for ASAR.

4.4.2 25 February 2011

In fig. 4.15 we can see that there's a very large discrepancy between the ASAR and model wind estimates, which don't seem to be directly connected to specific geographical features. In fact, the area to the north-west, where the wind seems to come rather unimpeded up along the coast, is where we find the largest difference. The ASAR wind estimates is consistently much lower than the model estimate, and there is a very large RMSD (6.19) as well as bias (-5.24). To give a better idea of possible causes, fig. 4.16 includes two figures which show the model wind estimates on a regional scale 14 hours before and 10 hours after the ASAR scene was captured.

4.4.3 16 April 2011

The wind estimates for 16 April 2011 have a similarly large discrepancy as those described in section 4.4.2 for 25 February 2011. However, the ASAR wind estimates correspond somewhat better in some high wind speed areas offshore. Wind streaks in the ASAR image in fig. 4.17c indicate that the wind direction matches the model wind direction quite well. There are frequent occurrences of wind shadows in the ASAR wind estimates, particularly around Vannøya and north-east of Nordkvaløya where they can be seen as elongated streaks of lower wind speeds in connection with the mountains in the northern regions. These are mostly missing from the model wind estimates, which on the whole predicts a much higher wind speed even in the lee areas.

4.4.4 13 January 2012

This scene is one of the few occasions where the dominant wind direction is from the north. However, the wind coming up the fjords from the south indicate that the wind pattern at this moment in time was rather

turbulent. A look at the regional model wind conditions were included in fig. 4.19 to get a better overview of this. The wind speed is generally low, though there is evidence in the ASAR wind estimate in fig. 4.18a of higher wind speeds along the northern tip of Vannøya and Nordkvaløya, where the wind meets the coast at a very low angle. The model wind predicts higher wind speeds up along the fjord to the south, which the ASAR estimates do not agree on. The most obvious feature, however, is the band of quiet running through the image, presumable created by the meeting winds in the model. This appears in the ASAR wind map as a light streak, but is not evident from the ASAR image itself. However, the wind feature in the north-eastern corner is present in both ASAR image and wind map.

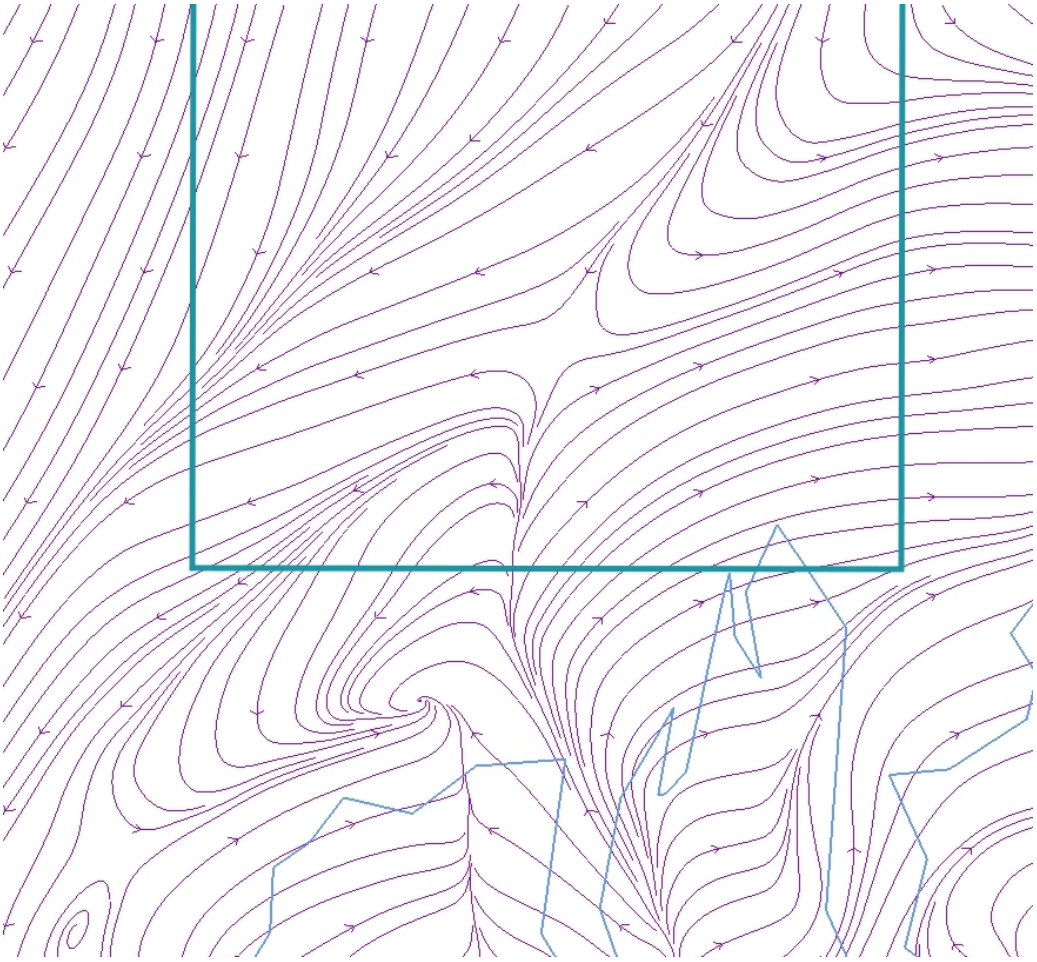

Figure 4.19: Regional model wind vectors for 13 January 2012.

4.4.5 27 February 2012

A strong wind is coming from the south and south-east in this scene, largely funnelled up the fjords and fanning over the area. It's interesting to see in this scene that the high wind speed through Fugløyfjorden

and up the Lyngen fjord to the east is the feature the model and ASAR wind estimates agree best on. However, when it comes to wind shadowing and speed-up they differ quite a lot. A notable feature is the large discrepancy between the wind estimates north of Arnøya, where the model predicts much lower wind speeds, while the ASAR wind map shows an increase in speeds around the western edge of the island. There is also a distinct difference in wind speed at the mouth of the Ullsfjord, where different model wind directions meet at an angle.

4.4.6 RMSD illustration

To better illustrate the spatial distribution of the difference in the wind estimates, the root mean square deviation of each individual pixel for all 103 scenes has been calculated, and then plotted in fig. 4.21. From this we can get a clearer idea of which areas are more prone to differ between model and ASAR wind estimates. The RMSD values range from 2.25 to 7.46, and of 11999 un-masked pixels, only 48 had values over 5. To better highlight the range in the image, the colorbar limits were set to [0,5] and all pixels over 5 highlighted in white.

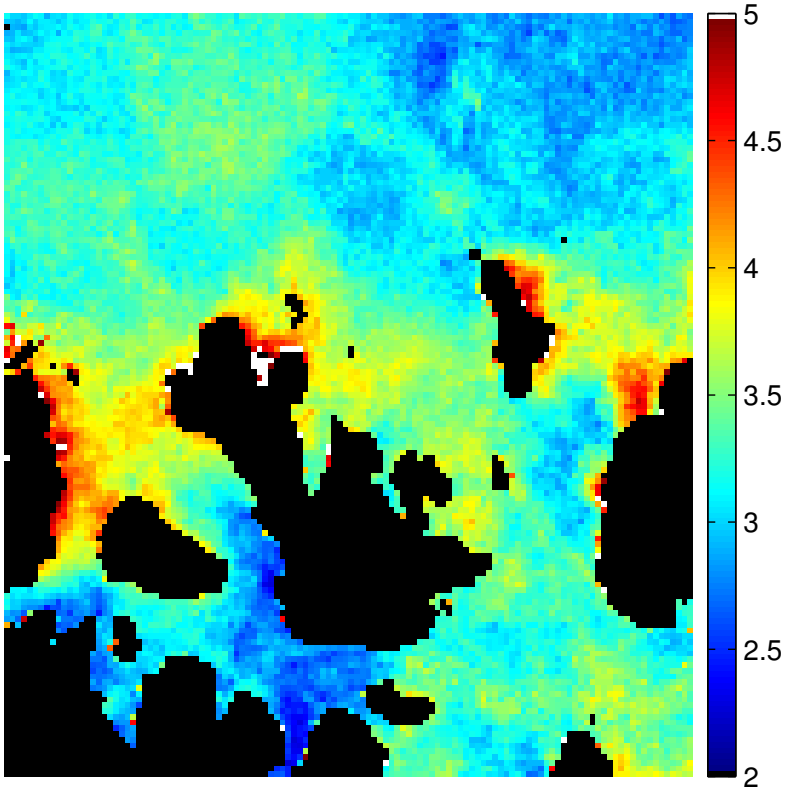

Figure 4.21: Visualisation of RMSD of each pixel for all 103 scenes from 2011.

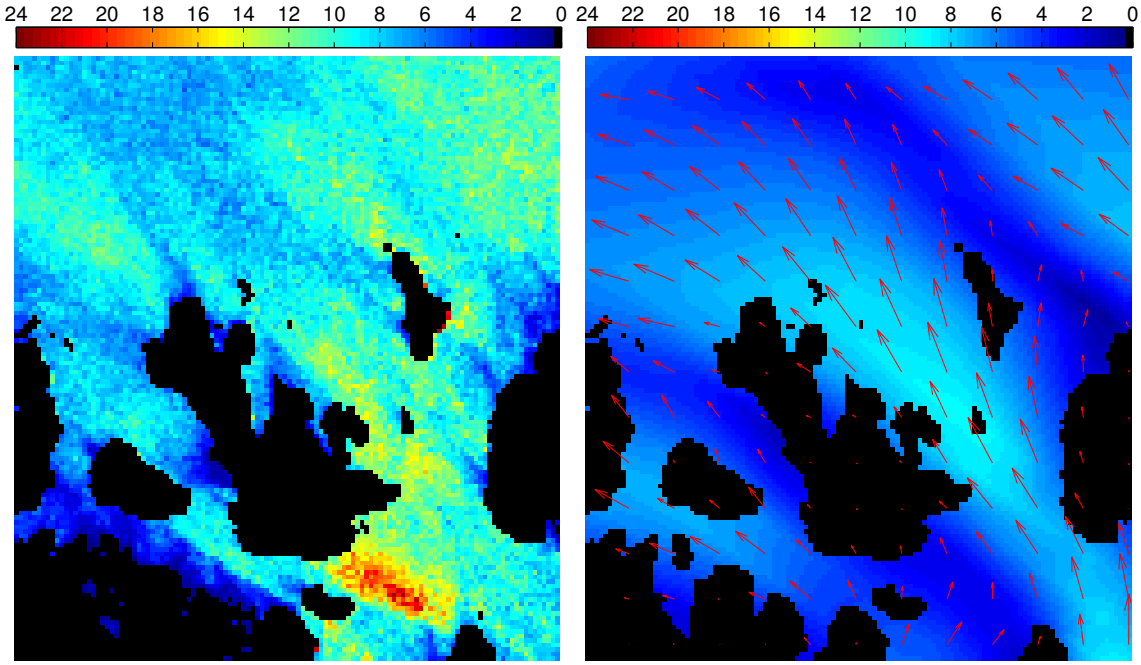

(a) ASAR wind map

(b) Model wind map

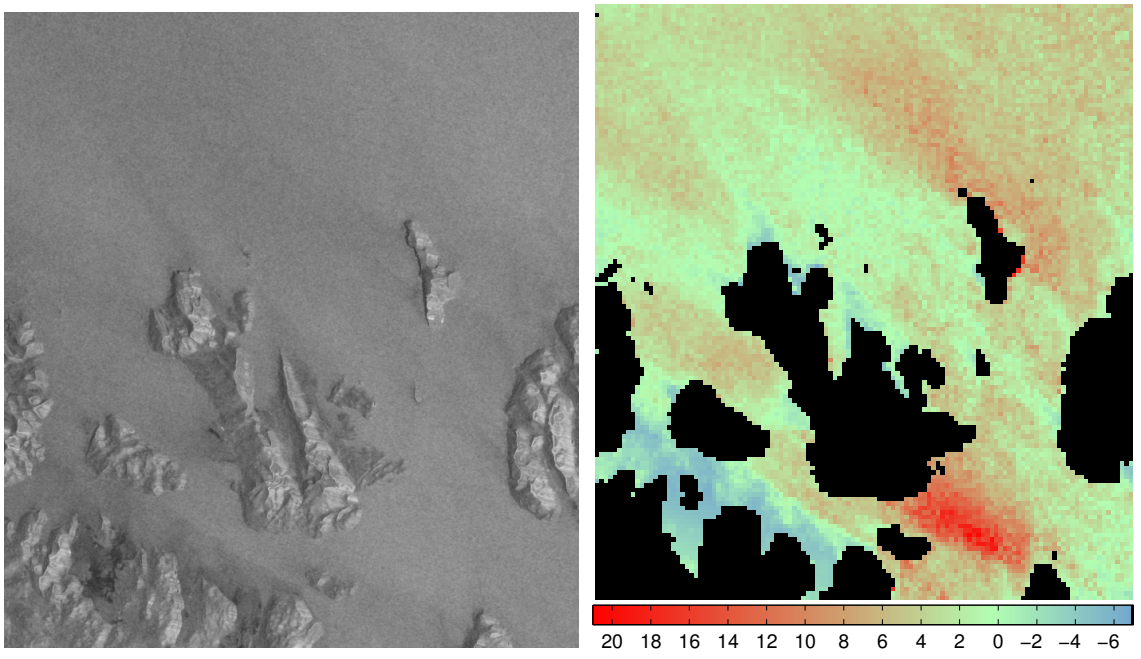

(c) ASAR image

(d) Difference image of wind maps

Figure 4.14: Illustrations of ASAR and model wind estimates for 13 January 2011.

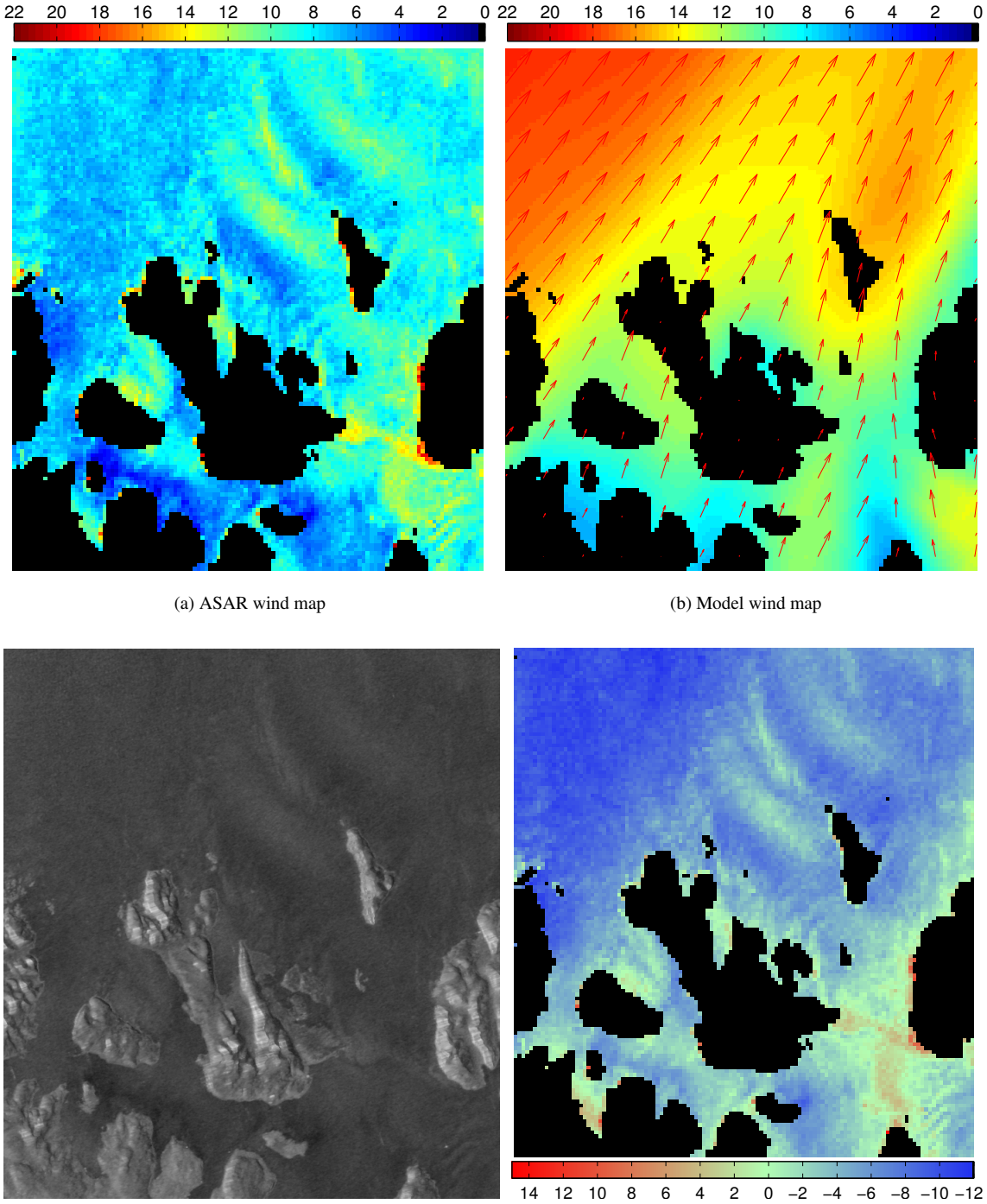

(a) ASAR wind map

(b) Model wind map

(c) ASAR image

(d) Difference image of wind maps

Figure 4.15: Illustrations of ASAR and model wind estimates for 25 February 2011.

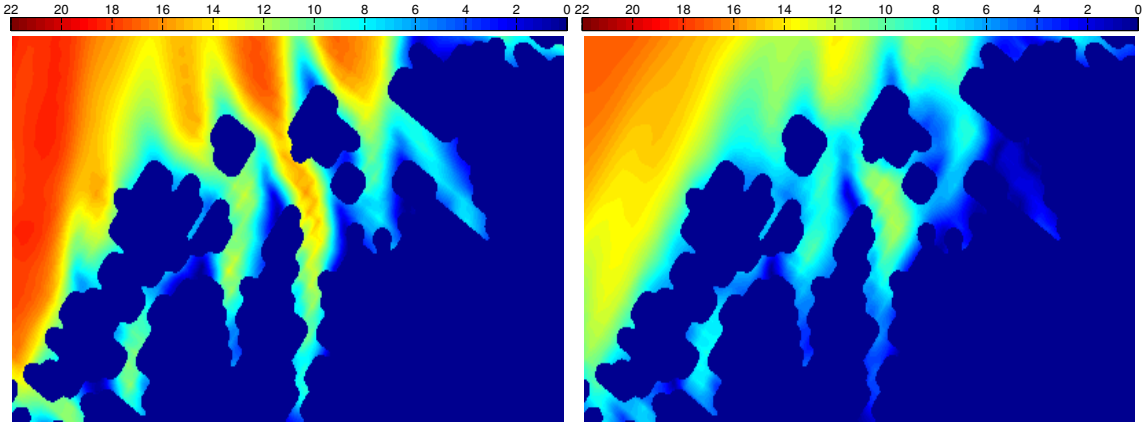

(a) Model winds 25 February, 06:00

(b) Model wind 26 February, 06:00

Figure 4.16: Illustrations of regional model wind estimates for hours before and after the ASAR time.

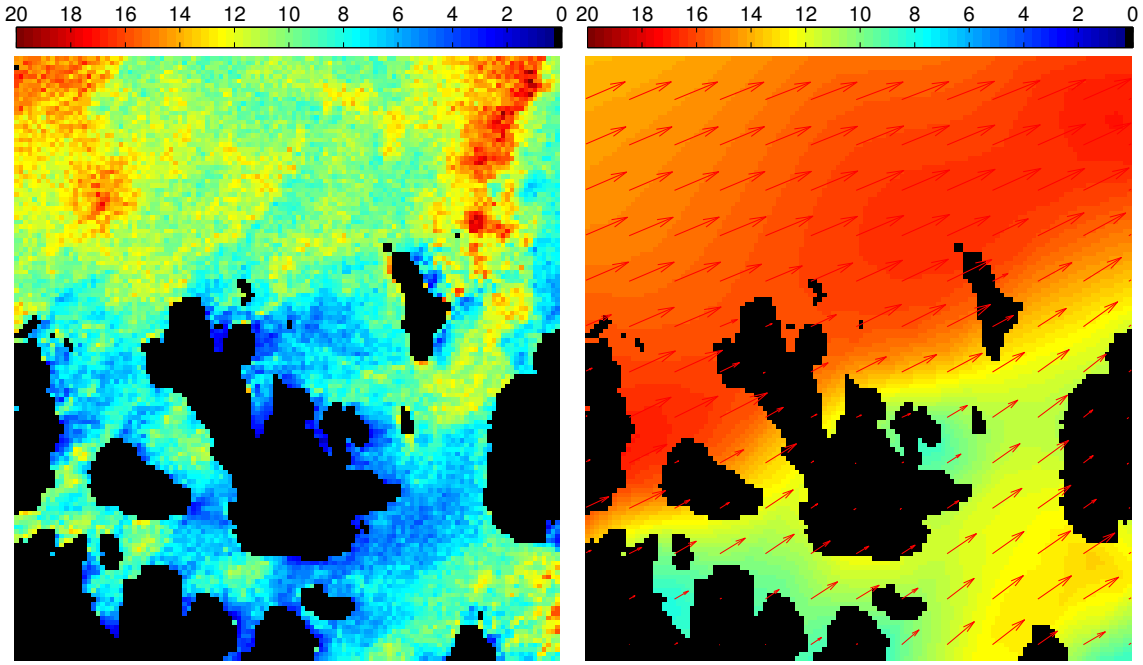

(a) ASAR wind map

(b) Model wind map

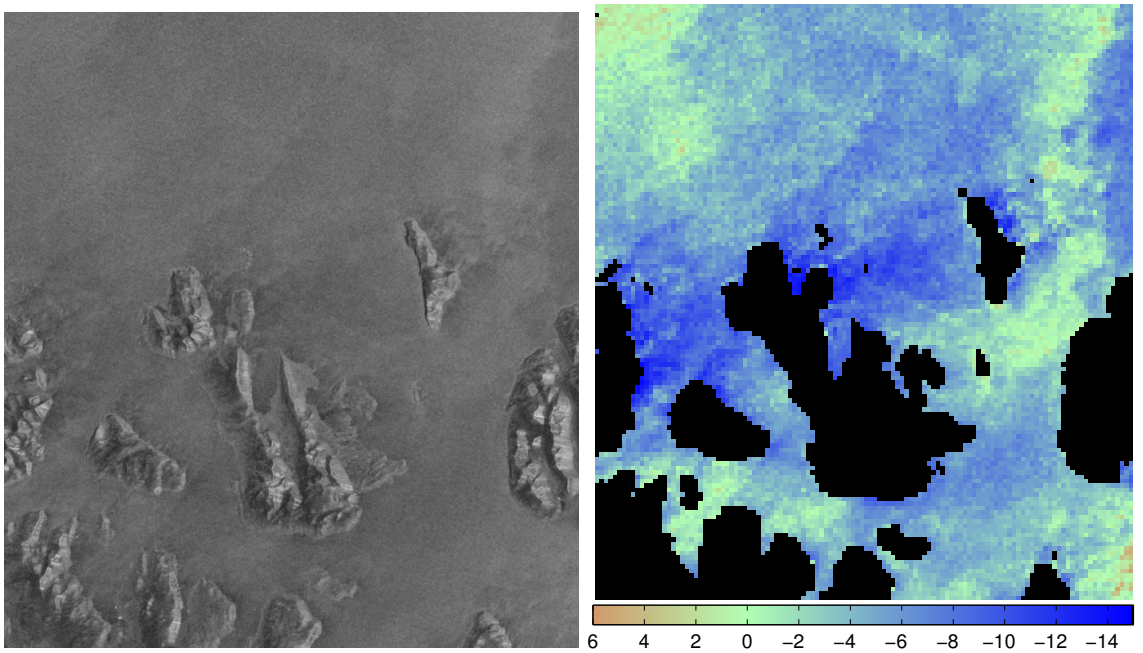

(c) ASAR image

(d) Difference image of wind maps

Figure 4.17: Illustrations of ASAR and model wind estimates for 16 April 2011.

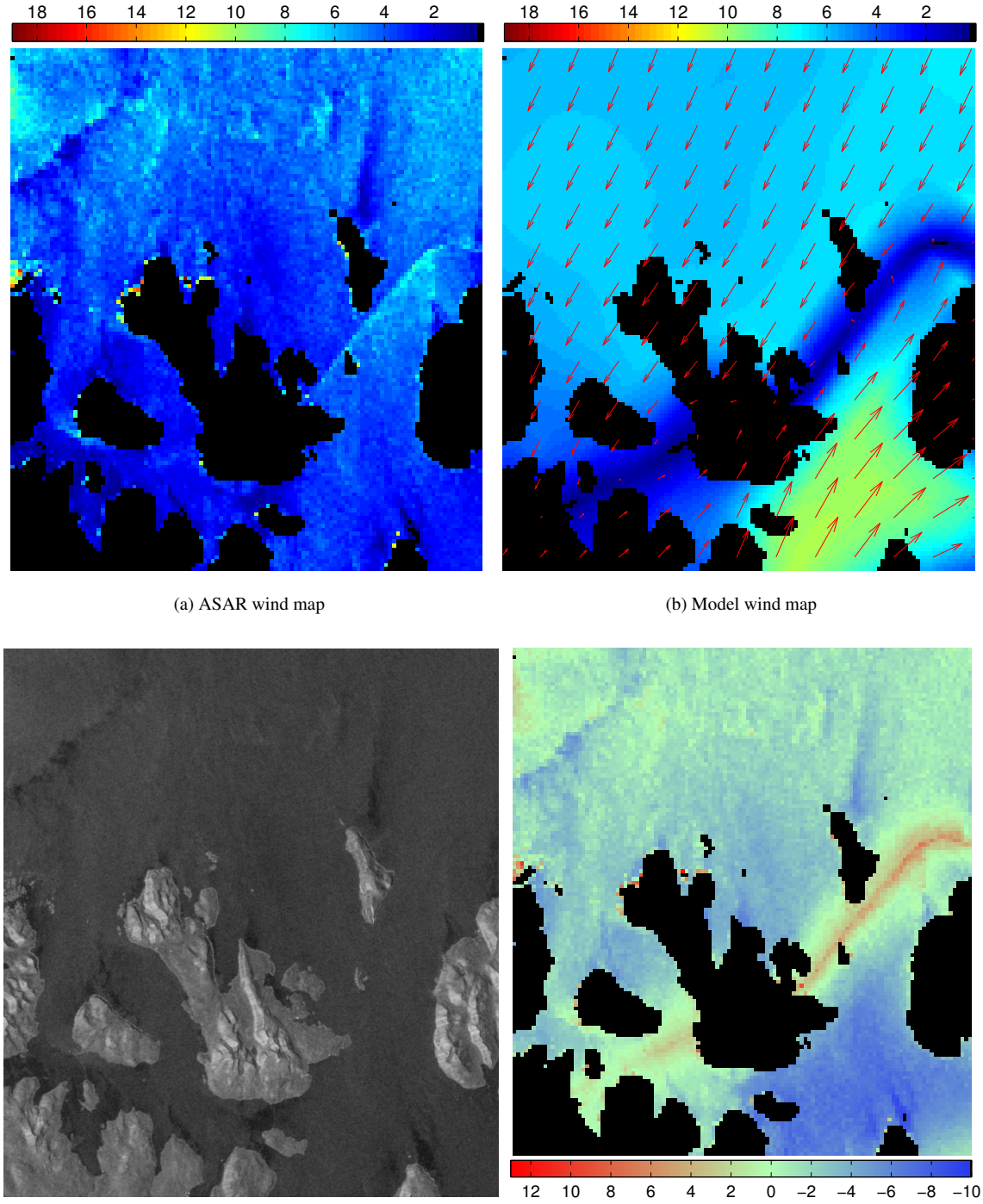

(a) ASAR wind map

(b) Model wind map

(c) ASAR image

(d) Difference image of wind maps

Figure 4.18: Illustrations of ASAR and model wind estimates for 13 January 2012.

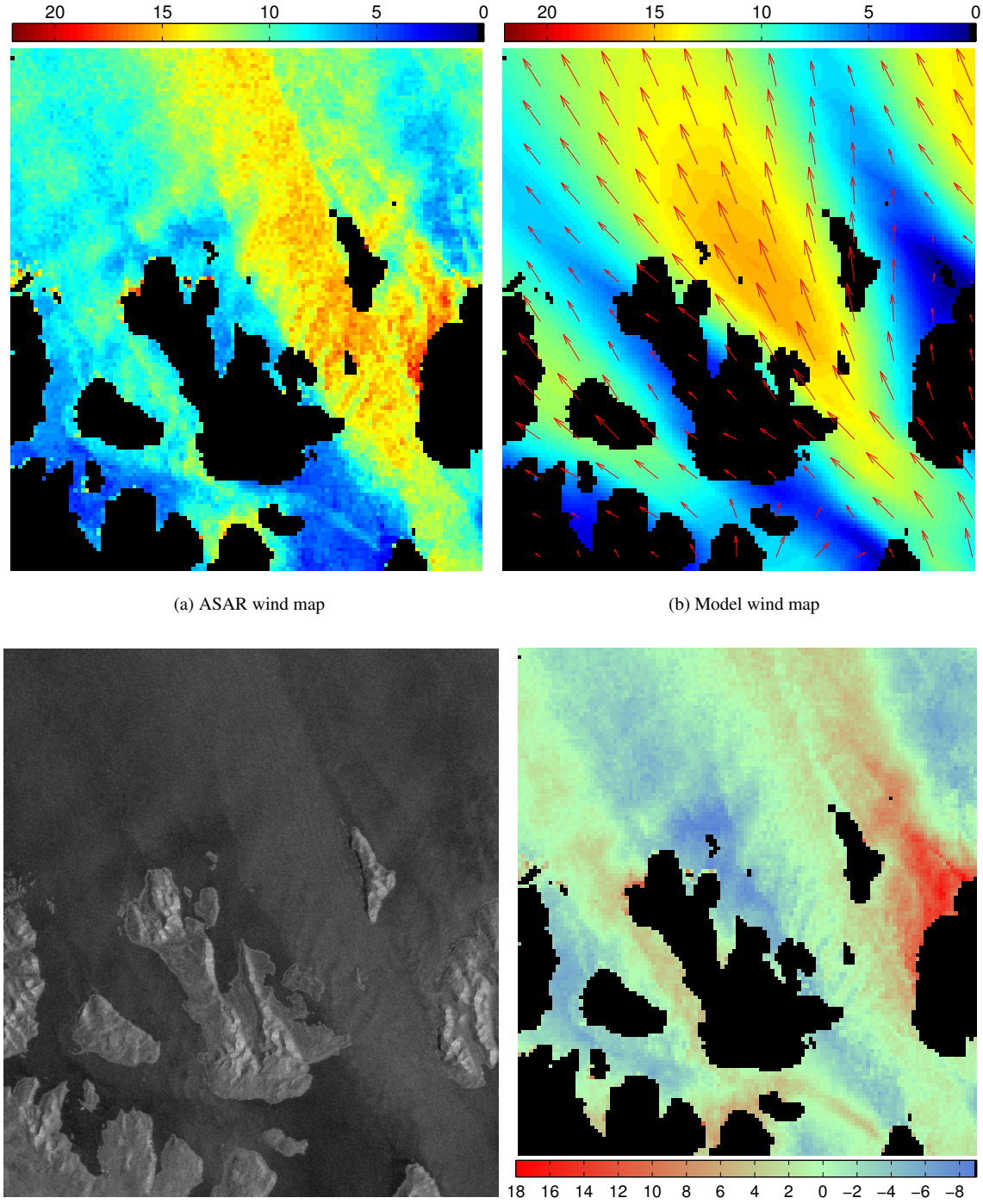

(a) ASAR wind map

(b) Model wind map

(c) ASAR image

(d) Difference image of wind maps

Figure 4.20: Illustrations of ASAR and model wind estimates for 27 February 2012.

Chapter 5

Discussion

The presentation of the results showed that there are many different aspects of the data which must be considered when using ASAR or model wind estimates to evaluate wind climate. The following discussion will first consider the spatial features identified in the ASAR and model wind maps, including geographical and atmospheric sources, before addressing some of the statistical features of the data. Finally, a discussion on the implications of these will be done later in the chapter.

5.1 Geographical features

Certain features of the terrain affects the wind climate in the area, but is not necessarily described equally well by ASAR and model. As the area is relatively mountainous, as can be seen from the map in fig. 4.2, some things which we might expect to occur frequently are wind speed up and shadowing effects. Examples of probable wind speed up effects can be seen to varying degrees in the ASAR wind maps, such as in fig. 4.14a, where the northerly wind hits the south-western edge of Arnøya at a low angle, and larger wind speeds are seen. This feature is not as evident in the model wind maps. The challenge with identifying speed up effects in the ASAR wind map is that the land mask can at times cover the effect if it occurs very close to land. Another challenge can be seen frequently around the northern tip of Vannøya and eastern side of Nordkvaløya. There are frequent indications of speed up effects in these areas, such as we can see in figs. 4.18a and 4.20a, and due to the relatively steep mountains found here, it is not unexpected. However, the wind direction evident in the model map in fig. 4.20b suggest that we might be seeing either evidence of human made structures such as boats, or insufficient land masking, and a closer look at the ASAR image in fig. 4.20c indicates the latter.

In the ASAR wind estimates for 27 February 2012 in fig. 4.20a, we see an indication of another form of speed up effect which is equally missed by the model. North-east of Arnøya, there is an area of very high wind speeds, though the model predicts very low wind speeds. And indeed the area might at first glance appear to be in the lee of the wind coming from the south-east, around or over Arnøya. But if we look at the map in fig. 4.2, we can see that the island in fact features rather high mountains of 500 m to nearly 1000 m, separated by valleys where we might get a speed up effect such as is indicated by the ASAR wind map. If we look at the map of the model terrain in fig. 4.1, however, we find a very different landscape. As we can see, Arnøya is indicated as a land mass with a height rising to roughly 400 m, which makes it unable to properly describe the movement of the wind. None the less, the result on the wind from this topographical feature is quite evident in the ASAR wind map.

A similar problem is encountered if we look at wind shadows. These feature in nearly all of the scenes, most frequently in the bays on Ringvassøya and the northern part of Vannøya. In these areas, the ASAR and model wind estimates correspond fairly well, though the spatial extent and magnitude of the wind shadows will vary. In the ASAR wind maps we can frequently connect them not just to the bay areas, but also the mountains surrounding them, indicated by longer streaks in the direction of the wind. This is another area where the lack of detail in the model becomes apparent, as some islands are missing entirely from the model, including a large part of northern Vannøya where we find a 757 m high mountain, and where wind shadowing would otherwise occur. An example of this can be seen in fig. 4.17, were there is a clear wind shadow behind Nordkvaløya and Vannøya. In fact, the wind shadows in the ASAR wind map correspond very well with the peaks on Nordkvaløya and northern Vannøya, however they are not at all present in the model wind map.

5.2 Atmospheric and ocean surface features

Several different features of the ocean and atmospheric boundary layer can be identified in the ASAR images. In the 25 February 2011 scene in fig. 4.15c, we can see streaks perpendicular to the wind in the south-east corner which are probably examples of either tidal waves or atmospheric gravity waves. In fig. 4.20c there are quite powerful examples of what are probably atmospheric gravity waves both in the center of the image and somewhat fainter at the south-east of Vannøya. These atmospheric waves modify the capillary waves on the ocean surface and give a strong indication of the wind conditions in this area. As described in section 2.1.2, they are connected with turbulence and rotors, which can have a potentially large negative effect on the power production, and cause turbine fatigue. The presence, magnitude, location and frequency of these features must be identified in connection with wind farm siting, to determine whether they entail such a deviation from normal wind conditions that they will significantly impact power production. That will not be accomplished from examining 5 ASAR images, but the location of the features in these images tell us something about the areas which should be examined further. The general effect on the wind speed from gravity waves might be present in the model estimates when the atmospheric or topographical sources of them are of a large enough magnitude. As the ASAR image reflects the near immediate wind conditions at the moment of capture, it will show the features present from all sources regardless of scale, provided it is larger than the image resolution. But it will also capture the gusts (or lulls) of the wind, and can give an erroneous image of the true magnitude of the forces. When the gusts and rotors are such that they might cause complications for wind production, the identification of them might be a valuable feature, but it will none the less affect the statistics.

5.3 Wind direction

Erroneous wind direction input into the CMOD algorithm can be a large factor in misestimation of wind speed. There are several examples of this in the ASAR wind scenes we have looked at. Most notable are probably the examples from 13 January 2011 in fig. 4.14, 13 January 2012 in fig. 4.18 and 27 February 2012 in fig. 4.20. In all of the examples, the wind vectors from the model meet at an angle in a limited area, which means that even if the wind in general from the model estimates should be correct, it's highly likely that the interpolation of the winds in this area have resulted in an error. In those instances where no other wind feature can be identified in the ASAR image, such as in these cases, it's quite likely that a erroneous wind direction is the cause. In the case of the 13 January 2012 scene, the problem is inherent in the model wind estimates, as this mistake in wind direction also leads directly to what is most likely an error in the wind speed.

It's hard to point directly to any feature of the wind climate and terrain when it comes to errors caused by wind direction, but it's worth taking note of the fact that two of the three discrepancies probably linked to errors in wind direction mentioned here are connected to southerly wind coming up the fjords, and all of them seem related to different wind directions converging. It seems clear that terrain features such as converging fjords would make such complicated wind situations more likely, and thus increase the chance of errors due to wrong wind direction when using model wind direction input.

Other studies have found that a higher accuracy in the wind direction is achieved when deriving it from SAR image features. Christiansen et al. (2006) found the accuracy to be 21° when using semi-automatic methods, and 33° for automatic retrieval. This is not very far from what was found in this study, where the accuracy of the model wind in relation to the in-situ observations was found to be 33.2°. This indicates that in general, model wind directions can be on par with automated wind direction retrieval. However, as in-situ observations were only available for a single on-shore site, there is no way here of examining the accuracy offshore, and for different locations near the coast. As the location of the Fakken wind farm is in an area which is topographically relatively well defined by the model, the results might not be representative for offshore locations.

5.4 Temporal and spatial displacement

For 25 February 2011, figures were included to examine the model wind estimates before and after the selected model time, as seen in fig. 4.16. These indicate that the large discrepancy between ASAR and model winds might be due to the model predicting that the high wind speed conditions will last longer than they actually do, and that they are temporally displaced in relation to the actual dynamics. If this is indeed the case, the wind prediction for 26 February is closer to what's observed by the ASAR, and the ASAR wind estimate might be much closer to the actual wind conditions. However, as long as model wind directions are used as input to the CMOD algorithm, there might be errors in the ASAR estimates as well as a result of this temporal misplacement, which makes an analysis of the ASAR estimates without grounds for comparison rather fruitless.

In the scene for 13 January 2012 in fig. 4.18, the different wind directions seemed to cause some issues regarding the input wind direction to the CMOD algorithm. If we study the ASAR image for the scene, we can see wind features in the image in the north-west corner and north of Fugløya which are not present in the model wind map. It's possible that the front which the model predicts will be crossing the southern half of Vannøya, is in reality further to the north and should coincide with this ASAR image feature. On this scale, the spatial displacement (if it indeed is that) is not very big for such a model. Figure 4.19 indicates that the wind conditions at the time was quite turbulent, and this might make it harder for the model to accurately predict the details in this scene.

5.5 Wind estimate comparisons

5.5.1 Polarization

We saw in section 4.1.1 that there is only a slight difference between the statistics for 'VV' and 'HH' polarization. With such a slim data basis for comparison, with only 11 scenes available with 'VV' polarization against 93 with 'HH' and nearly all of the 'VV' polarized scenes captured in June, there is not much that can be said about effect of different polarizations on ASAR wind speed estimates generally. The very small increase in RMSD for 'VV' polarization might just as well be a feature of the wind conditions in June.

5.5.2 Seasonal and diurnal effects

There's no clear trend when it comes to seasonal or diurnal affects. As mentioned in section 4.3.2, the ASAR image acquisition times make it hard to detect diurnal variations. Naturally this is a downside to using ASAR for wind estimation, as a piece of the puzzle will be lost, and one must be concious of this when trying to form an image of the wind climate at the site. There is a somewhat higher variance for the morning wind than the evening, and even higher yet for ASAR winds over model winds. The mean wind speeds are quite similar, and combined with the high variance, it's possible that the wind power density is a bit higher for morning winds than for evening. However, this is speculation and the data basis is too low to draw any conclusions.

When it comes to variations related to wind speed, there is also a large increase in variance for ASAR wind speeds with increasing speed. It's difficult to ascertain how meaningful this increase is, as the range of wind speeds in the group of high wind speeds is much larger than for low wind speeds, and an increase in variance is to be expected. No doubt this is a large weakness in this particular test. However, we should be able to expect some increase in variance for model wind estimates as well. In fact, the variance increases from low to medium wind speeds, from 6.7 to 10.3, but decreases to 9.9 for high wind speeds. We know that the range of wind speeds for model estimates is somewhat lower than for ASAR winds, with a maximum occurring wind speed of 22 m/s, while the ASAR wind estimates go as high as 25 m/s. Based on this, it's not entirely surprising the we get bias in favour of the ASAR wind estimates with such a low number of data points in this group.

5.5.3 Wind climate evaluation

The standard deviations and RMSD found in this study are generally higher than those found in similar studies. When comparing ASAR estimates with in-situ observations, Christiansen et al. (2006) found the standard deviation to be 1.3 m/s when using ASAR image streaks for wind direction inputs, and similar results were found in other studies (Monaldo et al., 2001; Hasager et al., 2008). Studies comparing ASAR and model wind estimates generally find larger deviations between the estimates than those comparing ASAR winds with in-situ observations. When Beaucage et al. (2007) compared the 4km MC2 NWP model with SAR wind estimates, they found a RMSE of 2.07 m/s and a correlation coefficient of 0.79, while Yang et al. (2011) found a standard deviation of 0.77 m/s between ASAR and the NOGAPS model estimates. There are several reasons why the deviations found in this study might be larger. One is the lack of rain filtering, as already mentioned. Another is the different method in filtering low wind speeds, as Beaucage et al. consistently removed all data points with wind speeds under 2 m/s, while in this study they are merely filtered on the basis of percentage in each scene. Though the frequency of such low wind speeds is very small in this study, it is none the less a possible source of error. Another factor is the proximity to land. As the furthest point from land is 23 km from the coast, with most of them being considerably closer, this study looks at an area much closer to land than similar studies.

A statistical analysis of the wind estimates gives a very limited idea of the wind climate and how the ASAR and model estimates differ. If we compare with the wind maps, and particularly the difference images of them, we see that instances with a low correlation coefficient can still visually appear quite well matched for large areas, yet be thrown off by smaller areas with large discrepancies. A good example of this is 13 January 2012 in section 4.4.4.

Examining the Weibull estimates is a good first step to get an impression of where the difficulties truly lie. Though it's impossible to say with any certainty which estimate should be trusted as a good representation of the true wind at the site, it is absolutely an indication that the terrain is affecting the estimates differently when the estimates differ considerably. If we look at the power density estimates, the differences

are quantified in a way that also illustrates the consequences of choosing the wrong basis for siting. Generally, the model predicts higher mean wind speeds with more variation than the ASAR estimates, in all cases but for location 5 and 6. The biggest difference is for 2 and 4, which we know are located between three islands which are not well defined in the model, and we've seen examples of this in several of the scenes. It's more difficult to say exactly what the results are. Generally, it seems that the model over-estimates the wind in these areas in comparison with the ASAR estimates, but it's quite possible that for some wind conditions there might be a speed-up effect around and down the mountains situated on these islands which is also lost.

If we examine the Weibull pdf estimates in fig. 4.7, we can see that the shape parameter for the model estimates vary relatively little, while those for the ASAR estimates vary somewhat more, and in particular tends towards positive skewness. In this they are more similar to the Fakken measurements. The most obvious difference between the in-situ wind observations from Fakken and the model wind estimates, is that the Fakken observations have a much larger spread in the data than the model wind. The difference in variance of 16.7 m/s is very large, and so is the RMSE of 4.22. If we examine the Weibull pdfs in fig. 4.9, we see that the in-situ observations encompass a far larger range of wind speeds than the model pdf. This tells us that the model is unable to capture the variation in wind at this location. It's possible that the same is true for model and ASAR estimates, and that the natural variability in the wind is lost in the model estimates. However, this doesn't allow us to conclude that the ASAR estimates are more accurate. As the model wind predictions are based on 10 minute averages, and the ASAR wind estimates reflect the nearly instantaneous wind, the ASAR estimates will capture the wind gusts, and so the wind might appear to be stronger than it really is. When investigating wind features in the ASAR wind map, there is the possibility that these features are accentuated by gust winds.

In general, the feature that primarily impacts the wind estimates seem to be slightly different placement and extent of the wind shadows, combined with the low level of terrain detail in the wind model. This impression is reinforced by the RMSD image in fig. 4.21. If we compare the RMSD illustration with the map in fig. 4.2, we can see that the area elected as a possible offshore wind park site is one of the places where the estimates diverge. It is near location 3, which has a high estimated wind power density, but also a very high difference between model and ASAR estimates. The ASAR images indicate that it has a high potential for both wind shadows from Vannøya, and turbulent wind conditions from the south-east. These can enhance power production by reducing wake effects, but depending on the nature of the source, can also increase load and reduce power output.

Chapter 6

Conclusion

Statistics for 2011 show that the RMSD is 3.33 m/s, which is higher than that found in similar studies. Possible reasons for this is that the data has not been filtered for rain, the scene is generally closer to land than the locations for other studies, and the topography of the region makes the wind climate very complex. The RMSE between the in-situ wind observations from Fakken and model data was found to be ~ 4.22 m/s, with a difference in variance of 16.7 m/s. This indicates that the model is unable to describe the variations in the wind for this area, but the statistics are not necessarily applicable offshore.

The data was examined for variations related to diurnal and seasonal effects, but no clear trends were found. The limited overpass times of the satellite makes diurnal biases hard to detect, however a slight trend in increased variance was found for morning winds with a possible increase in wind power density.

Model wind directions for the ASAR wind estimates were derived from the model wind predictions. The standard deviation between the Fakken in-situ wind directions and the model estimated wind directions was found to be 33.2°. With this estimate of the wind direction error, the corresponding wind speed error for the CMOD-IFR2 algorithm is 4.14 m/s for VV polarization and 3.98 m/s for HH polarization. Examination of wind features in the ASAR images indicate that converging wind directions may be a large source of error, possibly accentuated by the interpolation from 4 km resolution to 1 km resolution in the model. These complicated wind directional conditions most frequently occur around the fjord mouths. There are indications that wind features such as fronts in the model wind map are temporally and spatially misplaced. Aside from the impact this has on wind estimation with the model alone, it will also lead directly to estimation errors in the ASAR wind map by way of wind directional errors, as long as the model wind direction is used as input.

Wind shadowing occurs in both the model and ASAR wind estimates, but to very different extent. Wind shadowing is more closely linked with mountainous terrain in the ASAR wind maps, and is not present at all for some of the islands in the area, due to the low resolution of the model terrain. This means that a very important feature in terms of wind farm siting is missing from the model estimates, and may give an overly positive impression of the wind conditions. Other terrain and atmospheric features were not included in any large degree in the model wind map, such as local speed up effects and atmospheric gravity waves. Atmospheric gravity waves are indicators of atmospheric turbulence, and may be important factors to local wind climate conditions.

In general, the largest discrepancy between model and ASAR estimates seem to be associated with the fjord mouths, where we find complicated wind conditions, and the smaller islands, where the model terrain is not defined. The ASAR wind map is good tool for identifying relevant features in the local wind climate and their spatial extent, but it is sensitive to errors in wind direction input and errors in the NWP model. The

NWP model on the other hand suffers from low resolution, but is not as sensitive to short-term variations in the wind estimates. These are both issues that must be kept in mind when considering either as a tool for estimation of the wind climate for a first siting of an offshore wind farm.

6.1 Further research

This study has looked at possible complications when using ASAR and model wind maps for estimating the wind climate in a coastal area. The consequences connected to choosing a potential wind farm site base on wrong wind conditions can be costly, even if it is just a preliminary siting study. The results in this study are based on a limited data basis as well as a limited region, and though the region is very representative of typical Norwegian coastal terrain, it is necessary with a more extensive study to be able to generalize further about the coastal climate as estimated with these tools. With this in mind, certain adaptations are recommended:

- The use of data spanning several years to improve the statistical basis and get a better idea of seasonal variations.
- The comparison of different coastal regions to examine if similar results and features are found.
- The inclusion of offshore in-situ measurements. These could also enable the inclusion of data on the atmospheric stability of the site, which would give more insight into the wind climate and allow for extraction of wind speeds to turbine height.
- The use of a higher resolution model.

Appendix A

Appendix

$\alpha = c_1 + c_2P_1 + c_3P_2 + c_4P_3$

$\beta = c_5 + c_6P_1 + c_7P_2$

for which

$P_1 = x$ $\quad P_2 = \frac{(3x^2-1)}{2}$ $\quad P_3 = \frac{x(5x^2-3)}{2}$ $\quad x = \frac{(\theta-36)}{19}$

and

$b_1 = c_8 + c_9V_1 + c_10P_1 + c_{11}P_1V_1 + c_{12}P_2 + c_{13}P_2V_1$

$b_2 = c_{14} + c_{15}P_1 + c_{16}P_2 + (c_{17} + c_{18}P_1 + c_{19}P_2)V_1 + (c_{20} + c_{21}P_1 + c_{22}P_2)V_2 + (c_{23} + c_{24}P_1 + c_{25}P_2)V_3$

for which

$P_1 = x$ $\quad P_2 = 2x^2 - 1$ $\quad x = \frac{(2\theta-76)}{40}$

$V_1 = \frac{2V-28}{22}$ $\quad V_2 = 2V_1^2 - 1$ $\quad V_3 = (2V_2 - 1)V_1$

Table A.1: Variables of the CMOD-IFR2 function

	RMSD	Bias	Correlation ρ	Mean μ_{MODEL}	Mean μ_{ASAR}
SELECTED POINTS					
1	3.1791	-0.2838	0.5370	9.3872	9.1034
2	3.9197	-2.2864	0.4319	8.4119	6.1255
3	3.6963	-1.8578	0.5188	9.2801	7.4223
4	3.0932	-0.2031	0.4722	8.8242	8.6211
5	3.5041	-0.1071	0.3473	6.3880	6.2809
6	3.5592	-0.0481	0.4361	7.8387	7.7905
Whole data set	3.3293	-0.6426	0.5414	8.2841	7.6415
SELECTED DATES					
13 January 2011	4.4859	3.2372	0.1270	5.5261	8.7633
25 February 2011	6.1930	-5.2424	-0.0683	13.3605	8.1181
16 April 2011	5.4622	-4.7863	0.4228	14.3196	9.5333
26 December 2011	4.0350	2.9015	0.3980	15.9262	18.8277
13 January 2012	3.1395	-2.1770	0.0597	6.0667	3.8897
27 February 2012	3.6482	0.0343	0.3298	10.1161	10.1504
SEASONAL					
Spring	3.3789	0.2234	0.5635	8.2912	8.5147
Summer	3.3132	-1.2508	0.5552	8.5320	7.2811
Autumn	3.4256	-1.5143	0.5606	8.3072	6.7929
Winter	3.2470	-0.7282	0.5286	8.0438	7.3156
DIURNAL					
Morning (∼9:00)	3.4545	-0.3232	0.5586	8.1626	7.8393
Evening (∼19:00)	3.1912	-0.9812	0.5308	8.4130	7.4318
WIND SPEED					
Under 5 m/s	3.0251	-1.2910	0.3809	6.7503	5.4592
Between 5 m/s and 8 m/s	3.4002	-0.6690	0.4016	8.9492	8.2802
Over 8 m/s	3.6928	1.1238	0.5160	11.0115	12.1353

Table A.2: Statistics

	RMSE	Bias	Correlation ρ	Mean μ_{MODEL}	Mean $\mu_{IN-SITU}$	σ_{MODEL}	$\sigma_{IN-SITU}$
Fakken	4.2176	1.5684	0.6339	6.8025	8.3710	2.9661	5.0534

Table A.3: Statistics for Fakken

σ^2_{MODEL}	σ^2_{ASAR}	σ_{MODEL}	σ_{ASAR}	$\mu_{DIR,MODEL}$	$\sigma^2_{DIR,MODEL}$	$\sigma_{DIR,MODEL}$	n
12.0538	9.6604	3.4719	3.1081	198.5°	43.9°	70.9°	103
10.2757	7.5906	3.2056	2.7551	186.8°	41.2°	68.7°	103
10.0990	11.2968	3.1779	3.3611	193.2°	35.7°	64.0°	103
9.7250	8.4645	3.1185	2.9094	198.4°	39.9°	67.6°	103
7.7572	11.0668	2.7852	3.3267	203.2°	27.1°	55.8°	103
7.4193	14.3812	2.7238	3.7923	193.5°	21.3°	49.4°	103
11.0019	12.2324	3.3169	3.4975	193.4°	38.0°	66.0°	103
2.9177	7.9504	1.7081	2.8196	139.0°	5.9°	25.9°	11999
6.9112	3.3070	2.6289	1.8185	206.8°	1.2°	11.7°	11999
4.3059	7.3925	2.0751	2.7189	243.1°	0.2°	5.4°	11999
5.4604	7.4951	2.3367	2.7377	262.4°	0.7°	8.8°	11999
3.4578	1.9714	1.8595	1.4041	21.7°	29.2°	57.9°	11999
11.1656	8.6135	3.3415	2.9349	153.6°	3.1°	18.8°	11999
12.5981	13.4289	3.5494	3.6645	175.4°	24.1°	52.6°	34×11999
9.6840	11.3917	3.1119	3.3752	225.4°	33.7°	62.1°	28×11999
11.0862	10.3882	3.3296	3.2231	92.6°	41.5°	69.0°	12×11999
10.2320	10.9954	3.1987	3.3159	219.0°	42.1°	69.4°	30×11999
11.5793	14.9526	3.4028	3.8669	181.5°	40.6°	68.2°	53×11999
10.3575	9.2635	3.2183	3.0436	202.7°	34.5°	62.9°	50×11999
6.7336	5.3032	2.5949	2.3029	162.5°	41.3°	68.8°	40×11999
10.3281	8.1536	3.2137	2.8563	199.3°	34.0°	62.4°	50×11999
9.9848	15.0321	3.1599	3.8774	239.4°	29.1°	57.8°	12×11999

σ^2_{MODEL}	$\sigma^2_{IN-SITU}$	$\mu_{DIR,MODEL}$	$\mu_{DIR,IN-SITU}$	$\sigma_{DIR,MODEL}$	$\sigma_{DIR,IN-SITU}$	n
8.7976	25.5371	154.7°	187.5°	66.7°	71.2°	8273

Bibliography

Barthelmie, R. J. and Pryor, S. C. . Can satellite sampling of offshore wind speeds realistically represent wind speed distributions? *Journal of Applied Meteorology*, 42:83–94, January 2003.

Barthelmie, R. J. , Grisogono, B. , and Pryor, S. C. . Observations and simulations of diurnal cycles of near-surface wind speeds over land and sea. *Journal of geophysical research*, 101(D16):21327–21, 1996.

Barthelmie, R. J. , Pryor, S. C. , and Frandsen, S. T. . Climatology. In Twidell, J. and Gaudiosi, G. , editors, *Offshore Wind Power*, chapter 4, pages 43–70. Multi-Science Publishing Co. Ltd., 2009. ISBN 0906522633.

Beal, R. C. . Toward an international stormwatch using wide swath SAR. *Johns Hopkins APL Technical Digest*, 21(1):12–20, 2000.

Beaucage, P. , Glazer, A. , Choisnard, J. , Yu, W. , Bernier, M. , Benoit, R. , and Lafrance, G. . Wind assessment in a coastal environment using synthetic aperture radar satellite imagery and a numerical weather prediction model. *Canadian Journal of Remote Sensing*, 33(5):368–377, 2007.

Berens, P. . CircStat: a MATLAB toolbox for circular statistics. *Journal of Statistical Software*, 31(10): 1–21, 2009.

Brand, A. J. , Peinke, J. , and Mann, J. . Turbulence and wind turbines. In *Journal of Physics: Conference Series*, volume 318, page 072005. IOP Publishing, 2011.

Christiansen, M. B. . Wind energy applications of synthetic aperture radar. , Risoe National Lab., Roskilde (Denmark). Wind Energy Dept., 2006.

Christiansen, M. B. , Koch, W. , Horstmann, J. , and Nielsen, M. . Wind resource assessment from C-band SAR. *Remote Sensing of Environment*, 105:68–81, 2006.

Churchfield, M. J. , Lee, S. , Michalakes, J. , and Moriarty, P. J. . A numerical study of the effects of atmospheric and wake turbulence on wind turbine dynamics. *Journal of Turbulence*, (13), 2012.

Cohen, A. C. . Maximum likelihood estimation in the Weibull distribution based on complete and on censored samples. *Technometrics*, 7(4):579–588, 1965.

COMET Program, . MetEd website. `http://meted.ucar.edu/`, May 2013.

da Rosa, A. V. . *Fundamentals of Renewable Energy Processes*. Academic Press, 1 edition, 2005.

Dagestad, K. F. , Johannessen, J. , Hauge, G. , Kerbaol, V. , and Collard, F. . High-resolution wind field retrievals off the norwegian coast: Comparing ASAR observations and MM5 simulations. In *Proceedings OceanSAR 2006 Third Workshop on Coastal and Marine Applications of SAR*, 2006.

Davies, T. , Cullen, M. J. P. , Malcolm, A. J. , Mawson, M. H. , Staniforth, A. , White, A. A. , and Wood, N. . A new dynamical core for the Met Office's global and regional modelling of the atmosphere. *Quarterly Journal of the Royal Meteorological Society*, 131(608):1759–1782, 2005. ISSN 1477-870X.

Devore, J. L. and Berk, K. N. . *Modern mathematical statistics with applications*. Brooks/Cole, 2007.

Elachi, C. and van Zyl, J. J. . *Introduction To The Physics and Techniques of Remote Sensing*. Wiley-Interscience, 2006. ISBN 0471475696.

Espedal, H. , Johannessen, O. , Furevik, B. , Sandven, S. , Hasager, C. , Christensen, L. , and Gaudiosi, G. . WEMSAR - Wind energy mapping using synthetic aperture radar. In *Geoscience and Remote Sensing Symposium, 2001. IGARSS '01. IEEE 2001 International*, volume 3, pages 1137–1139, 2001.

European Environment Agency, . Europe's onshore and offshore wind energy potential - an assessment of environmental and economic constraints. 6, EEA, June 2009.

European Space Agency, . ESA official website. `http://www.esa.int`, November 2012.

Frank, H. P. , Rathmann, O. , Mortensen, N. G. , and Landberg, L. . The numerical wind atlas - The KAMM/WAsP method. 2001.

Furevik, B. R. , Espedal, H. A. , Hamre, T. , Hasager, C. B. , Johannessen, O. M. , Jørgensen, B. H. , and Rathmann, O. . Satellite-based wind maps as guidance for siting offshore wind farms. *Wind Engineering*, 27(5):327–338, 2003.

Gonzalez, R. and Woods, R. E. . *Digital image processing*. Prentice Hall, Upper Saddle River, N.J, 2008. ISBN 9780135052679.

Hasager, C. B. , Peña, A. , Christiansen, M. B. , Astrup, P. , Nielsen, M. , Monaldo, F. , Thompson, D. , and Nielsen, P. . Remote sensing observation used in offshore wind energy. *IEEE Journal on Selected Topics in Applied Earth Observations and Remote Sensing*, 1(1):–, 2008.

Hasager, C. B. , Nielsen, M. , Astrup, P. , Barthelmie, R. , Dellwik, E. , Jensen, N. O. , Jørgensen, B. H. , Pryor, S. C. , Rathmann, O. , and Furevik, B. R. . Offshore wind resource estimation from satellite SAR wind field maps. *Wind Energy*, 8(4):403–419, 2005.

Hasager, C. B. , Astrup, P. , Nielsen, N. M. , Christiansen, M. B. , Badger, J. , Nielsen, P. , Sørensen, P. , Barthelmie, R. J. , Pryor, S. , and Bergström, H. . SAT-WIND project. Final report. , April 2007.

Hasager, C. B. , Badger, M. B. , Peña, A. , Badger, J. , Antoniou, I. , Nielsen, M. , Astrup, P. , Courtney, M. , and Mikkelsen, T. . Advances in offshore wind resource estimation. In Sathyajith, M. and Philip, G. S. S. , editors, *Advances in Wind Energy Conversion Technology*, volume 0, pages 85–106. Springer Berlin Heidelberg, 2011.

Hertenstein, R. F. and Kuettner, J. P. . Rotor types associated with steep lee topography: Influence of the wind profile. *Tellus A*, 57(2):117–135, 2005.

Hofstad, K. and Tallhaug, L. . Wind power potential outside the norwegian coast (offshore); (vindkraftpotensialet utenfor norskekysten (offshore)). , Norwegian Water Resources and Energy Directorate (NVE), Oslo, Norway, February 2008.

Hyndman, R. J. and Koehler, A. B. . Another look at measures of forecast accuracy. *International Journal of Forecasting*, 22(4):679–688, 2006.

Jammalamadaka, S. R. and Sengupta, A. . *Topics in circular statistics*, volume 5. World Scientific Publishing Company, 2001.

Johannessen, O. , Espedal, H. , Furevik, B. , Hamre, B. T. , Sandven, S. , Hasager, C. , Christensen, L. , Gaudiosi, G. , Pirazzi, L. , and Jevne, G. . WEMSAR. Wind Energy Mapping using Synthetic Aperture Radar. Key action 5: Cleaner energy systems, including renewable energies. WEMSAR final report. , Nansen Environmental and Remote Sensing Center, March 2003.

Kalnay, E. . *Atmospheric modeling, data assimilation and predictability*. Cambridge university press, 2003.

Koch, W. . Directional analysis of SAR images aiming at wind direction. *IEEE Transactions on Geoscience and Remote Sensing*, 42(4):702–710, 2004.

Kudryavtsev, V. , Hauser, D. , Caudal, G. , and Chapron, B. . A semiempirical model of the normalized radar cross-section of the sea surface 1. background model. *J. Geophys. Res.*, 108(C3):8054–, January 2003. ISSN 0148-0227.

Lin, H. , Xu, Q. , and Zheng, Q. . An overview on SAR measurements of sea surface wind. *Progress in Natural Science*, 18(8):913–919, 2008. ISSN 1002-0071.

Liu, W. T. and Xie, X. . Measuring ocean surface wind from space. *Remote Sensing of the Marine Environment: Manual of Remote Sensing*, 6:149–178, 2006.

Lynn, P. A. . *Onshore and offshore wind energy: An introduction*. Wiley Publishing, Inc., 2012. ISBN 047097608X.

Manwell, J. F. , McGowan, J. G. , and Rogers, A. L. . *Wind Energy Explained: Theory, Design and Application*. Wiley, 2010. ISBN 0470015004.

Mathew, S. . *Wind energy fundamentals, resource analysis and economics*. Springer, Berlin New York, 2006. ISBN 9783540309062.

Met Office, . Met office unified model. `http://www.metoffice.gov.uk/research/modelling-systems/numerical-models`, May 7th 2013.

Monaldo, F. M. , Thompson, D. R. , Beal, R. C. , Pichel, W. G. , and Clemente-Colon, P. . Comparison of SAR-derived wind speed with model predictions and ocean buoy measurements. *IEEE Transactions on Geoscience and Remote Sensing*, 39(12), 2001.

Monaldo, F. . The Alaska SAR Demonstration and Near Real-Time Synthetic Aperture Radar Winds. *John Hopkins APL Technical Digest*, 21, 2000.

Mouche, A. , Hauser, D. , Kudryavtsev, V. , and Daloze, J. . Multi-polarisation ocean radar cross-section from envisat asar observations, airborne polarimetric radar measurements and empirical or semi-empirical models. *Proc. of the 2004 Envisat & ERSsymposium, CD-rom*, 373, 2004.

Nielsen, M. , Astrup, P. , Hasager, C. B. , Barthelmie, R. , and Pryor, S. . Satellite information for wind energy applications. , 2004.

Norwegian Coastal Administration, . Kystinfo map service. http://www.kart.kystverket.no/, June 2013.

Pavia, E. G. and O'Brien, J. J. . Weibull statistics of wind speed over the ocean. *Journal of climate and applied meteorology*, 25(10):1324–1332, 1986.

Pichel, W. G. and Clemente-Colón, P. . NOAA CoastWatch SAR applications and demonstration. *John Hopkins APL technical digest*, 21(1):49–57, 2000.

Pryor, S. C. , Nielsen, M. , Barthelmie, R. J. , and Mann, J. . Can satellite sampling of offshore wind speeds realistically represent wind speed distributions? Part II: quantifying uncertainties associated with distribution fitting methods. *Journal of Applied Meteorology*, 43:739–750, May 2004.

Quilfen, Y. and Bentamy, A. . Calibration/validation of ERS-1 scatterometer precision products. In *Geoscience and Remote Sensing Symposium, 1994. IGARSS'94. Surface and Atmospheric Remote Sensing: Technologies, Data Analysis and Interpretation., International*, volume 2, pages 945–947. IEEE, 1994.

Quilfen, Y. , Chapron, B. , Elfouhaily, T. , Katsaros, K. , and Tournadre, J. . Observation of tropical cyclones by high-resolution scatterometry. *Journal of Geophysical Research: Oceans (1978–2012)*, 103 (C4):7767–7786, 1998.

Richards, J. . Scattering from earth surface features. In *Remote Sensing with Imaging Radar*, Signals and Communication Technology, pages 135–180. Springer Berlin Heidelberg, 2009. ISBN 978-3-642-02019-3.

Romeiser, R. and Alpers, W. . An improved composite surface model for the radar backscattering cross section of the ocean surface 2. model response to surface roughness variations and the radar imaging of underwater bottom topography. *J. Geophys. Res.*, 102(C11):25251–25267, 1997. ISSN 0148-0227.

Romeiser, R. , Alpers, W. , and Wismann, V. . An improved composite surface model for the radar backscattering cross section of the ocean surface 1. theory of the model and optimization/validation by scatterometer data. *J. Geophys. Res.*, 102(C11):25237–25250, 1997. ISSN 0148-0227.

Schneiderhan, T. , Lehner, S. , Schulz-Stellenfleth, J. , and Horstmann, J. . Comparison of offshore wind park sites using SAR wind measurement techniques. *Meteorological Applications*, 12(2):101–110, 2005.

Sempreviva, A. , Barthelmie, R. , and Pryor, S. . Review of methodologies for offshore wind resource assessment in european seas. *Surveys in Geophysics*, 29:471–497, 2008.

Skolnik, M. . *Introduction to radar systems*. McGraw Hill, Boston, 2001. ISBN 007118189X.

Snyder, J. P. . *Map projections–A working manual*. Number 1395. USGPO, 1987.

Steiness, C. . (Photographer). Wake effects at Horns Rev windfarm, Denmark. Shared under Creative Commons Lisence. , Vattenfall, Stockholm, Sweden, May 3rd 2013. URL http://www.flickr.com/photos/vattenfall/4270899001/.

Swinbank, R. . Numerical weather prediction. In Lahoz, W. , Khattatov, B. , and Menard, R. , editors, *Data Assimilation: Making Sense of Observations*, pages 381–406. Springer Berlin Heidelberg, 2010. ISBN 978-3-540-74702-4.

The European Wind Energy Association, . Wind in our sails – the coming of europe's offshore wind energy industry. , EWEA, 2011.

Thompson, D. R. , Elfouhaily, T. M. , and Chapron, B. . Polarization ratio for microwave backscattering from the ocean surface at low to moderate incidence angles. In *Geoscience and Remote Sensing Symposium Proceedings, 1998. IGARSS'98. 1998 IEEE International*, volume 3, pages 1671–1673. IEEE, 1998.

Tonboe, R. T. . *Detailed Wind Speed Information From RADARSAT ScanSAR Wide*. Danish Meteorological Institute, Ministry of Transport, 2001.

Troms Kraft, . Fakken vindpark. `http://www.tromskraft.no/om/prosjekter/fakken`, May 11th 2013.

Twidell, J. . Basics of wind turbines. In Twidell, J. and Gaudiosi, G. , editors, *Offshore Wind Power*, chapter 2, pages 15–26. Multi-Science Publishing Co. Ltd., 2009. ISBN 0906522633.

Vestas, . Vestas product website for the V112-3.3 MW IEC 1B turbine. `http://www.vestas.com/en/wind-power-plants/procurement/turbine-overview/3-mw-platform/v112-3.3-mw-iec-1b.aspx#/vestas-univers`, May 1st 2013.

Walpole, R. E. , Myers, R. H. , Myers, S. L. , and Ye, K. . *Probability and statistics for engineers and scientists*, volume 8. Prentice Hall Upper Saddle River, NJ:, 2007.

Worthington, R. . Alignment of mountain lee waves viewed using noaa avhrr imagery, mst radar, and sar. *International Journal of Remote Sensing*, 22(7):1361–1374, 2001.

Worthington, R. . Mountain waves launched by convective activity within the boundary layer above mountains. *Boundary-layer meteorology*, 103(3):469–491, 2002.

Yang, X. , Li, X. , Pichel, W. , and Li, Z. . Comparison of ocean surface winds from envisat asar, metop ascat scatterometer, buoy measurements, and nogaps model. *Geoscience and Remote Sensing, IEEE Transactions on*, 49(12):4743–4750, 2011.

Young, G. S. , Sikora, T. D. , and Winstead, N. S. . Manual and semiautomated wind direction editing for use in the generation of synthetic aperture radar wind speed imagery. *Journal of Applied Meteorology and Climatology*, 46(6):776–780,785–787,789–790–776, 2007.

Zar, J. H. and others, . *Biostatistical analysis*. Pearson Education India, 1999.

List of Abbreviations

ASAR Advanced Satellite Aperture Radar

CMOD C-band Model Function

ESA European Space Agency

FIMEX File Interpolation, Manipulation and EXtraction

GMF Geophysical Model Function

HIRLAM High Resolution Local Area Model

KAMM Karlsruhe Atmospheric Mesoscale

MET Meteorological Institute

MSE Mean Square Error

NOGAPS Naval Operational Global Atmospheric Prediction System

NORUT Northern Research Institute

NRCS Normalized Radar Cross Section

NVE Norwegian Water Resources and Energy Directorate

NWP Numerical Weather Prediction

OI Optimal Interpolation

RCS Radar Cross Section

RMSD Root Mean Square Difference

S-WASP Satellite - Wind Atlas Analysis and Application Program

SAR Synthetic Aperture Radar

UM Unified Model

UTM Universal Transverse Mercator

WaSP Wind Atlas Analysis and Application Program

WEMSAR Wind Energy Mapping using Synthetic Aperture Radar

WMO World Meteorological Organisation

List of Figures

List of Tables


UNIVERSITY
OF TROMSØ